UNIVERSITÀ DEGLI STUDI DI PADOVA

Dipartimento di Scienze Chimiche

Corso di laurea magistrale in chimica

Tesi di laurea

Terthiophene as a Novel Spin Laber for the EPR investigation of Peptide-Protein interactions

Relatore
Prof. Marco Bortolus

Laureando: Luca Boscolo Chiodoro
Matricola: 2158493

Anno Accademico 2025/26

Summary

Abstract

Electron paramagnetic resonance (EPR) spectroscopy is widely employed in structural biology for the determination of intra- and intermolecular distances in biomolecular complexes. Such measurements rely on the introduction of paramagnetic spin labels through site-directed spin labeling (SDSL), often combined with site-directed mutagenesis (SDM) to selectively control the labeling position within the protein sequence. Among pulsed EPR techniques, double electron–electron resonance (DEER) allows for distance measurements between pairs of stable radicals, whereas Laser-Induced Magnetic Dipole spectroscopy (Laser-IMD) enables distance measurements between a stable radical and a photo excitable triplet-state label.

This thesis reports the study of terthiophene (TT) as a novel photo excitable spin label for pulsed EPR spectroscopy. The acetyl-imidazole-functionalized TT was selected because it can be linked to cysteine residues through a one-atom covalent linker, which was expected to limit conformational flexibility and produce narrow distance distributions. Upon excitation with 355 nm laser pulses, TT populates the triplet state. At the same wavelength, it also forms the radical anion, raising the question whether TT is more suitable for Laser-IMD or DEER measurements.

This study was carried out on the CaM-M13C system, which mimics the interaction between calmodulin and the myosin light chain kinase (MLCK) that occurs during smooth muscle contraction. Previously prepared single-cysteine CaM mutants (positions 6, 100 and 114) and M13C peptide were employed as model systems for TT labeling and EPR characterization. CaM mutants were already available with the SPIRO nitroxide spin-label. TT labeling tests were conducted both on M13C and unlabeled CaM mutants.

The labeled peptide (M13TT) was purified by reverse phase chromatography (RPC). UV-Vis spectroscopy was used both to characterize the RPC fractions and to determine the labeling efficiency. Echo detected EPR was employed to characterize the triplet-state spectra of free TT, M13TT, CaM6S-M13TT, CaM100S-M13TT and CaM114S-M13TT. DEER and Laser-IMD measurements were performed on the peptide-protein complexes to determine inter-spin distance distribution between the SPIRO nitroxide on CaM and the TT on the peptide.

The acetyl-imidazole-functionalized TT derivative exhibited limited aqueous solubility, slow labeling kinetics, and marked pH sensitivity, requiring mixed DMSO/water conditions for efficient conjugation. While these conditions enabled peptide labeling, they proved incompatible with protein substrates, representing a significant limitation for broader biomolecular applications of TT-based spin labels. Photoinduced radical anion formation significantly complicated Laser-IMD measurements, limiting the overall suitability of TT for this technique. The radical generation may originate from charge-transfer processes involving a neighboring tryptophan residue within the peptide sequence. Furthermore, the measured distance distributions were broader than initially expected, suggesting that the conformational flexibility of TT may still be significant. These findings indicate that shorter thiophene-based labels, such as dithiophene derivatives, may represent more suitable candidates for future pulsed EPR distance measurements.

Introduction

1 Calmodulin

Calmodulin (CaM) and M13, a peptide derived from one of its protein targets (myosin light chain kinase - MLCK), are the systems used in this thesis. The well-defined geometry of the CaM/M13 complex, and the possibility of obtaining CaM mutants with cysteines for spin labeling, make this an ideal model system for distance measurements using pulsed EPR techniques.

CaM is a messenger protein that acts as an intracellular receptor for Ca^{2+}, which is a secondary messenger. CaM transduces changes of intracellular Ca^{2+} concentration into conformational changes of target proteins, modulating their biological activity. CaM has four EF-hand sites, helix-loop-helix structural motifs specialized in coordinating Ca^{2+} ions; Ca^{2+} binding induces important conformational changes in CaM (holo-CaM conformation – see below) that favor its interaction with target proteins by exposition of hydrophobic residues involved in the complex. Among CaM targets, we are interested in MLCK, involved in the smooth muscle contraction process, schematized in **Figure 1**. Muscle contraction originates from the sliding of myosin filaments on actin filaments. In smooth muscle tissues, the actin–myosin interaction is regulated by phosphorylation of the myosin light chain. Phosphorylation is performed by MLCK, which in turn is activated by holo-CaM. For muscle cell contraction to occur, Ca^{2+} must enter the cytoplasm from the sarcoplasmic reticulum or the extracellular space. Calcium binds to calmodulin, MLCK activation occurs, and increased phosphorylation of the myosin light chain takes place.

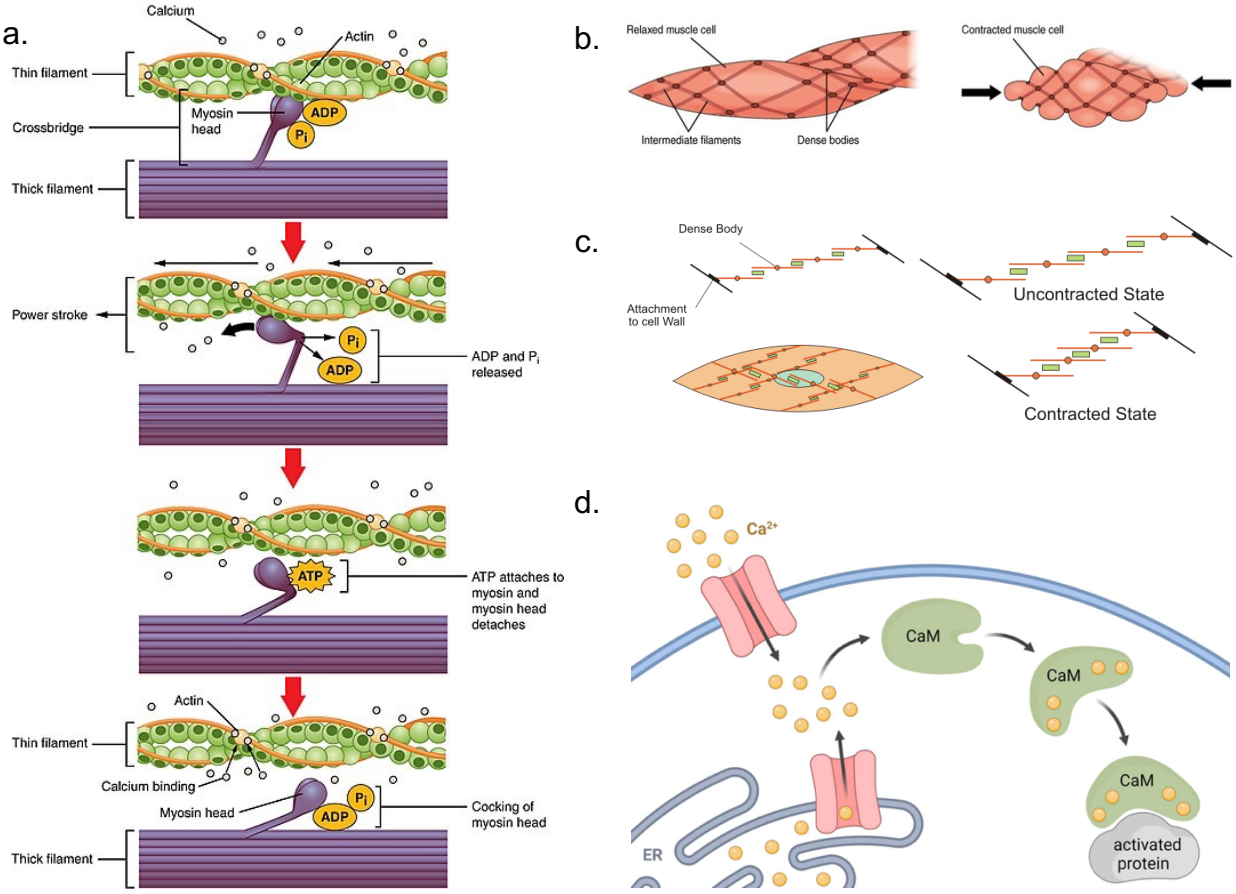

Figure 1: Smooth muscle contraction mechanism regulated by the CaM/Ca^{2+} complex. (a) Actin-myosin cycle associated with phosphorylation of the myosin light chain. (b, c) Organization of contractile filaments in smooth muscle and their reciprocal sliding.[1] (d) MLCK activation mediated by the Ca^{2+}/CaM complex.[2]

These conditions allow the interaction between actin and myosin, thus beginning muscle contraction. Reduction of calcium concentration in the cytoplasm deactivates MLCK but does not stop muscle contraction. To stop it, dephosphorylation of myosin through a dedicated phosphatase will be necessary.

Since observing the interaction between two proteins can be difficult, we used only the MLCK sequence interacting with CaM, the high affinity peptide called M13. The M13 peptide constitutes one of the most widely used model systems for the study of the CaM-target interaction, since it retains the essential binding domain of the MLCK while significantly reducing the experimental complexity compared to the complete protein.[3] It is a peptide of 22 amino acids corresponding to those between 577 and 602 of the MLCK. A cysteine (Cys) was added to the N terminal residue of the sequence to allow the spin probe to be attached via the sulfide group.

MLCK (M13wt)	KRRWKKNFIAVSAANRFKKISS
M13Cys	CKRRWKKNFIAVSAANRFKKISS

The crystallographic structure of the holo-CaM[4] shows a long central α-helix that connects the N- and C-terminal domains.[5] However, multidimensional NMR studies have shown that, in solution, this central region has high conformational flexibility and can adopt partially unfolded conformations, allowing the protein to wrap around and adapt to different target sequences.[6] This conformational flexibility allows the holo-CaM to envelop the target peptide, stabilizing the complex through predominantly hydrophobic interactions. In **Figure 2** the conformational changes are shown, with panel (C) showing the CaM/M13 complex.

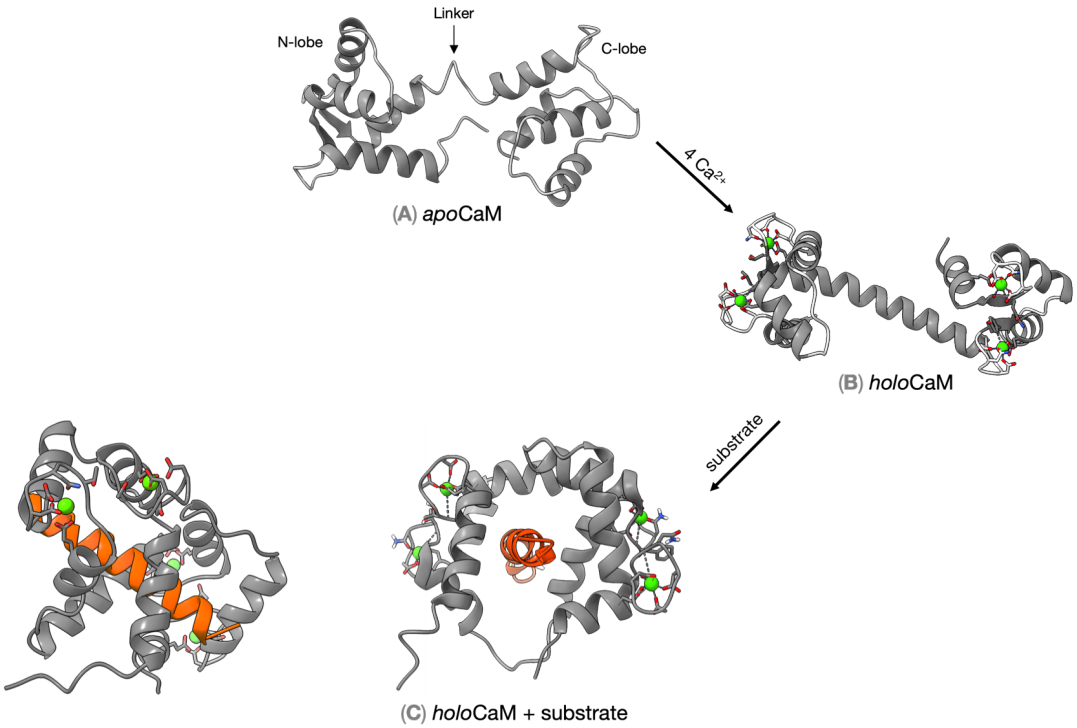

Figure 2: Crystallographic structures of CaM in different conformational states: (A) apo-CaM; (B) holo-CaM bound to four Ca^{2+} ions; (C) holo-CaM/M13 complex.

2 EPR

Electron Paramagnetic Resonance (EPR), alternatively named Electron Spin Resonance (ESR) is an increasingly popular and versatile technique in structural biology. EPR spectroscopy is a physicochemical technique used to investigate paramagnetic systems - species with at least one unpaired electron, or in general with a non-null electron spin angular momentum S≠0.

2.1 EPR fundamentals

2.1.1 The spin system

The electron is a fundamental particle of negative charge. Electrons are characterized by an intrinsic angular momentum, called spin (**S**). For an electron there are two spin states, called up and down. To describe them, the spin quantum number $\left(S = \frac{1}{2}\right)$ and the spin magnetic quantum number $\left(m_s = \pm\frac{1}{2}\right)$ are used. They provide information respectively on the modulus of the angular momentum vector and its projection on the z-axis of the reference frame, as it's visually represented in **Figure 3**.

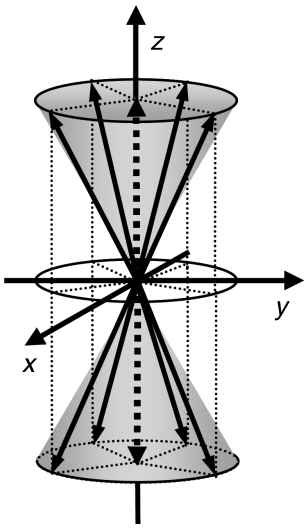

Figure 3: Vectorial representation of the electron spin moment. The electron spin angular momentum is a vector represented in the figure as a solid arrow, while the z component is shown in the figure as a dotted arrow pointing in the positive (α-spins) or negative z direction (β-spins). According to quantum mechanics, when a Cartesian frame x, y, z is chosen, only a component of the spin vector (usually assumed as the z component) has a definite value.

Now we come to the crucial feature for EPR spectroscopy. For each electron, the angular spin momentum is associated with a magnetic moment through:

$$\widehat{\boldsymbol{\mu}}_{\boldsymbol{e}} = g_e \mu_B \widehat{\boldsymbol{S}} \tag{1}$$

Where $g_e = 2.0023$ is the Landé factor, while $\mu_B = -2.974 \cdot 10^{-24} JT^{-1}$ is the Bohr magneton.

2.1.2 The Zeeman effect

In orbitals containing two coupled electrons the respective magnetic moments cancel each other out $(S = 0)$, while in orbitals with one unpaired electron the magnetic moment remains

and can be influenced by an external magnetic field B_0. If we consider an isolated electron, in a vacuum and in the absence of fields, it can exist in both m_s states with the same probability; they are degenerate. However, as represented in **Figure 4**, in the presence of the B_0 the two states lose degeneration and acquire different energies: this phenomenon is called the Zeeman effect and is one of the basic principles of magnetic resonance techniques, such as EPR. At thermal equilibrium their populations will then be described by the Boltzmann distribution.

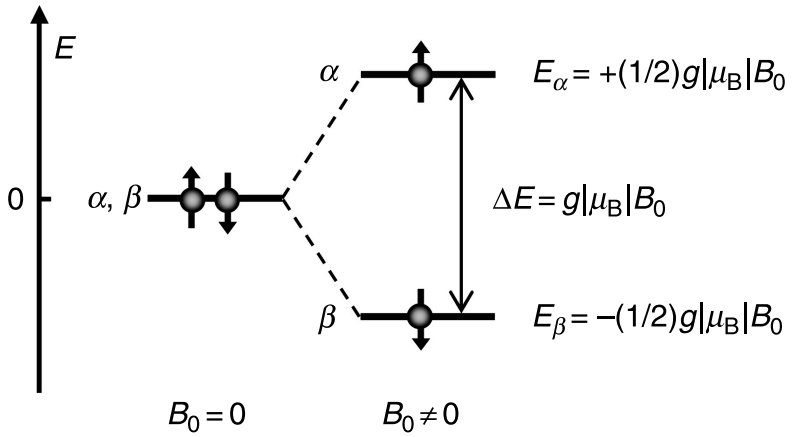

Figure 4: Representation of the Zeeman effect. To the left, in absence of B_0, the two energy levels are degenerate. To the right, the presence of B_0 causes the energy levels splitting.

In both states, the magnetization is oriented parallel to the direction of B_0, which by convention is placed as the z-axis. What physically distinguishes the two states is the direction of the magnetic moment projection on the z-axis. In the case of the β state, the magnetic moment and B_0 are parallel and point toward opposite directions, while for the α state the direction is the same. The energy of each level is described through the Hamiltonian of the Zeeman effect.

$$\widehat{\mathcal{H}}_{zeeman} = -\widehat{\boldsymbol{\mu}}_{\boldsymbol{e}}\boldsymbol{B_0} = -g\mu_B\widehat{\boldsymbol{S}}\boldsymbol{B_0} \tag{2}$$

$$E_{\pm} = -\boldsymbol{\mu_e B_0} = -g\mu_B \boldsymbol{S B_0} = -g\mu_B m_s^{\pm} B_0 \tag{3}$$

$$E_\alpha = E_+ = +\frac{1}{2}g|\mu_B|B_0 \tag{4}$$

$$E_\beta = E_- = -\frac{1}{2}g|\mu_B|B_0 \tag{5}$$

Where α refers to the state with $m_s = +\frac{1}{2}$, while β refers to the state with $m_s = -\frac{1}{2}$. When degeneration between two states is lost in a system, it becomes possible to stimulate energy transitions between them through electromagnetic radiation (EMR). In the case of an electron subjected to the Zeeman effect, it will undergo magnetic transitions because the transition is stimulated by the magnetic component of the EMR. The magnetic component of the EMR used to make the transition happen is referred to as B_1. The second basic principle of the EPR technique is that the energy of the EMR must be the same as the difference in energy between the two energy levels.

$$h\nu = \Delta E = E_\alpha - E_\beta = g|\mu_B|B_0 \tag{6}$$

Since a photon is absorbed during the transition, if the instrument detects a drop in the power of the EMR leaving the sample, then it means that an electron transition is taking place. As sowed in **Figure 5**, because of experimental setup the spectra will appear in derivative mode and centered at the g_e value.

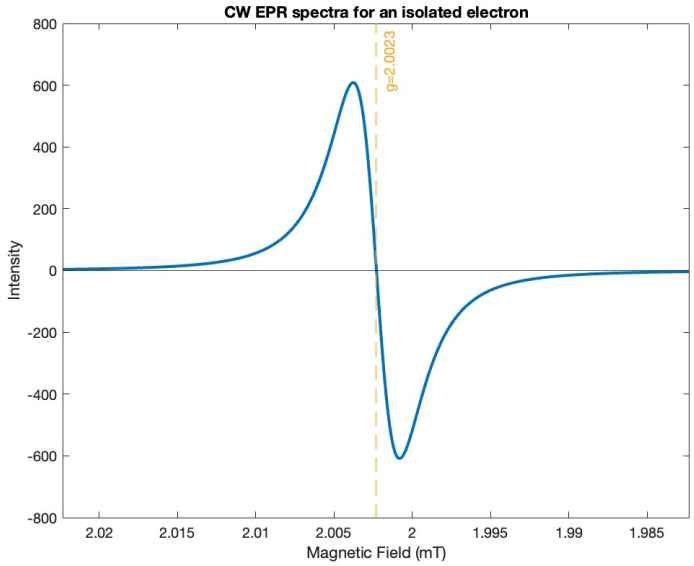

Figure 5: CW EPR spectra for an isolated electron.

2.1.3 g anisotropy

Until now we have considered a spin system consisting of an isolated electron. However, when the unpaired electron is contained within the orbital of a molecule, the contribution of the orbital angular momentum to the electron's magnetic moment must also be considered.

Indeed, if the contribution of angular momentum and spin moment to the magnetic moment of the electron were independent, then there would be no difference between the spectrum of the isolated electron and that for an electron contained in an orbital.

$$\boldsymbol{\mu_e} = \mu_B \boldsymbol{l} - g\mu_B \boldsymbol{S} \tag{7}$$

In organic radicals, orbital angular momentum is generally quenched by the molecular field. However, the spin-orbit coupling causes mixing between the angular and spin momentum, with partial restoration of the angular momentum and deviation of the g-value from that of the isolated electron.

$$\hat{\mathcal{H}}_{zeeman} = g\mu_B \hat{\boldsymbol{S}} \boldsymbol{B_0} + \boldsymbol{\lambda} \hat{\boldsymbol{l}} \hat{\boldsymbol{S}} \tag{8}$$

Spin-orbit coupling is an anisotropic interaction, so the value of g will depend on the orientation of the external field with respect to the molecule. To simplify the mathematical treatment, it is possible to enclose the angular and spin contribution in a single term through the introduction of the $\boldsymbol{g}$ tensor, a rank-2 tensor.

$$\hat{\mathcal{H}}_{zeeman} = g\mu_B \hat{\boldsymbol{S}} \boldsymbol{g} \boldsymbol{B_0} \tag{9}$$

The reference system in which the $\boldsymbol{g}$ tensor gets diagonalized is called the principal axes system and the g values for each axis will appear on the diagonal of the tensor.

$$\boldsymbol{g} = \begin{bmatrix} g_{xx} & g_{xy} & g_{xz} \\ g_{yx} & g_{yy} & g_{yz} \\ g_{zx} & g_{zy} & g_{zz} \end{bmatrix} \tag{10}$$

$$\boldsymbol{g} = \begin{bmatrix} g_{xx} & 0 & 0 \\ 0 & g_{yy} & 0 \\ 0 & 0 & g_{zz} \end{bmatrix} \tag{11}$$

If the sample is a solution and the probe can rotate freely, then g anisotropy will have no effect on the spectral shape and a single line centered at the isotropic value g_{iso} will be observable (still different from that for the free electron).

$$g_{iso} = \frac{(g_{xx} + g_{yy} + g_{zz})}{3} \tag{12}$$

In the case of a powdered sample (solid or frozen solution), since free rotation of the sample is no longer possible, the EPR spectrum will take on a more structured shape.

The simplest case is that of a powder spectrum on an axial symmetry, in which two diagonal values from the $\boldsymbol{g}$ tensor are identical to each other while the third one is different. As in **Figure 6**, in the integrated form of the spectrum, the most intense peak will represent the radical population whose z-axis is oriented orthogonally to the external field, which happens to be the most populated. On the other hand, the less intense peak will represent the radical population oriented parallel to the external field.

Next comes the more complicated case of a fully anisotropic powder spectrum. As in **Figure 7**, in a system with a rhombic tensor all principal values of the $\boldsymbol{g}$ tensor are different from each other. The integrated shape of the spectrum will consist of three peaks, each representative of one of the three diagonal components of the $\boldsymbol{g}$-tensor.

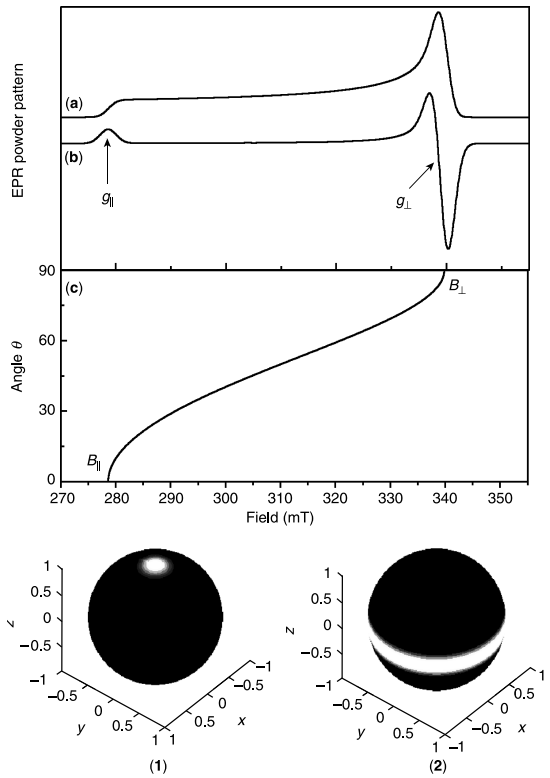

Figure 6: The (a) absorption and (b) first derivative EPR line shape for a randomly oriented $S = \frac{1}{2}$ spin system with axial symmetry ($g_\parallel = 2.437$, $g_\perp = 2.000$, $\nu = 9.5\ GHz$). (c) The angular dependency curve (θ vs. field) is shown. The orientation selection on the unit spheres are also provided for the observer position in the $g_\parallel$ plane (1) and the $g_\perp$ plane (2).

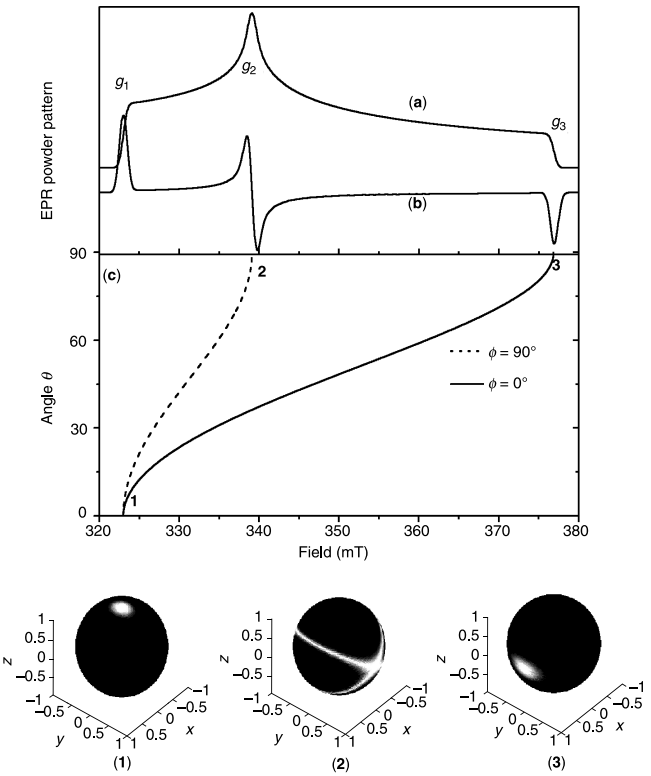

Figure 7: The (a) absorption and (b) first derivative EPR line shape for a randomly oriented $S = \frac{1}{2}$ spin system with rhombic symmetry ($g_1 = 2.101$, $g_2 = 2.000$, $g_3 = 1.800$, $\nu = 9.5\ GHz$). (c) The angular dependency curve (θ vs. field) is shown for two angles of f¼ 08 and 908. The orientation selections on the unit spheres are also shown for the observer position in the $g_\parallel$ plane (1), $g_\perp$ plane (2), and g_3 plane (3).

2.1.4 Energy levels

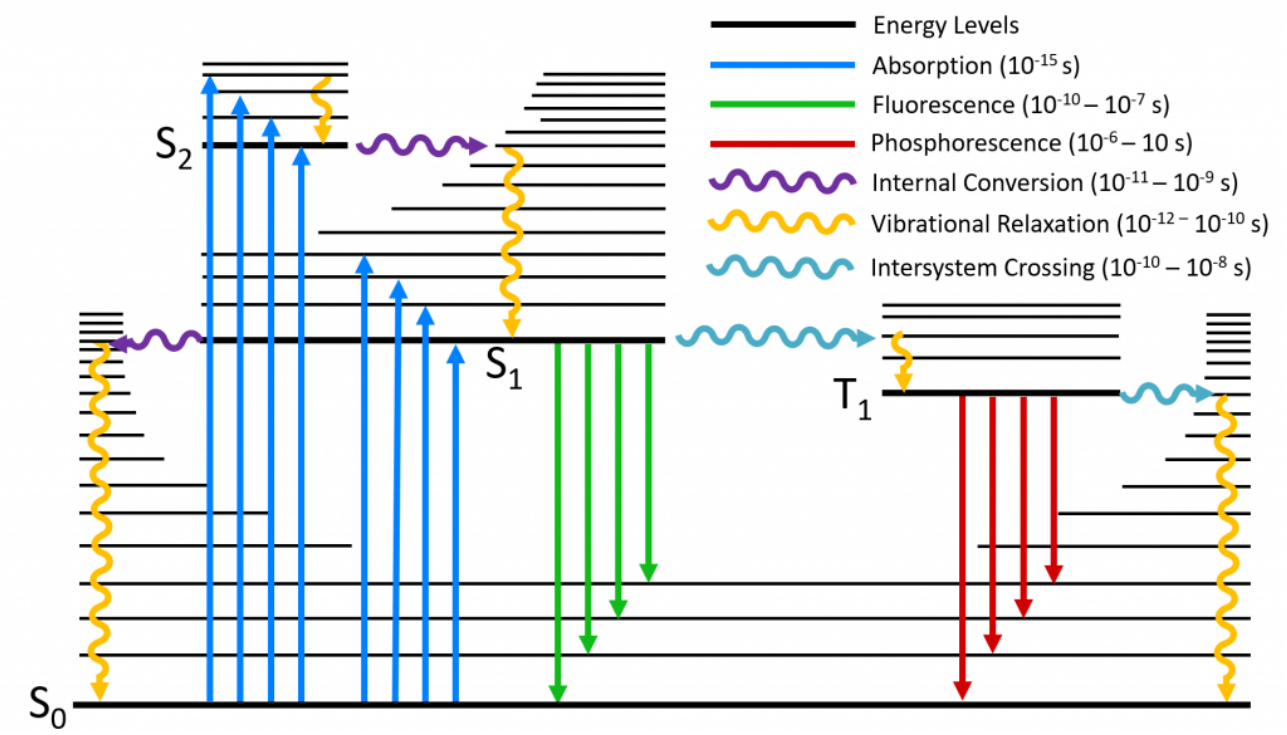

Figure 8: A typical Jablonski diagram showing the possible radiative and non-radiative transitions.[7]

The Jablonski diagram (**Figure 8**) allows the representation of molecular electronic levels (bold horizontal lines) with their vibrational sublevels (thin horizontal lines above bold ones) and how they are connected by electronic transitions. Each of these states describes the valence electrons for the molecule. In most molecules the ground and excited states are singlets, S_n where all electrons are paired $(S = 0)$ and the molecule is invisible to the EPR. In a radical, not represented here, the ground state is a doublet $(S = \frac{1}{2})$. In the triplet state T_n there are two unpaired electrons, so $(S = 1)$ and the molecule will be EPR visible. To switch the system into the triplet state a molecule must be excited, usually by EMR. Light absorption excites the system from the ground state S_0 to a generic S_n singlet state. Subsequently, the system will be able to populate the triplet state through intersystem crossing (ISC), formally a forbidden non-radiative transition.

2.1.5 Triplet state and Zero Field Splitting

The triplet state is formally made up of three degenerate energy levels $(S = 1)$. In it, two unpaired electrons with identical spin quantum number can coexist. When at least two unpaired electrons are present in a system, the phenomenon of Zero Field Splitting (ZFS) occurs, which leads to loss of degeneracy of the energy levels of the triplet even with $B_0 = 0$, as represented in **Figure 9**. The two unpaired electrons of the triplet state can be considered as two distinct and interacting magnetic moments.

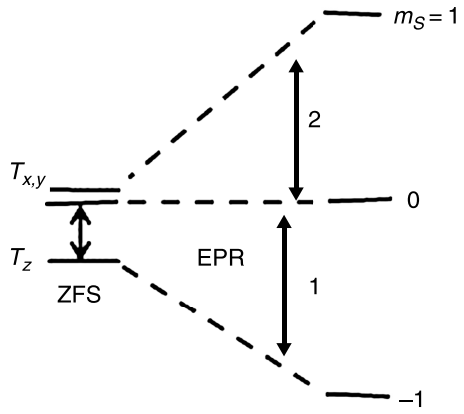

Figure 9: A schematic energy level diagram for a triplet ($S = 1$). The ZFS in the absence of a magnetic field and the subsequent additional Zeeman splitting for an applied external field is illustrated.

The dipole-dipole interaction between the magnetic moment of one electron and the magnetic field generated by the magnetic moment of the other electron is the main contribution. Since it depends on the relative orientation of the dipole moments, it's an anisotropic interaction and can be represented by a rank-2 tensor. The energy of the dipolar interaction is:

$$E_{dip} = \left(\frac{\mu_0}{4\pi}\right) g^2 \mu_B^2 \left[\frac{\boldsymbol{S_1} \cdot \boldsymbol{S_2}}{r^3} - 3\frac{(\boldsymbol{S_1} \cdot \boldsymbol{r})(\boldsymbol{S_2} \cdot \boldsymbol{r})}{r^5}\right] \tag{13}$$

and is described by nine components of the type:

$$\left(\frac{\mu_0}{4\pi}\right) g^2 \mu_B^2 \left[\frac{\delta_{ij}}{r^3} - 3\frac{ij}{r^5}\right] S_i S_j \tag{14}$$

where $i, j = x, y, z$ are the three orthogonal axes and S_i and S_j are the magnetic moment components of the individual electrons. Since both electrons are contained in molecular orbitals, the dipole interaction will have to be averaged on their respective probability distributions. The integrated form of dipole energy is:

$$E_{dip} = \sum_{i,j} D_{ij} S_i S_j \tag{15}$$

$$D_{ij} = \left(\frac{\mu_0}{4\pi}\right) g^2 \mu_B^2 \left\langle \left(\frac{\delta_{ij}}{r^3} - 3\frac{ij}{r^5}\right) \right\rangle \tag{16}$$

where D_{ij} are the components of the zero-field-splitting (ZFS) tensor. As for the g-tensor, a principal axes system that diagonalizes the ZFS tensor can be identified. Also, the ZFS is traceless (since it represents a dipolar interaction):

$$D_{XX} + D_{YY} + D_{ZZ} = 0 \tag{17}$$

Then, the ZFS interaction can be described through only two parameters, D and E, named ZFS parameters.

$$D = -\frac{3}{2} D_{ZZ} \tag{18}$$

$$E = \frac{1}{2}(D_{YY} - D_{XX}) \tag{19}$$

$$E_{dip} = D S_Z^2 + E(S_Y^2 - S_X^2) \tag{20}$$

The populations of the triplet sublevels are not the ones obtained from the Boltzmann distribution due to the spin selectivity of the processes that may populate the triplet, i.e. ISC, energy transfer and electron transfer. The non-equilibrium population of the spin sublevels is named spin polarization.

In the EPR spectrum of a triplet state, the energy of the transitions depends on the magnitude of the ZFS parameters, whereas the relative intensity on the spin polarization.

In the case of the EPR spectrum of triplet state of a single crystal, only two transitions will be visible for each orientation of the magnetic field relative to the crystallographic axes, and it will be possible to determine the ZFS parameters, the orientation of the principal axis system and the spin polarization.

In the case of a powder spectrum, represented in **Figure 10**, an overlap of transitions will be visible, with three pairs of features corresponding to the three principal axes of the ZFS tensor. In a powder or frozen solution, only the ZFS parameters and the spin polarization can be determined.

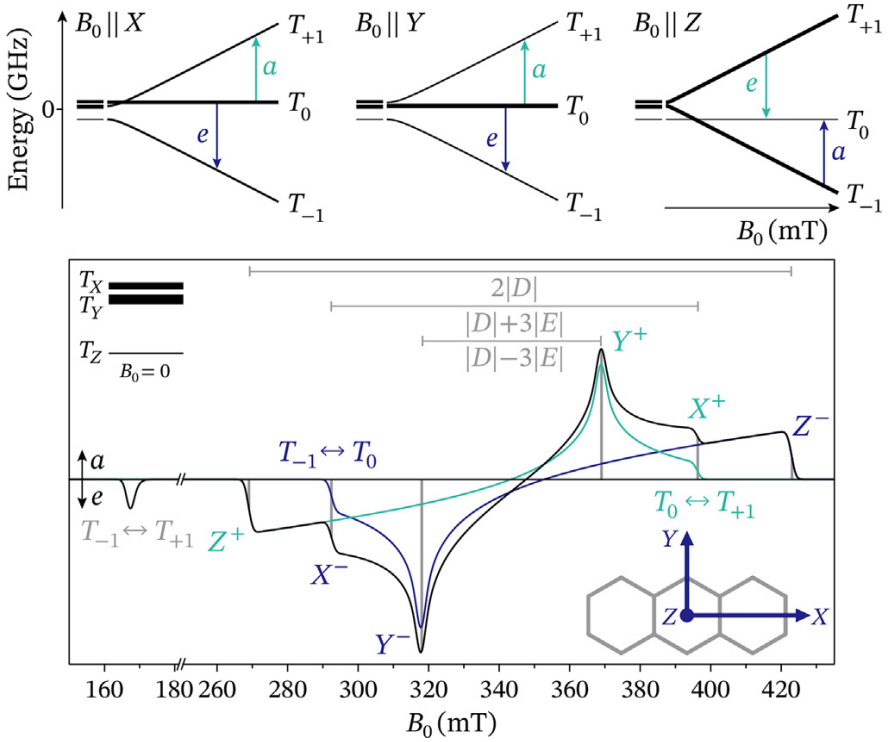

Figure 10: EPR spectrum of the anthracene triplet state formed by ISC and energies of the triplet sublevels as a function of an applied magnetic field oriented parallel to the principal axes of the ZF interaction matrix. The spectrum was simulated with ZF interaction parameters D = +2159 MHz and E = -246 MHz and relative sublevel populations ($p_X : p_Y : p_Z$ = 1 : 1.4 : 0.14). The contributions of the $m_s = -1 \leftrightarrow m_s = 0$ and $m_s = 0 \leftrightarrow m_s = +1$ transitions to the spectrum are shown in blue and green, respectively where a is absorption and e emission. The insets show the distribution of the populations across the T_X, T_Y and T_Z sublevels and the orientation of the principal axes of the ZF interaction matrix with respect to the molecular structure.[8]

2.2 Pulsed EPR

A relevant area of modern EPR is pulsed EPR. Pulsed experiments are characterized by sequences of EMR pulses that are used to stimulate energy transitions or create spin coherences in the system, as in NMR.

2.2.1 Boltzmann distribution

The electron spins of an ensemble are distributed between the α and β states. Since they are equivalent in absence of the B_0, half of the spins will be in the α state and half in the β state. Under these conditions, the magnetization vector is zero. If a B_0 is introduced, then due to the Zeeman effect the two spin states will no longer have the same energy and at thermal equilibrium the population of the β state will be slightly greater than α. The ratio of the populations of the two states depends on the temperature and the energy difference according to the Boltzmann equation:

$$\frac{N_\alpha}{N_\beta} = \exp\left(\frac{-g|\mu_B|B_0}{k_b T}\right) \tag{21}$$

where $k_b = 1.3806 \cdot 10^{-23}\, JK^{-1}$ is Boltzmann's constant and T is the temperature. Although the probability of a transition occurring from the $\alpha \rightarrow \beta$ state or vice versa from the $\beta \rightarrow \alpha$ state is identical, the population difference between α and β means that the number of photons absorbed is greater than those emitted. Therefore, it is possible to observe a net absorption signal.

2.2.2 Magnetization vector

To understand the effect of pulses on the spin system, it is necessary to introduce the magnetization vector model that allows a macroscopic interpretation. As we have already seen, an unpaired electron with $S = \frac{1}{2}$ can exist in two states. The behavior of a single electron respects the laws of quantum mechanics and is described through quantum properties. If, on the other hand, we consider an ensemble of identical and non-interacting electron spins, this can be described by the sum of the magnetic moments of the individual spin systems, called magnetization:

$$\boldsymbol{M} = \sum \mu_i \tag{22}$$

The use of the magnetization vector is versatile because it respects the physical laws of classical mechanics. Like any vector, it can be written in terms of the components: M_z, M_x, M_y. For a system at thermal equilibrium and interacting with the B_0, the magnetization will be aligned along the z-axis; i.e. parallel to B_0. Since magnetization originates from single electrons, it will be characterized by an angular momentum given by the sum of the spin angular moments:

$$\boldsymbol{J} = \sum \boldsymbol{S}_i \tag{23}$$

In this way it is possible to obtain the macroscopic analogue of the equation (1):

$$\boldsymbol{M} = g\mu_B \boldsymbol{J} \tag{24}$$

The time evolution of $\boldsymbol{M}$ in a generic magnetic field $\boldsymbol{B}$ is described by the following differential equation:

$$\frac{d\boldsymbol{M}}{dt} = \boldsymbol{M} \times g\mu_B \boldsymbol{B} \tag{25}$$

In presence of a constant magnetic field B_0, the spins will precede around the Z-axis, and the magnetization will align with the magnetic field. This motion is called the Larmor precession and is characterized by the Larmor frequency:

$$\omega_L = \frac{g\mu_B B_0}{\hbar} \tag{26}$$

2.2.3 Relaxation

In real systems, electron spins are not isolated but interact with surrounding molecules. This type of interaction is called spin-lattice (relaxation time T_1) and tends to bring the value of the M_z component back to the equilibrium value M_0. The other interaction type occurring in real systems is the one between electron spins (relaxation time T_2) and which tends to cancel out the M_x and M_y components. A graphic description of these relaxation phenomena is represented in **Figure 11**. These two system relaxation phenomena are described by the Bloch equations:

$$\frac{dM_z}{dt} = -M_y\omega_1 - \frac{(M_z - M_0)}{T_1} \tag{27}$$

$$\frac{dM_x}{dt} = -M_y(\omega - \omega_0) - \frac{M_x}{T_2} \tag{28}$$

$$\frac{dM_y}{dt} = M_z\omega_1 - M_x(\omega - \omega_0) \tag{29}$$

Where ω_0 is the precession frequency of $\boldsymbol{M}$ about the B_0, ω is the B_1 frequency and ω_1 the precession frequency of $\boldsymbol{M}$ about the B_1. Bloch's equations introduce two time constants, whose reciprocal corresponds to a kinetic constant. The first is the spin-lattice or longitudinal relaxation constant, T_1, the second is the spin-spin or transverse relaxation constant, T_2.

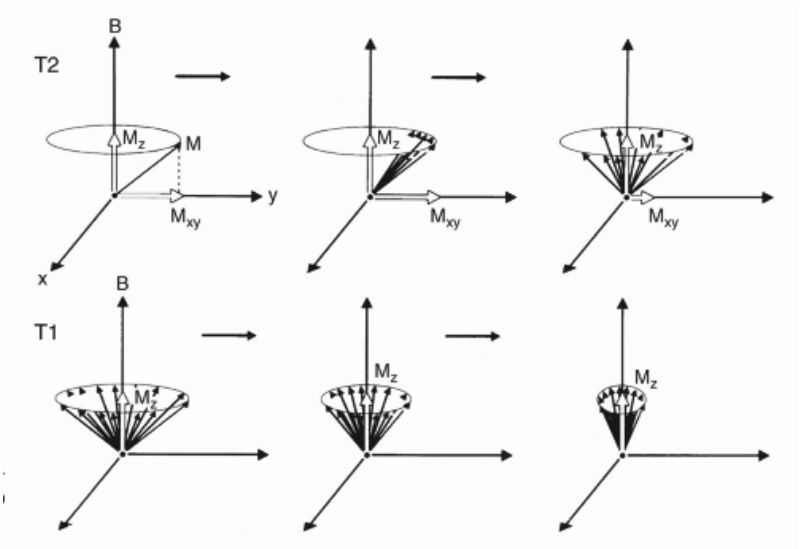

Figure 11: Through the vector model, the effect of the transverse relaxation of the $\boldsymbol{M}$ vector is represented at the top. The effect of the longitudinal relaxation on the $\boldsymbol{M}$ is visualized at the bottom.

2.2.4 Rotating frame reference system

To probe the properties of the system through pulsed EPR, EMR pulses are used to take the magnetization out of equilibrium. Before moving onto the description of the pulses, it is necessary to introduce the rotating frame reference system. In it, the z-axis coincides with the rotation axis for the xy plane, and the angular velocity of this rotation is the same as ω_L. In the rotating frame, the Larmor precession around B_0 gets removed as from **Figure 12**.

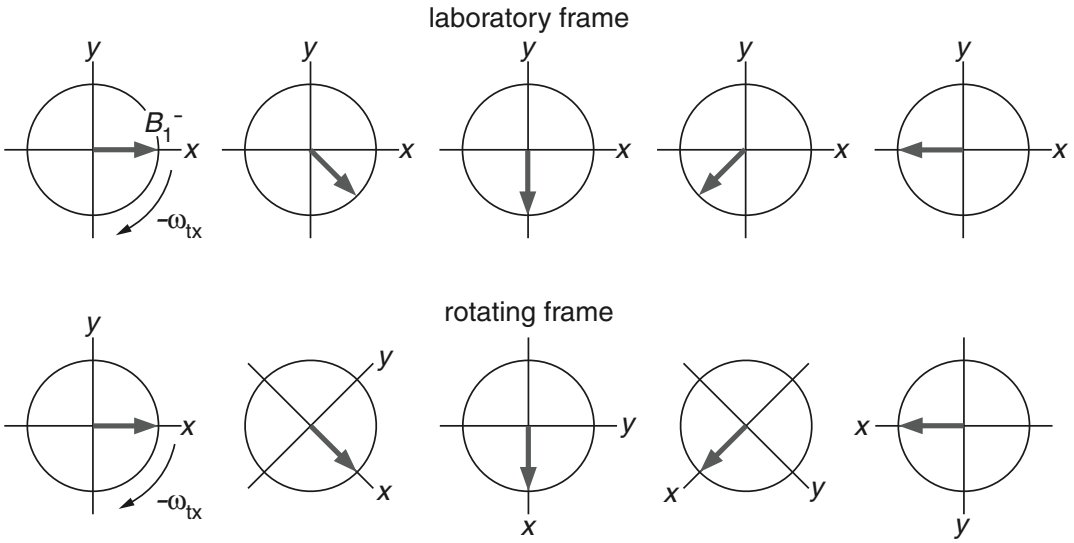

Figure 12: Precession of the magnetization in the rotary frame.

The rotating frame axes are labeled as X, Y and Z.

2.2.5 EMR pulses effect on the magnetization vector

In EPR spectroscopy, the magnetic component of an EMR is the one of interest, called B_1. As depicted in **Figure 13 (b)** it oscillates over time along the same direction. The effect of a pulse on $\boldsymbol{M}$ will be to bring it out of equilibrium. To give an intuitive explanation of the phenomenon, the rotating frame will be introduced. Since B_1 is a vector, it can be decomposed into other two vectors whose sum returns the original vector, as represented in **Figure 13 (a)**; specifically, two rotors named B_1^+ and B_1^-.

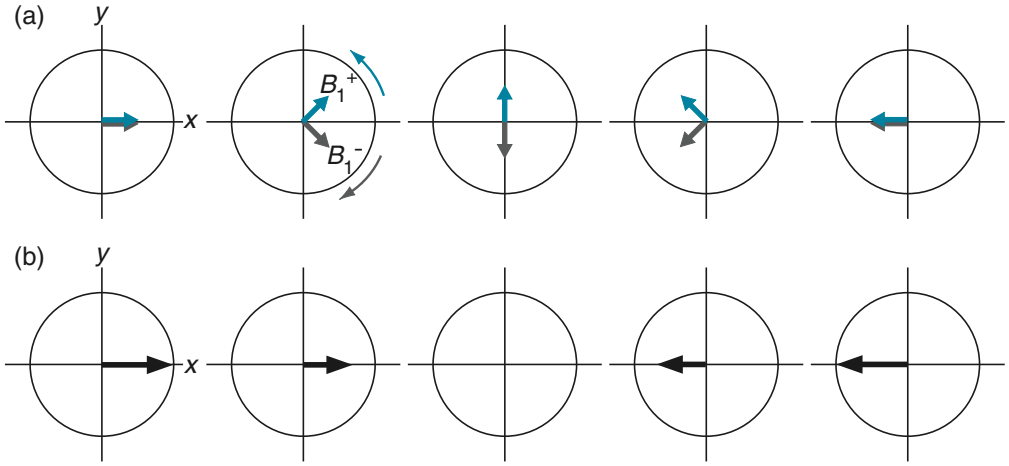

Figure 13: (a) Representation of the B_1^+ and B_1^- rotors. (b) Representation of the B_1 oscillation.

Let's consider just the B_1 component with counterclockwise rotation direction. If the B_1 is applied along the x-axis of the laboratory system and the EMR frequency coincides with ω_L, then its B_1^+ component will remain stationary on the XY plane of rotating frame and aligned along the X axis. At the same time the $\boldsymbol{M}$ will appear not to be preceding around the B_0. It's clear that the $\boldsymbol{M}$ will precede exclusively around the X axis, as depicted in **Figure 14**.

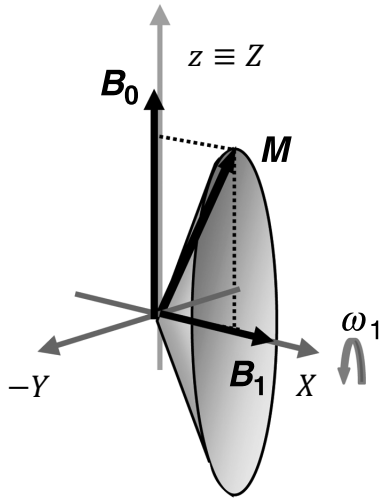

Figure 14: Precession of $\boldsymbol{M}$ around X during an x-pulse application.

Since the $\boldsymbol{M}$ precedes around the X-axis only during the application of the pulse, it is possible to control the final $\boldsymbol{M}$ position by adjusting the pulse application duration. For each pulse the final position will be:

Pulse along x: $M_z = M_z \cos \omega_1 t \quad M_y = -M_z \sin \omega_1 t$ (30)

Pulse along $-x$: $M_z = M_z \cos \omega_1 t \quad M_y = M_z \sin \omega_1 t$ (31)

Pulse along y: $M_z = M_z \cos \omega_1 t \quad M_x = M_z \sin \omega_1 t$ (32)

Pulse along $-y$: $M_z = M_z \cos \omega_1 t \quad M_x = -M_z \sin \omega_1 t$ (33)

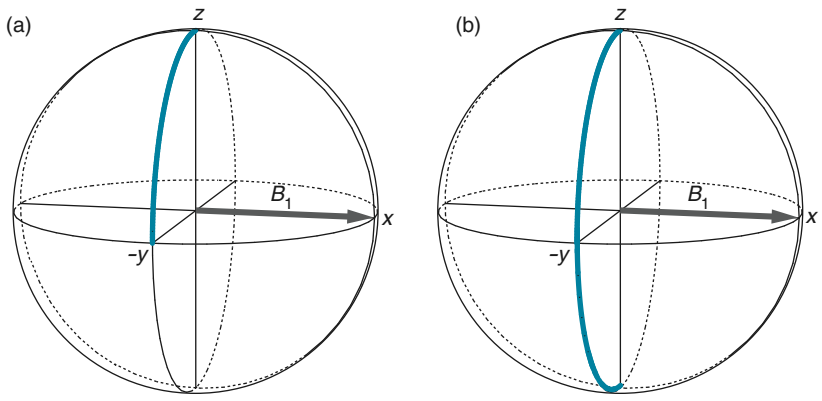

Figure 15: Effect of two different pulses on the $\boldsymbol{M}$: (a) 90° pulses along x interconverting the M_z to the M_y one; (b) 180° pulses along x changing sign of the M_z component.

Microwave pulses are typically applied as either 90° (π/2) or 180° (π) pulses, denoting the angle by which the magnetization is rotated: depending on the spin and the instrumental conditions π/2 or π pulses vary in duration and amplitude. **Figure 15** represents the effect of the pulses on $\boldsymbol{M}$. A 180° pulse can be produced either by doubling the length of a 90° pulse at the same power, or by applying the same length with double field strength (B_1).

2.3 Pulsed experiments

2.3.1 EDEPR

Echo Detected EPR Spectroscopy is a technique that allows the observation of paramagnetic species using the spin echo phenomenon for signal acquisition. The direct acquisition of a free induction decay after a single π/2 can be inaccessible due to fast relaxations and long instrumental dead time. This inconvenience can be solved by refocusing the free induction decay into a spin echo after the dead time. The simplest pulse sequence to get a spin echo is the Hahn Echo sequence: $\pi/2 - \Delta - \pi - \Delta$ which is shown in **Figure 16** and that generates a so-called Primary Echo.

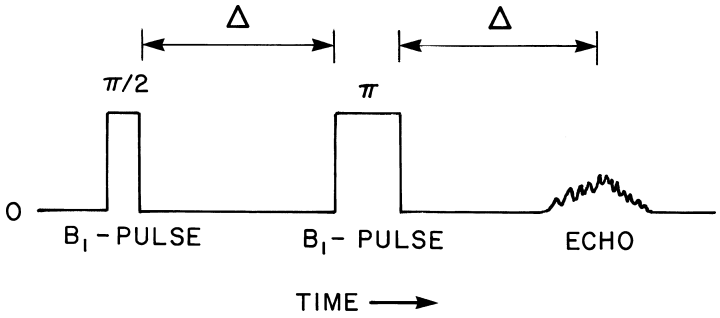

Figure 16: The Hahn B1-pulse sequence: $\pi/2 - \Delta - \pi - \Delta - echo$.

The firs $\pi/2$ pulse rotates the net magnetization M_z from the z-axis to the xy-plane, bringing the spins into phase coherence. The spin packets then begin to dephase and precess in the xy-plane at their respective Larmor frequencies. After a defined delay time Δ, a π pulse is applied, inverting all spins by 180°. While maintaining their individual precession frequencies and directions, the spins start to rephase. A graphical representation of $\boldsymbol{M}$ movement is depicted in **Figure 17**. The transverse magnetization, which reaches its maximum after a total time of 2Δ, constitutes the Hahn Echo. This sequence allows to recover the loss of magnetization related to local field inhomogeneity but does not permit to recover the irreversible loss of magnetization caused by transverse relaxation processes.

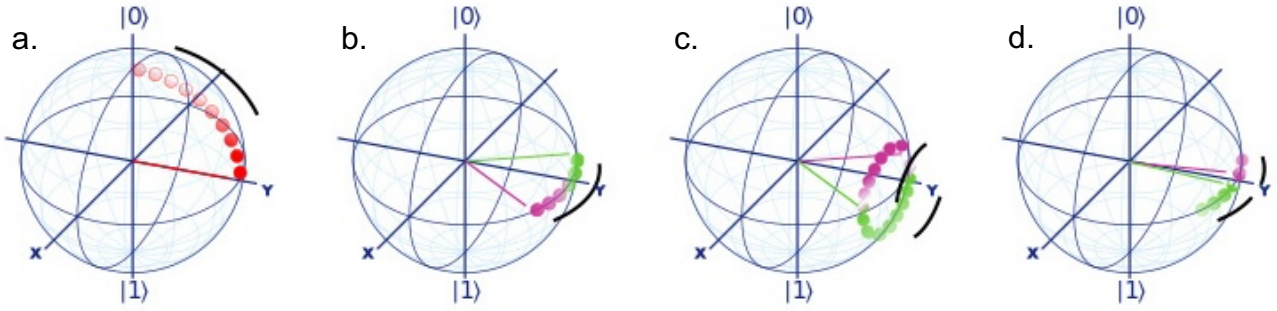

*Figure 17: Visual representation of the spin packets evolution over time (**a**) during the first π/2 pulse, (**b**) during the first Δ delay, (**c**) during the second π pulse and (**d**) during the second Δ delay.*

The ED-EPR spectrum is recorded by repeating the pulse sequence at different values of the magnetic field and plotting the integrated echo intensity. Note that differently from conventional EPR, the ED-EPR lineshape is not in derivative, but in absorption.

While this technique allows easy detection of stable radicals, for triplet species the synchronization of the pulse sequence with a photoexcitation via laser pulses is required. Introducing a laser pulse at the beginning of the Hahn Echo sequence, it is possible to populate (almost instantly on the EPR timescale) the triplet state to be studied. When both

a stable radical and a triplet state are present, their contributions can be isolated by repeating the same experiment in the dark (radical only) and under laser irradiation (triplet + radical). By subtracting the two spectra the triplet ED-EPR can be obtained.

2.3.2 DEER

The most widely employed pulsed dipolar spectroscopy (PDS) experiment is Double Electron–Electron Resonance (DEER). The 4 pulses DEER experiment has become the standard method for measuring distances between electron spins in biomacromolecules, typically in the range of ~1.5 – 6 nm, and in exceptional cases up to ~8 nm. Importantly, this technique can yield not only a single mean distance but also the full distance distribution, thereby enabling the characterization of conformational ensembles in proteins on the nanometer scale[9]. The pulse sequence of the four-pulse DEER experiment is illustrated in **Figure 18**.

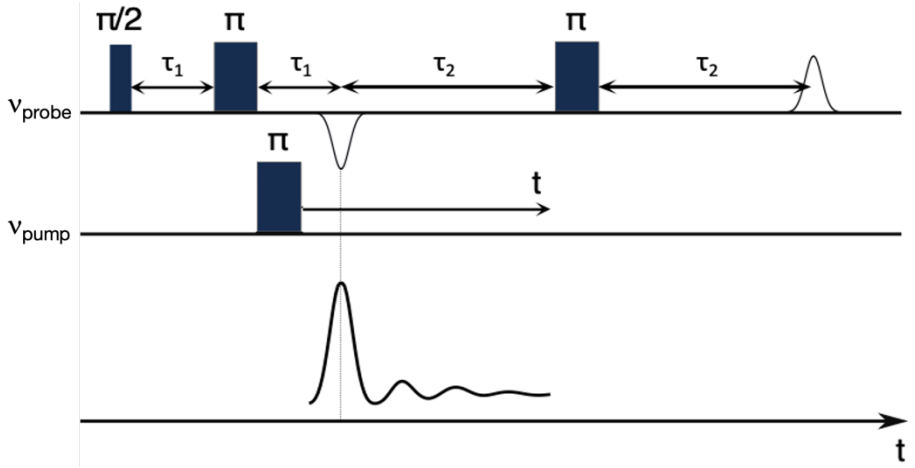

Figure 18: Pulse sequence of the four-pulse DEER experiment. Delays τ_1 and τ_2 are kept fixed, while the delay between the first π-pulse and the pump pulse is varied. The echo intensity V(t) is recorded.

The DEER experiment operates at two microwave frequencies: the detection frequency ν_{probe} which is in resonance with spin *A*, and the pump frequency ν_{pump} which is in resonance with spin *B*. A Hahn-echo sequence at the detection frequency ν_{probe} generates the spin *A* echo. A π-pulse at the pump frequency ν_{pump}, inverts spin *B* and if both spins *A* and *B* are dipolar-coupled the inversion of spin *B* changes the local magnetic field at spin *A* and shifts its Larmor frequency by ω_{dd}. The second π-pulse applied at the detection ν_{probe} frequency refocuses the Hahn echo and generates an inverted, refocused echo whose intensity is changed due to the resulting phase shift of $\pm\omega_{dd} \cdot t$, where t is the dipolar evolution time. Increasing the delay between the first π-pulse and the pump pulse will cause oscillations in the echo intensity forming the DEER time trace, from which distance distributions can be extracted.

In general, DEER performs optimally for spin pairs with comparable longitudinal relaxation times, T_1, and moderately broad EPR spectra. In fact, the detection and pump pulses must be separated by a sufficient frequency offset to selectively excite spins *A* and *B* without pulse overlap, which could introduce artefacts into the time trace. At the same time, the spectral width should remain narrow enough to ensure that a sufficient fraction of spins is excited, thus maintaining good sensitivity. In this thesis work, DEER experiments were carried out to measure NO•–TT•$^-$ distances. Nitroxide and TT radicals are a prominent example of spin labels ideally suited for DEER measurements, as their spectral width and frequency offset

allows for efficient application of detection and pump pulses. As the two signals are partially overlapped, tuning the TT•- generation is required to improve signal intensity.

2.3.3 ReLaser-IMD

Much effort has been invested to research alternative probes that can be used as endogenous paramagnetic centers. Laser induced pulsed dipolar spectroscopies (LiPDS) are methods designed to measure the dipolar interaction either between a permanent spin center and a photoexcited triplet state or between two photoexcited triplets. All LiPDS methods employ one or more laser pulses to generate a triplet state.[10] The focus of this thesis is on systems involving a stable paramagnetic species interacting with a photoexcited triplet, which in our case is represented by the nitroxide radical-triplet state terthiophene interaction. Among the various LiPDS techniques, the one employed in this project is the ReLaser-IMD method.

ReLaser-IMD exploits the paramagnetic property of the triplet which allows it to be used as a pump spin. Upon photoexcitation with a laser pulse, the spin state of the photo-activated triplet changes the spin state of the moiety from $S = 0$ (singlet state) to $S = 1$ (triplet state). As in the triplet state $m_s = [-1, 0, +1]$, it leads to a variation in the dipolar interaction between the spin labels. The effect of the laser pulse is equivalent to the microwave pump pulse in the DEER experiment[30]. Increasing the delay between the first π-pulse and the laser pulse will cause oscillations in the echo intensity form the ReLaser-IMD time trace, from which distance distributions can be extracted. As the optical pulse does not interfere with the microwave ones, they can be applied simultaneously[11].

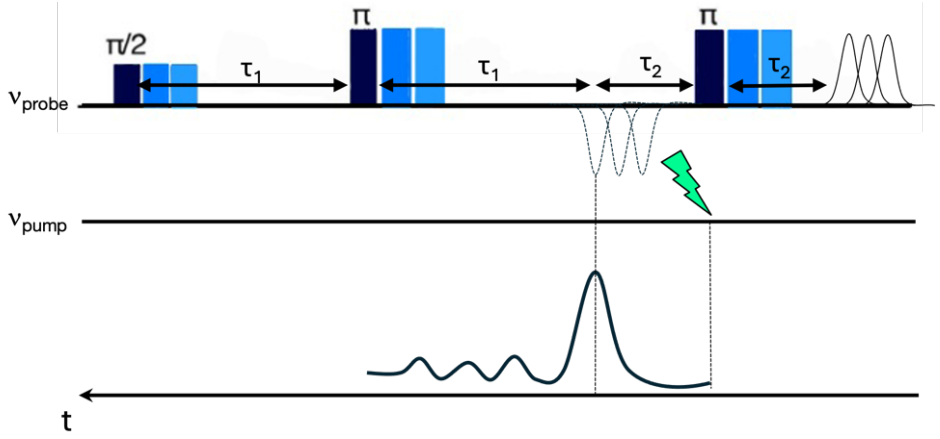

Figure 19: ReLaser-IMD pulse sequence. The probe pulse sequence is the same as the DEER one, while the pump pulse is substituted by a laser pulse. The laser pulse remains fixed in time while the whole microwave probe sequence is delayed relative to it.

The ReLaser-IMD experiment is performed in practice by applying a Refocused Hahn Echo sequence to the nitroxide (like DEER technique) and delaying this whole pulse sequence over time with respect to the fixed laser pulse event, as depicted in **Figure 19**. The resulting trace will be symmetric relative to the zero time at the intensity maximum: the obtainment of a well-defined zero time is the main advantage of the ReLaser-IMD experiment relative to other LiPDS techniques.

Compared to nitroxide–nitroxide DEER, ReLaser-IMD is expected to provide higher sensitivity and greater modulation depth. This is because only a single microwave frequency is required, which can be tuned to the center of a critically coupled resonator. This setup allows the use of short observer pulses applied at the nitroxide spectrum maximum, thereby maximizing the number of excited observer spins and improving the signal-to-noise ratio

(SNR).[12] Unlike bandwidth-limited microwave pump pulse, a laser flash can excite chromophores in all possible orientations relative to the external magnetic field, effectively covering the entire triplet EPR spectrum. This eliminates orientation selection for the pumped spin and can potentially enhance the modulation depth.[12] In DEER, the shortest measurable distance is constrained by the limited excitation bandwidth, but in ReLaser-IMD the lower distance limit is defined solely by the observer pulse duration.[12] For example, with a π pulse length of 20 ns, distances as short as 1.2 nm can be detected -significantly below the ~1.5 nm limit of DEER. However, as a refocus sequence is used, species with a large T_2 must be used to prevent the irreversible signal loss over a long pulse sequence. Using species with moderately long T_2 will limit the shortest detectable distance. In the end, by increasing the triplet quantum yield, ReLaser-IMD can extend the upper measurable distance range, shorten acquisition times, or allow measurements at lower concentrations than those typically used in DEER.

3 SDSL

Since a peptide is not naturally visible to the EPR, at least one spin probe must be covalently attached to it. There are two probe types, the radical ones and the photo excitable ones. The former are stable radical species such as nitroxides (for example SPIRO, MTSL, MSL, **3.3**). The latter are species in which it is possible to induce the triplet state through photo excitation, such as porphyrins, fullerenes, or other chromophores with a good triplet state yield.

Since the application of EPR to structural biology involves measuring distances, it will be necessary to be able to attach probes to specific positions in the AA sequence. Site direct spin labeling (SDSL) techniques are used to control the number of probes that can attach to a peptide or protein.[13,14] They are a set of reactions that selectively involve only one or two of the AAs of the protein or peptide; some of them are reported in **Figure 20**. This way, the probe will bind to all positions of the peptide or protein where the amino acid chosen to make SDSL is present. The amino acid most chosen to make SDSL (as well as the one used in this thesis) is Cys, as it is the only AA containing the sulfide group.

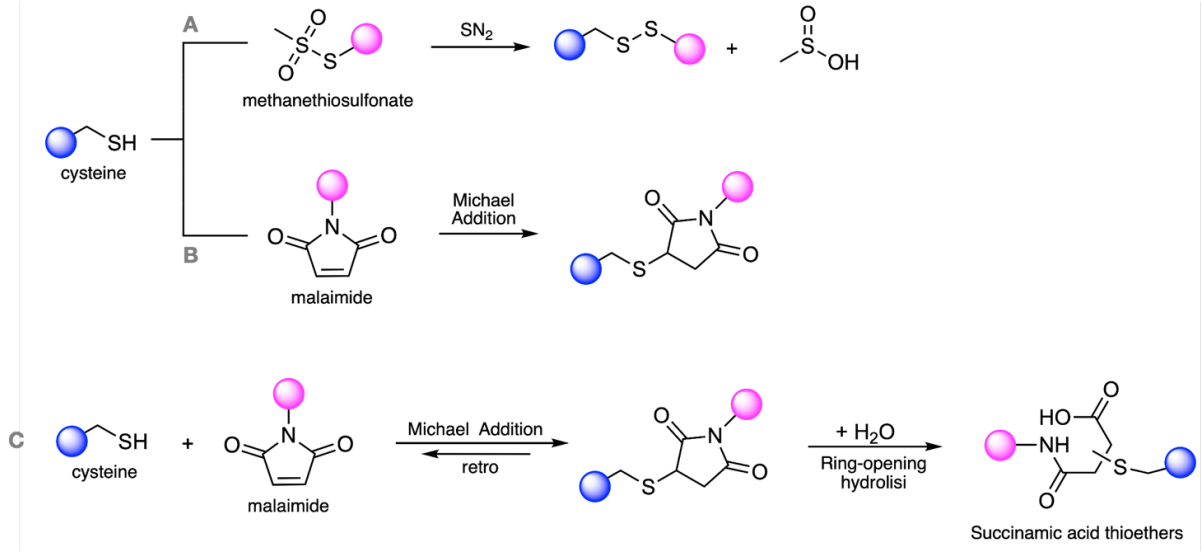

Figure 20: Two common labeling strategies. The first one involving the methanethiosulfonate group and the second involving the malaimide group. For the second one the ring opening reaction is suggested to increase the reaction yield.

Clearly, SDSL techniques alone are not enough. In the case of a peptide that is produced with the synthesizer, it is easy to introduce the desired AAs. For proteins, because they are synthesized by bacteria, site-direct mutagenesis (SDM) will be needed. It is a set of techniques that allow specific changes to be made to the DNA sequence encoding the protein. In this way, it will be possible to make the bacterium synthesize the modified protein, in which the AAs of specific positions will have been replaced by the desired one. Consider a protein in which Cys is natively absent, such as CaM. By combining SDM with SDSL it will be possible to replace the amino acid at a certain position in the sequence with a Cys to bind the spin probe on it.

3.1 Terthiophene as a novel spin label

Thiophene oligomers have been traditionally studied as building blocks for polythiophene. Oligothiophene properties guided most of the research on the development of molecular electronic devices.[15] Chemical or electrochemical reduction[15] leads to radical cations and di-cations with characteristic optical absorptions. TT radicals can also be obtained through direct photogeneration from the singlet state using high excitation energy.[16]

Although many theoretical and experimental studies have dealt with the optical properties of the redox states, only little has been published on the electronic properties of photoexcited states. In a 1992 paper the EPR spectra of photoexcited triplet state of oligothiophenes (n=2–8) have been reported.[15] Moreover, no experimental studies have been conducted applying terthiophene as a photoexcitable spin label. The use of TT in the biological environment represents a novelty of great interest.

3.2 Terthiophene and labeling reaction

The aim of this thesis was to test the terthiophene (TT) as a novel photo excitable spin label for pulsed EPR spectroscopy. Upon excitation with 355 nm laser pulses, TT populates the triplet state. At the same wavelength, it also forms the radical anion[15], raising the question whether TT is more suitable for Laser-IMD or DEER measurements.

The label was designed as a terthiophene bonded to an acetyl-imidazole, TTAI (**Figure 21**), and was synthesized by the group of Prof. Alessia Colombo (Univ. degli Studi di Milano).

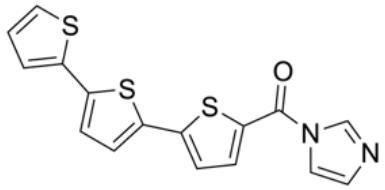

Figure 21: The terthiophen-acetyl-imidazole tested as a spin label.

The acetyl-imidazole was chosen instead of the more common maleimide or methanethiosulfonate linking groups, because it links the label to the sulfur atom of cysteine residues on the peptide or the protein through just one atom. This feature is of particular interest because usually the probes visible to the EPR are linked to peptides through bridges of much greater length than a single atom. Having such a short linker has been shown to limit conformational flexibility and to produce narrow distance distributions.[17–19]

As can be seen from **Figure 22**, the labeling involves a nucleophilic attack reaction on the carbonyl carbon of the probe by cysteine sulfide anion. Imidazole was chosen as the leaving group.

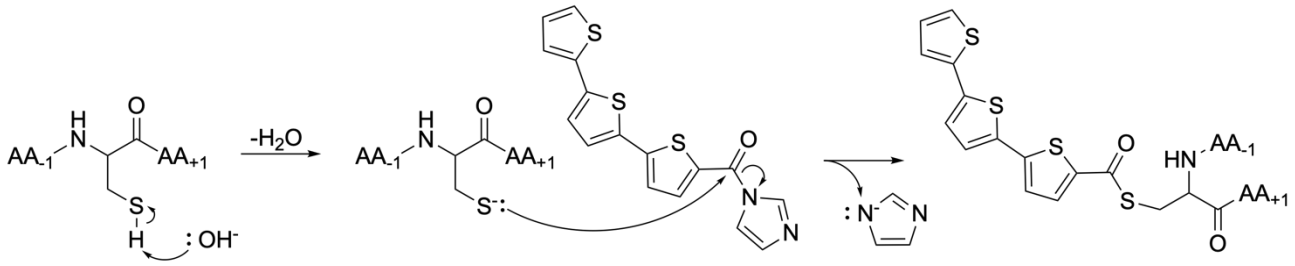

Figure 22: Reaction mechanism for the labeling reaction. First the sulfide anion is formed in solution, then the TTAI undergoes nucleophilic substitution, while imidazole acts as the leaving group.

The chosen labeling sites are cysteine residues on the N-terminus of the M13 peptide (see paragraph **1**) and the CaM E6C mutant, where the native glutamic acid residue had been mutated to a cysteine. Note that of the three available single mutants (see paragraph **10.2**) the E6C mutant is the one having the greatest solvent accessibility of the three in all CaM conformations, thus favoring the labeling reaction.

3.3 SPIRO

The most widely used class of spin probes are nitroxide radicals. These molecules consist of a heterocycle containing the NO• group. The unpaired electron is contained in the π orbital of the N-O bond and delocalized with spin densities around 60% on oxygen and 40% on nitrogen. Like all radicals, it tends to undergo redox reactions. The biological environment favors the redox reaction and it's shown in **Figure 23**. To increase their stability, bulky groups are bound to the α-carbons to limit the accessibility of the radical to collisions with other molecules. Radicals of this type are stable up to 140°C, resistant to slightly reducing environments and unstable only at extremely low pH.

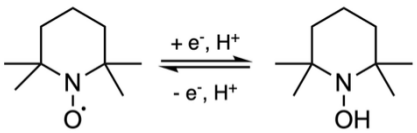

Figure 23: Redox scheme of (2,2,6,6-tetramethylpiperidin-1-yl)oxyl (TEMPO) with the nitroxide radical to the reduced hydroxylamine.

The size of the nitroxide ring influences the redox stability of the radical. This stabilizing effect increases as shown in **Figure 24 (A)**. The nitroxide radical stability also depends on the choice of functional groups that are attached to the α-carbons. The extent of the stabilizing effect given by the substituent group is reported in **Figure 24 (B)**. The methyl substituent guarantees the least stabilizing capacity, while the ethyl group the greatest. In the middle are the cycloexyl rings which are bulkier than methyl groups but more rigid than ethyl groups and adopt a twisted boat geometry that leaves the N-O bond partially exposed.[20] It can be deduced that as the freedom of rotational motion of the substituents increases, the stability of nitroxide increases.

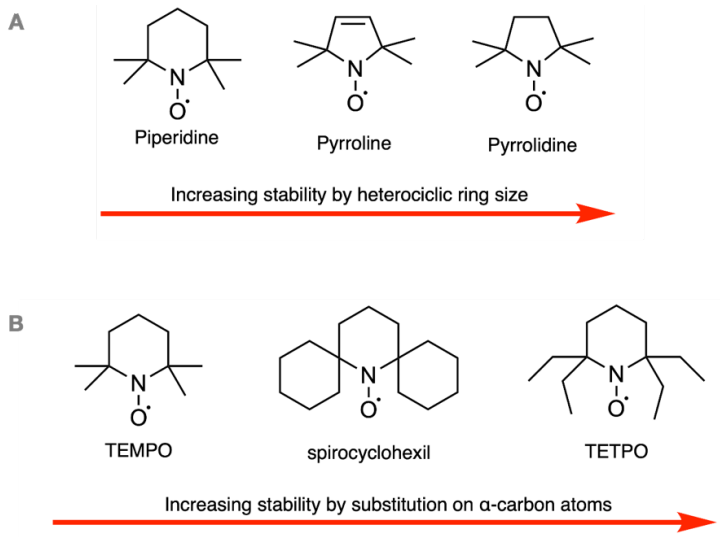

Figure 24: Substitution pattern on the α-carbon atoms as a structural factor contributing to nitroxide stability toward reduction.

To ensure the quality of the signal measured by DEER technique, it is necessary to maximize the transverse relaxation time, T_2. Increasing T_2 results in a better signal-to-noise ratio and the ability to measure long distances. In the solid state, it's influenced by the local microscopic environment of the nitroxide. Rotating methyl side groups are among the main contributors to the T_2 shortening.[20] The effect of the substituent group on the T_2 is reported in **Figure 25**. The use of ethyl groups instead of the methyl ones increases the reduction stability of the nitroxide and mildly increases the T_2. But, for DEER techniques it is preferable to use a probe in which the carbons are replaced by rigid molecules, such as cyclohexyl rings, increasing T_2 even more.[21,22]

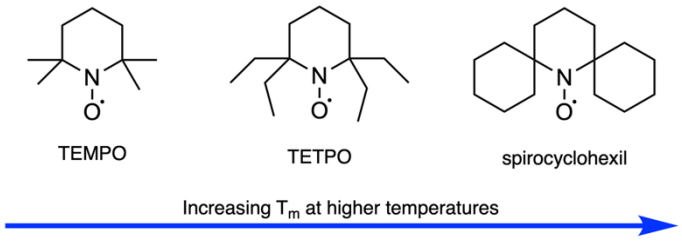

Figure 25: Substitution pattern on the α-carbon atoms influencing the nitroxide relaxation parameters.

The SPIRO spin label is a five-membered nitroxide ring with two spiro-cyclohexyl rings in α and in which the maleimide group has been attached to the β-carbon of the heterocycle. The maleimide acts as a bridge for selective attachment to the cysteine sulfide group. The cysteine SDSL for the SPIRO spin label is reported in **Figure 26**.

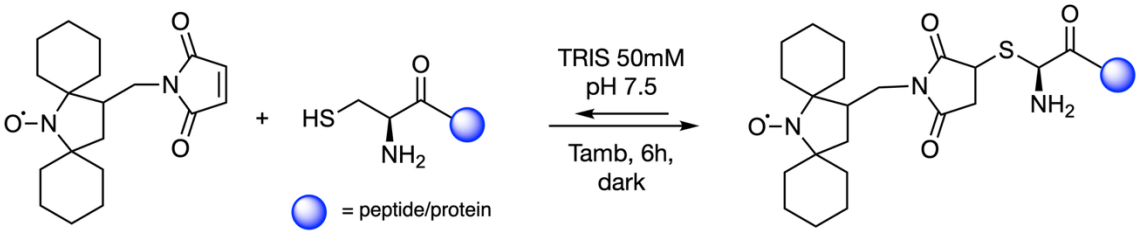

Figure 26: Reaction between the SPIRO nitroxide spin label containing a maleimide group, whose electron-poor double bond is attacked by the thiol group of cysteine (Michael reaction). A C–S bond is formed, linking the protein or peptide to the probe.

4 Reverse Phase Chromatography (RPC)

4.1 RPC Theory

RPC has become increasingly important for high-resolution separation and analysis of proteins, peptides, and nucleic acids. RPC separates molecules according to differences in their hydrophobicity.

Separation relies on sample molecules existing in an equilibrium between the mobile phase (water/organic solvent mixture) and the surface of the resin (the stationary phase). The distribution of the sample depends on the properties of the resin, the hydrophobicity of the sample, and the composition of the mobile phase. Initially, conditions favor an extreme equilibrium state where essentially 100% of the sample is bound.

To initiate elution, the amount of organic solvent is increased so that conditions become more hydrophobic. Binding and elution occur continuously as sample moves through the column. The process of moving through the column is slower for those samples that are more hydrophobic. Consequently, samples are eluted in order of increasing hydrophobicity.[23]

RPC steps are reported in **Figure 27**.

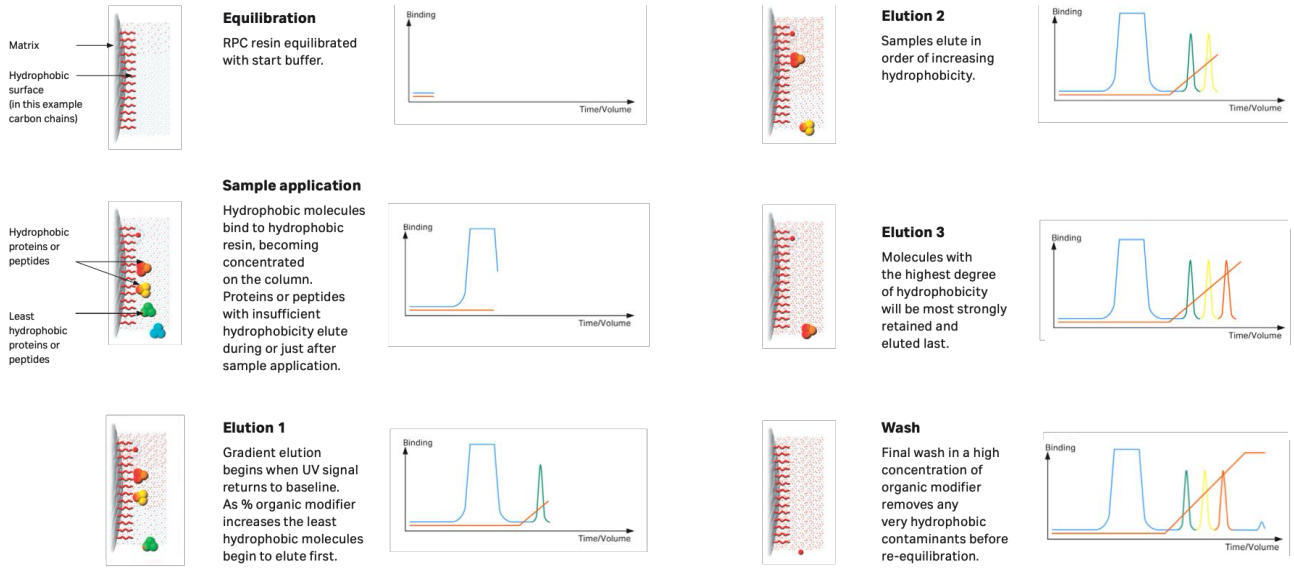

Figure 27: Steps involved in an RPC separation using gradient elution.[12]

4.2 Components of a RPC resin

From the several possible existing resins, we employed a SOURCE™15RPC prepacked column with naked, polystyrene-based, hydrophobic polymer matrix (**Figure 28**). Synthetic organic polymers, such as beaded polystyrene, provide excellent chemical stability, particularly under strongly acidic or basic conditions (from pH 1.0 to pH 12.0). These stable matrices offer key advantages when separating complex mixtures of protein or peptide: a broad working pH range offers greater control over selectivity; greater chemical stability facilitates any cleaning that may be required after working with biological samples. In addition, high physical stability and uniform particles facilitate high flow rates, particularly during cleaning or re-equilibration steps, thereby improving throughput and productivity and minimizing back pressure.[23]

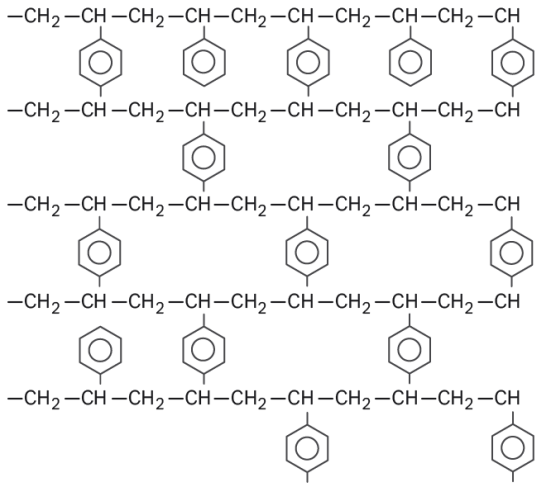

Figure 28: Partial structure of a polystyrene-based RPC resin.[23]

4.3 Ion pairing

Optimum pH is one of the most important parameters to establish since the properties of proteins and peptides can alter significantly at different pH values.

A common way to increase the hydrophobicity of charged components, enhance binding to the resin, and so alter retention time, is to add ion-pairing agents to the buffer. These agents bind via ionic interactions with charged groups and thereby suppress their influence on overall hydrophobicity (**Figure 29**). Since most proteins and peptides are slightly basic, ion-pairing agents are often acids such as trifluoroacetic acid (TFA) whereas a base such as triethylamine is used for negatively charged molecules.

In some cases, the addition of ion-pairing agents is an absolute requirement for binding to the RPC resin. For example, an ion-pairing agent such as TFA is essential to ensure the binding of hydrophilic peptides, like the M13 peptide. The type and concentration of an ion-pairing agent can also affect retention behavior and subsequent selectivity.[12]

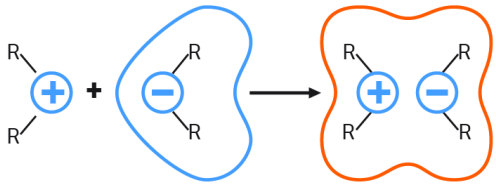

Figure 29: Ion-pairing agents alter net hydrophobic properties.[23]

Materials and methods

5 Labeling procedures

5.1 CaM E6C labeling procedure

A total of 16 stock 100 μL solutions of TTAI 3 mM in DMSO were prepared. The stock solution was then kept at -80°C and protected from light to prevent photodegradation.

The first labeling attempt was performed on the CaM E6C mutant:

- 1.25 mL of CaM E6C 40 μM in aqueous solution of 50 mM TRIS at pH=7 was treated with 1.5 μL of 1 M DTT to break any disulfide bridge and to increase the effectiveness of the labeling. The solution was left reacting for 30 min at 4°C.
- At the end of the reaction, the solution volume was increased to 2.5 mL, and the DTT was removed by a PD10 pre-packed size exclusion column of 5 kDa cutoff. The fraction eluted from the column came out diluted to 3.5 mL, so it was concentrated down to 2.5 mL using a concentrator in a thermostatically controlled centrifuge at 4°C.
- 70 μL of TT 3 mM were added to the concentrated solution and paying attention to obtain approximately 2.5 mL of total reaction volume. The labeling reaction was left 20 h under magnetic stirring and in the dark.
- After the necessary time, another PD10 column was used to remove the unreacted TT and to isolate the protein. Same as in the second point, the fraction eluted from the column came out diluted to 3.5 mL
- The labeled protein was concentrated and characterized by UV-Vis spectroscopy.

Despite the molar excess of label (approximately 4x) and the long reaction time, the yield of the labeling reaction for CaM E6C was only around 20%. Considering the impossibility of separating the labeled and unlabeled proteins, this yield percentage was too low to be able to obtain valid data from DEER and Laser-IMD techniques. No further attempts were made to label the protein. All efforts were concentrated on the labeling of the peptide which is more stable and easier to purify.

5.2 M13C labeling procedure

Several tests were performed trying to improve the labeling conditions and therefore yield. First purification attempts were conducted using chloroform extractions to remove unreacted label and proved to be inefficient. No DEER and ReLaser-IMD signal could be detected from samples prepared using the purified peptide. Reverse phase chromatography (RPC) was used to provide more efficient peptide purification. Amongst all the trials, the steps for the best M13C labeling procedure with the TTAI probe are as follows:

- An excess of TTAI equal to 12 times the moles of peptide was used. TTAI (100 μL, 3 mM, in DMSO) was added to M13C (300 μL, 5 mM, in 50 mM TRIS buffer solution, pH=8.0). A 75% H2O, 25% DMSO solution is obtained with a 12-fold molar excess of TTAI.
- The solution was incubated for 20 hours at room temperature, in the dark and under magnetic stirring.
- After the necessary time, the reaction mixture was transferred to an Eppendorf tube and centrifuged with a MiniSpin® centrifuge at 13400 rpm for 2 min to precipitate the

unreacted probe. It is important to remove as much unreacted TTAI as possible to avoid clogging the column in the following steps.

- After centrifugation, the supernatant was collected in another Eppendorf tube and placed under nitrogen flow to evaporate the greater part of the DMSO. It is not possible to use the freeze dryer on the DMSO/H_2O solution or inject the solution directly in the RPC due to the presence of DMSO which in the first case would damage the membranes of the vacuum pump and in the second, being in a concentration greater than 10%, it would decrease the resolution of the chromatogram peaks, enlarging them.
- The yellow solid residue obtained after evaporation was dissolved in 600 μL of MilliQ and centrifuged again with MiniSpin® at 13400 rpm for 2 min to further precipitate any residual excess TTAI.

The yield of the labeling reaction for M13TT was around 40%. The labeled peptide was then isolated through RPC and kept at -80°C.

6 Chromatography

The labelled peptide was purified using reverse phase chromatography on our ÄKTA pure™ 150. The sample solution was introduced by loading 500 µL of analyte into the injection loop. A pre-packed Cytiva RESOURCE™ 15RPC ST 4.6/100 column was used; the stationary phase consisting of rigid, monodisperse polystyrene/divinylbenzene beads with a diameter of 15 µm.

The first elution attempt was performed without ion paring agent, the mobile phase consisted of two eluents: Milli-Q water (eluent A'), and a 9:1 mixture of acetonitrile and Milli-Q water (eluent B').

The rest of the elutions were carried out after proving the M13TT stability in a 0.1% TFA solution. For those, the mobile phase consisted of two eluents: 0.1% TFA in Milli-Q water (eluent A), and 0.1% TFA in a 9:1 mixture of acetonitrile and Milli-Q water (eluent B).

To isolate the labeled peptide, a previously devised RPC protocol for labeled M13C purification, reported in **Figure 30**, was employed. Chromatographic separation was carried out at a flow rate of 1 mL/min using a time-dependent gradient. The initial mobile phase composition was maintained at 10% eluent B for 3 column volumes (CV; 1 CV = 1.66 mL), changed linearly to 30% in 3 CV and held at that composition for 2 CV. This was followed by a linear gradient to 60% eluent B over 17 CV. Finally, 100%B was applied for 10 CV to clean the column from any residual hydrophobic probes. The column was then brought back to 10% eluent B in 5 CV and equilibrated. Eluted fractions were collected using an F9-R fraction collector, which was set to switch collection tubes every 1.5 mL. Data acquisition was performed using the UNICORN software.

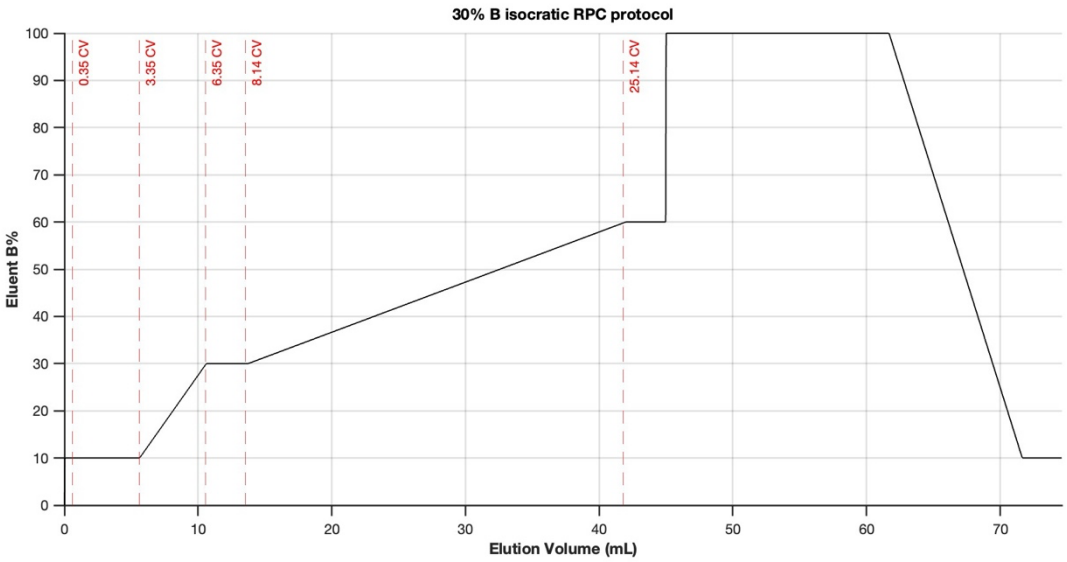

Figure 30: Elution protocol previously devised to purify M13C labeled with other spin probes and used in this project for the M13TT purification.

.

An alternative elution protocol, reported in **Figure 31**, was tested using the products of a labeling reaction carried out using the TTAI recovered from other labeling reactions. The initial mobile phase composition was maintained at 0% eluent B for 3 column volumes (CV; 1 CV = 1.66 mL), then slowly changed linearly to 60% eluent B in 36 CV. This was followed by a linear gradient to 60% eluent B over 2 CV. Finally, 100%B was applied for 8 CV to clean the column from any residual hydrophobic probes. The column was then brought back to 0% eluent B in 5 CV and equilibrated. Eluted fractions were collected using an F9-R fraction collector, which was set to switch collection tubes every 1.5 mL. Data acquisition was performed using UNICORN software.

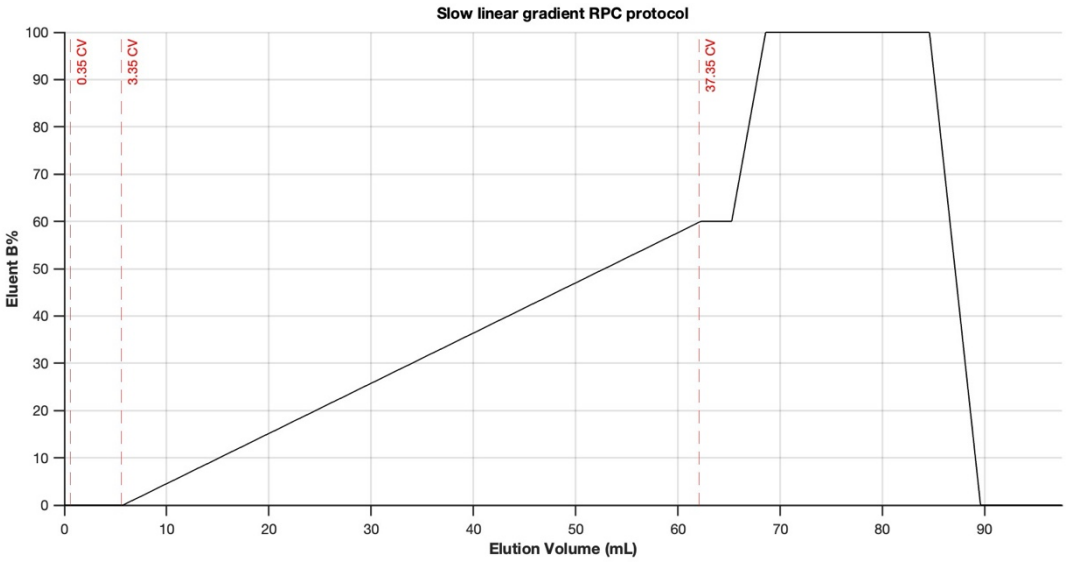

Figure 31: Elution protocol with a slow linear gradient devised trying to enhance the M13TT purification.

Isolated fractions were then analyzed through UV-Vis spectroscopy.

7 UV-Vis characterization

M13C, TT, M13TT and RPC fractions of interest spectra were acquired using the JASCO dual-beam spectrometer V-730ST UV-Vis spectrophotometer equipped with a deuterium lamp for the acquisition of spectra in the range 190-230 nm and a tungsten-halogen lamp for the range 230-700 nm. Measurements were made with a scanning speed of 200 nm/min using a low-volume quartz cuvette with a 1 cm optical path.

8 Circular dichroism (CD)

The main purpose of this technique was to assess the structural relationships between CaM100S in presence of unlabeled (M13C) or labeled (M13TT) peptide, to confirm that the individual domains of this multi-domain protein were correctly folded and remained intact after the labeling procedure. A maintained secondary structure is an essential prerequisite before detailed structural studies such as SDSL-EPR, since conformational changes induced by SDSL might affect protein function.

To verify this, CD spectra of CaM100S-M13C and CaM100S-M13TT in presence of a 20-fold excess of Ca^{+2} (essential for its ability to bind to target peptides), were recorded and compared (**Figure 57**, later in the text).

The following samples were prepared:

- The CaM100S-M13C sample was prepared from stock solution introducing CaM100S 0.5 nmol, M13C 0.6 nmol and Ca^{2+} 10 nmol in a total volume of 50 μL of MilliQ water.
- The CaM100S-M13TT sample was prepared from stock solution introducing CaM100S 0.5 nmol, M13TT 0.6 nmol and Ca^{2+} 10 nmol in a total volume of 50 μL of MilliQ water.

Diluted TRIS buffer is present in the final sample to increase stability CaM100S and M13C stock aliquots. The lowering of the buffer concentration is essential to lower as much as possible the absorbance of the sample in the deep UV region.

The CaM100S-M13C CD spectra were acquired on a JASCO dual-beam spectrophotometer V-730ST, from 260 nm to 190 nm, while the CaM100S-M13TT one was acquired from 260 nm to 198 nm using a 0.2 mm cylindrical quartz cuvette (sample volume 40 μL), the temperature was thermostated at 25 °C. For both samples, 8 scans were accumulated, acquired using auto-response mode of maximum 4 seconds; the spectra were baseline corrected by recording the blank spectrum using the same cuvette.

9 EPR characterization

Pulsed EPR at Q-band is a technique sensitive to samples with concentrations as low as 10-50 μM and that works with very small volumes. For the cavities suitable for the Q-band, quartz tubes filled with approximately 10-15 μL of sample are used. Freeze-drying was implied in EPR sample preparation because it allows solvent substitution with deuterated one and sample concentration. Proteins involved in distance measurements are CaM single mutants labeled with SPIRO label trough SDSL and were already available from a previous thesis. Through the notation CaMxS we refer to a CaM whose AA in position x had been mutated to cysteine and bound to SPIRO label. A solution of CaM single mutant SPIRO labeled, M13 and Ca^{2+} (already stored in TRIS) with the proportion $n_{CaM}: n_{M13}: n_{Ca^{2+}} = 1.0: 1.2: 20$ was prepared in MilliQ water. The introduction of the Ca^{2+} ion allows the CaM to take on the *holo* form, thus making it able to complex the labeled peptide. This solution was then frozen in liquid nitrogen and freeze-dried overnight. The use of MilliQ water avoids introducing salts that will be difficult to redissolve once the sample is freeze-dried. The freeze-dried white powder is redissolved using a mixture of 60% deuterated glycerol and 40% deuterated water as a solvent. Typically, we always aimed to obtain final solutions between 70 and 90 μM in 15-20 μL of solution. The use of deuterated solvents is necessary to increase the T_2 relaxation times. This large a percentage of glycerol is used in experiments with laser irradiation to improve the optical quality of the frozen glassy matrix and as a cryoprotectant. However, samples must be prepared quickly and immediately frozen in liquid nitrogen because large amounts of glycerol have a denaturing effect on CaM. To prevent radical formation on the glass at 355 nm, Suprasil synthetic quartz tubes were used.

All pulsed experiments were conducted at Q-band (~ 34 GHz) on a Bruker Elexsys E580 with a EN 5107D2 Q-Band resonator in combination with a 3 W solid state amplifier and an Oxford Instruments CF900 cryostat. The laser photo excitation of the sample was provided by the third harmonic (355 nm) of a Nd-YAG pulsed laser (Quantel Brilliant) operated at a repetition rate of 10 Hz (5 ns pulses) and an average energy of ~7.3 mJ/shot. The sample was cooled down to 80 K, employing a liquid nitrogen flow controlled with an Oxford Instruments ITC503 temperature controller.

9.1 ED-EPR experimental setup

ED-EPR experiments were performed using the Hahn Echo sequence [π/2 - Δ - π - Δ - echo], each executed right after a laser pulse. To do this, the pulse sequences is triggered by the laser Q-switch. This way it's guaranteed enough triplet population at the beginning of each Hahn Echo sequence. The intensity of the Echo is reported for each B_0 value of interest. 220 to 250 points were acquired in the range between 1105 mT and 1325 mT. Experiments were performed with pulse length $t_{\pi/2}$ = 20 ns and t_{π}= 40 ns, and inter-pulse delay of $\Delta = 400$ ns. A 2-step phase cycle was applied to remove undesired the residual FID or cavity ringdown and receiver baseline offset. Measurement parameters for each sample are reported in **Table 1**.

ED-EPR spectra of the TT triplet state were always acquired after DEER experiments to prevent uncontrolled generation of TT radical.

Parameter	TT	M13TT	CaM6SM13TT	CaM100SM13TT	CaM114SM13TT
π/2 [ns]	20	20	20	20	20
π [ns]	40	40	40	40	40
τ_1 [ns]	400	400	400	400	400
τ_2 [ns]	3500	3500	3500	400	400
Integrator gate width t [ns]	160	160	220	160	140
SRT [µs]	2500	2500	2500	2500	2500
Averages per scan	100	20	50	100	100

Table 1: Pulse parameter for ED-EPR experiments for all the TT triplet spectra acquisition on Q-band Elexys E580.

All triplet spectra were analyzed through EasySpin[24] an open-source, free MatLab® toolbox specifically designed for the simulation and data analysis of EPR spectra.

9.2 DEER experimental setup

All the DEER experiments on NO•—TT•$^-$ distance were performed using the four-pulses DEER sequence: [π/2 (ν_A) - τ_1 - $\pi(\nu_A)$ - (τ_1 + t) - $\pi(\nu_B)$ - ($\tau_2 - t$) - $\pi(\nu_A)$ – echo] depicted in **Figure 18**. The pump pulse (ν_{B}) was applied to the TT•$^-$ maximum signal intensity while the probe pulse (ν_{A}) were applied to the NO• maximum signal intensity. The series of preliminary experiments conducted for all the samples under investigation before starting the DEER experiments is described as follows:

- Light-off echo-detected field-swept EPR, based on the Hahn Echo sequences [π/2 - Δ - π - Δ] for the detection of the SPIRO signal. The experiment was carried out with pulse length $t_{\pi/2}$ = 20 ns and t_{π}= 40 ns, and inter-pulse delay of 400 ns. The obtained spectrum is then used to setup the probe (ν_{A}) pulse.
- Laser illumination from 50 s up to 80 s was performed to ensure controlled TT•$^-$ formation followed by ED-EPR. Its signal intensity must both be sufficiently high to be seen but also not so much as to cancel the NO• signal.
- Transient nutation experiments were performed to assess the length of the pump pulse $\pi(\nu_{\mathrm{B}})$. The length was set as the length that achieved to the maximum inversion of the Hahn echo. The experiment is based on a three-pulse sequences: [π_{Nutation} - T - π/2 - τ - π - τ – echo]. The nutation pulse length was incremented starting from zero in 4 ns steps, and the position of the detection pulses and of the acquisition trigger was displaced using the same increment. The intensity of the echo was recorded versus the nutation pulse length, and the position of the first minimum of the nutation transient was taken as the $\pi(\nu_{\mathrm{B}})$ pulse length.

In addition to these preliminary experiments, the following points summarize the set-up parameters used for the DEER measurements of all samples:

- Deuterium ESEEM was suppressed using an 8-step nuclear modulation averaging cycle with an increment Δt of 16 ns (given by the inverse of the observed ESEEM frequency divided by the number of modulation-averaging steps[25]).
- 2-step phase cycle was applied to remove undesired echoes and receiver baseline offset.

Unwanted signals may originate from imperfections in pulse execution, instrumental dead time, or the presence of multiple coherence pathways. Phase cycling eliminates these issues by systematically varying the phases of the microwave pulses and combining the resulting signals in a way that selectively cancels out undesired echoes and offsets. This enhances the SNR and ensures that only the desired echo -typically the refocused or primary echo- is retained for accurate integration and analysis[26].

The sequence and its parameters were loaded and compiled using PulseSpel script, an extension that supports syntax highlighting for Bruker's EPR experiment scripting language. **Table 2** summarize the parameters used for each individual sample:

Parameter	CaM100CM13C	CaM6SM13TT	CaM100SM13TT	CaM114SM13TT
$t_{probe}\ (\pi/2)_A$ [ns]	24	24	24	24
$t_{probe}\ (\pi)_A$ [ns]	48	48	48	48
$t_{pump}\ (\pi)_B$ [ns]	48	48	48	48
τ_1 [ns]	200	200	200	200
τ_2 [ns]	3000	3200	3200	3300
Integrator gate width t [ns]	48	48	48	52
SRT [µs]	3500	3500	3500	3500
Averages per scan	400	40	100	72

Table 2: Pulse parameter for DEER experiments for all the NO• — TT•⁻ distance measurement on Q-band Elexys E580.

All DEER traces were then processed using *DeerAnalysis2022*[27], the most used software package by EPR community to analyze dipolar EPR data. The program runs in the MatLab® environment and works through a graphical user interface (GUI); it provides post-processing of the obtained time domain spectra.

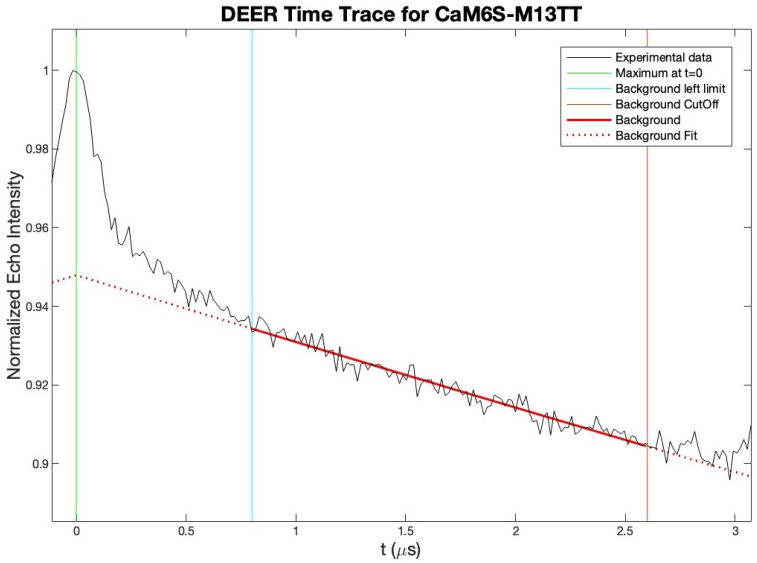

Figure 32: DEER Time Trace for CaM6S-M13TT loaded in DeerAnalysis after automatic phase correction. Signal at t=0 is identified by the green line, while the Background correction limits are identified by the blue and orange line. Background is reported as a red line while its fit as a dotted red line.

Time traces were loaded into the program (**Figure 32**), and phase correction was automatically done. t_0 was set to the maximum of the time trace and traces were truncated if an artifact at long dipolar evolution time was observed. To analyze DEER data, DeerNet, a neural network that analyzes background and distance distribution simultaneously, was used. Its GUI is reported in **Figure 33**.

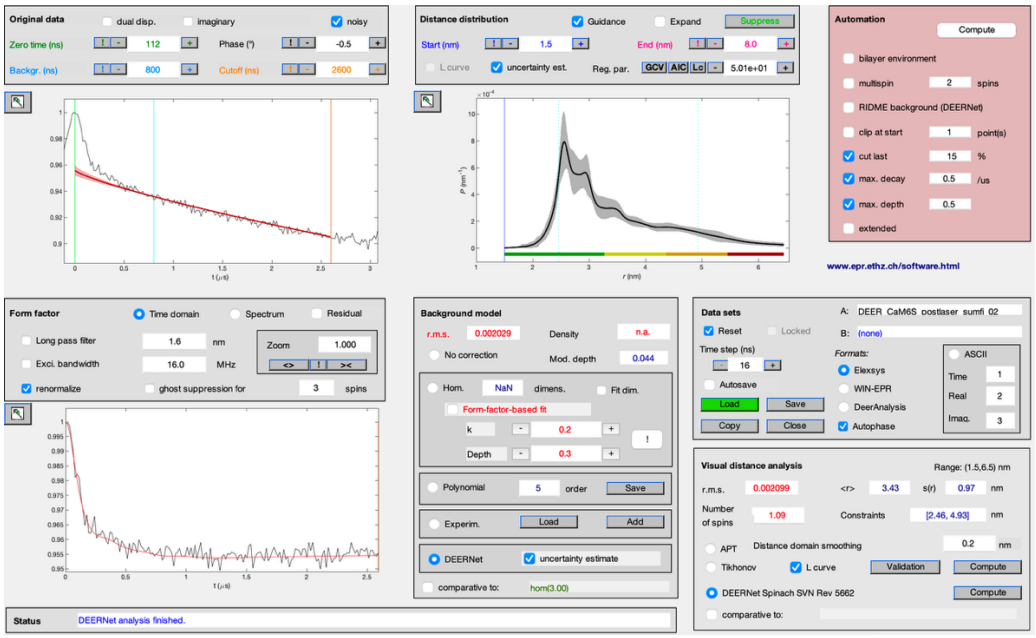

Figure 33: Graphical user interface for DeerAnalysis 2022.

9.3 ReLaser-IMD experimental setup

Refocused Laser Induced Magnetic Dipole experiments to measure NO•−T_1TT distance were performed using the following sequence: [$\pi/2$ - t_1 - π - (t_1 + t_2 - t) - laser - (t) - π – echo] depicted in **Figure 19**. The laser flash is kept fixed in time while the microwave pulses are moved forward in time. To obtain this, the pulse sequences is triggered by the laser flashlamp, in **Figure 34** there is a schematic representation for the wiring set-up of the ReLaser-IMD experiment.

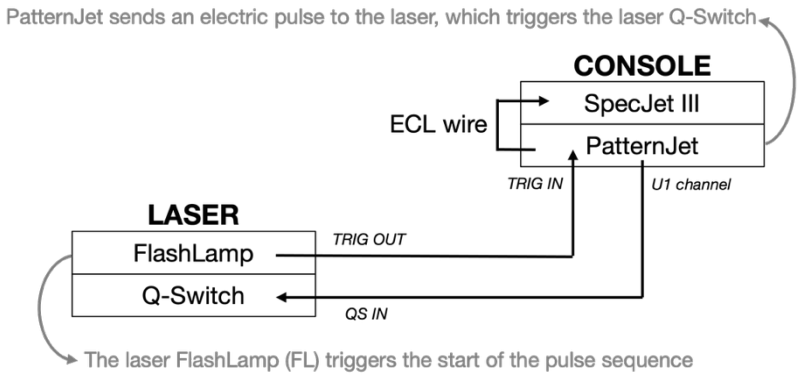

Figure 34: Schematic representation for the wiring configuration of the ReLaser-IMD experiment.

Before starting the ReLaser-IMD experiments, Time Resolved EPR (TR-EPR) experiments was performed to maximize the laser signal in cavity. The measured quantity is the temporal development of transient magnetization. To record TR-EPR spectra the signal coming from the detector (diode) was digitized using the SpecJet unit triggered by the laser flash. The

microwave cavity was critically coupled, and no modulation of the magnetic field was applied. This preliminary experiment was conducted for all the samples under investigation.

Since the DEER and ReLaser-IMD experiments require different resonator coupling conditions, the pulse lengths used for DEER measurements were not directly transferred to the ReLaser-IMD experiments. In DEER, the cavity was partially decoupled to increase the excitation bandwidth required for the two-frequency experiment. In contrast, ReLaser-IMD is a single-frequency experiment; therefore, the cavity was critically coupled to maximize the microwave field strength. Under these conditions, the pulse lengths were recalibrated before performing the ReLaser-IMD measurements.

In addition, a 4-step phase cycle was applied to selectively enhance the desired echo signal while suppressing unwanted ones.

The sequence and its parameters were loaded and compiled using PulseSpel script. **Table 3** summarize the parameters used for each individual sample:

Parameter	CaM6SM13TT	CaM100SM13TT	CaM114SM13TT
$\pi/2$ [ns]	20	20	20
π [ns]	40	40	40
τ_1 [ns]	200	200	200
τ_2 [ns]	2500	2500	2500
Integrator gate width t [ns]	40	40	40
SRT [µs]	10000	10000	10000
Averages per scan	20	20	20

Table 3: Pulse parameter for ReLaser-IMD experiments for all the NO•-T_1TT distance measurement on Q-band Elexys E580.

All the ReLaser-IMD traces were then processed using DeerAnalysis2022[27]. Data were analyzed through baseline subtraction, 3D-homogenous fitting of the time traces and Tikhonov regularization. The latter was applied to define the optimum compromise between goodness of the fitting and smoothness of the distance distribution.

10 Computational tools

10.1 UCSF ChimeraX

ChimeraX allows interactively viewing very large data sets and analyzing different types of data together, focusing on protein and molecular structures. ChimeraX reads over 60 file formats, many for volume data, with the remainder for atomic structures, sequences, 3D objects, scripts or code, and composites of multiple data types such as ChimeraX session files and integrative hybrid models. ChimeraX also provides advanced graphics and lighting modes and is often used to make high-quality figures and movies for publication.[28]

When an atomic structure is opened, it is displayed in a style designed to be the most informative given the structure's size. A small molecule is displayed as “sticks” colored by element type. The main ChimeraX analysis features used in this thesis are:

- Measure atomic distances and torsion angles

- Find clashes or contacts between sets of atoms
- Color surfaces by lipophilicity or (externally computed) electrostatic potential

ChimeraX is available for Windows, Mac, and Linux operating systems (http://www.rbvi.ucsf.edu/chimerax/) and is open source and free for non-commercial use.[29]

10.2 AlphaFold

AlphaFold (now in its 3.0 version) is a tool for predicting protein folding starting from its primary amino-acid sequence using artificial intelligence. AlphaFold structure prediction can produce starting protein models, albeit not always as accurate as from experiments, but suitable for subsequent refinement. ChimeraX has tools to run new AlphaFold predictions, find existing predictions in the EBI AlphaFold Database, and plot error metrics for evaluating model quality.[30] The three CaM mutants' structures (CaM E6C, CaM I100C and CaM E114C) in complex with M13C and labeled with the SPIRO label were already available from a previous thesis (work by Diletta Testoni and Daniela Centanni). Proteins structures were prepared with AlphaFold 3 in the *holo* form, complexing the M13C alpha-helix peptide; starting from the AlphaFold structures, the SPIRO labels were modeled and attached to the proteins using a combination of Avogadro (see below) and ChimeraX and then refined with molecular dynamics.

10.3 Avogadro

The Avogadro project is an advanced molecule editor and visualizer designed for cross-platform use in computational chemistry, molecular modeling, bioinformatics, materials science, and related areas. It offers flexible, high-quality rendering, and a powerful plugin architecture. Typical uses include building molecular structures, formatting input files, and analyzing output of a wide variety of computational chemistry packages.[31]

Avogadro's tools were used in a previous thesis to simulate the SPIRO spin label molecular structure before implementing it in the CaM molecular model. In this thesis, TTAI structure was generated through Avogadro and imported to ChimeraX. The TT spin label was then bound to the M13C cysteine residue using ChimeraX tools.

The protein models produced combining ChimeraX and Avogadro's features were used to interpret DEER and ReLaser-IMD distribution distances and are reported in **Figure 70**, **Figure 71** and **Figure 72**.

Experimental results

11 Peptide labeling

Optimization of the labeling conditions required numerous experimental attempts due to the limited solubility of the TTAI label and the limited compatibility of the probe with aqueous systems. TTAI is a difficult molecule to solubilize, an extremely limiting characteristic for labeling reactions. As discussed in the labeling protocols above, the label should be in a high molar excess to drive the labeling reaction, and the solvent mixture must be compatible with a protein or peptide.

TTAI is a difficult to dissolve and amphiphilic molecule. It can be broken down into three regions. The first, consisting of two thiophene rings, is expected to be soluble in toluene, THF or DCM. These are aprotic solvents that are good for solubilizing weakly polar molecules. Proceeding towards imidazole, the second part is constituted of acetylthiophene, while the third is made up of methylimidazole. These are two parts with similar solubility characteristics, soluble in aprotic polar solvents, such as DMSO, acetonitrile and DMF. TTAI therefore has a marked amphiphilic character, with a relatively hydrophobic thiophene portion and a more polar acetyl-imidazole region, as schematized in **Figure 35**. Several solvent mixtures were explored starting form computational solubility prediction tools;[32] however, none of the conditions experimentally tested proved to be satisfactory. Only DMSO was satisfactory.

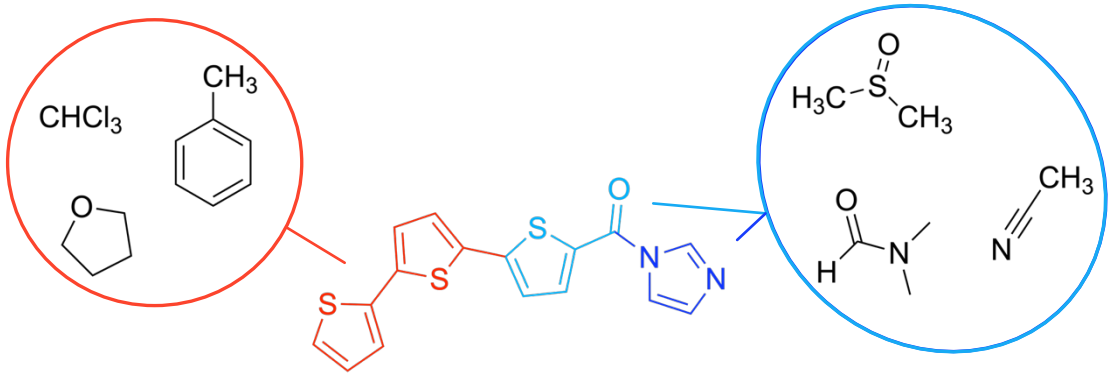

Figure 35: Schematic subdivision of the TTAI into regions characterized by different solubility properties. In red the dithiophene portion, soluble in aprotic organic solvents with low polarity; in blue the acetylthiophene group and in blue the methylimidazole group, more compatible with aprotic polar solvents.

The M13C peptide and CaM are both soluble in water. Since TTAI is highly insoluble in water and performing the reaction in pure DMSO would result in significant purification problems, and in the case of proteins in denaturation, the 25% DMSO mixture in water has been identified as the best solvent for labeling M13C. Note that this DMSO concentration is too high for a protein, where a 10 vol% is normally considered the safe upper limit, but is fine for a peptide. In 25 vol% DMSO the formation of TTAI in suspension was observed, as expected, but even in heterogeneous phase a labeling reaction can proceed.

Owing to the limited solubility of TTAI, increasing the molar excess of the label is not straightforward. We settled on a molar probe excess equal to 12 times that of the peptide. While this is only a nominal molar excess, since the reactions are performed in heterogeneous phase, these conditions increase the contact surface between the solid phase and the reaction medium, favoring the probe transfer into solution and improving the overall labeling performance.

The reaction time had also been optimized. After 1, 4 and 10 hours, no significant formation of labeled peptide was observed, so the reaction mixture was left under agitation for 20 hours. Longer reaction times did not significantly improve the yield, suggesting that the detachment of the probe becomes competitive.

The reaction formally proceeds through the nucleophilic attack of the thiolate ion of the cysteine on the carbonyl carbon of the probe, therefore, to thermodynamically drive the reaction, the formation of a cysteinate anion on the peptide at basic pH was chosen to improve the yield. At the same time the pH should not be too high that the amine side groups and the OH^- itself become competitive with the thiolate, see **Figure 36** below. A TRIS buffer was prepared at pH = 8.3 favoring the reactivity of the cysteine residue with respect to other nucleophiles present in the reaction mixture. Indeed, although the basic hydrolysis reaction of thioesters is favored above pH=6.5, an increase in reaction yield at pH = 8.3 was observed compared to attempts performed at pH=7. However, since the label might become detached from the peptide if left at pH>7 for long periods, such as those employed in the following steps, it is important to neutralize the solution after the reaction.

Following the labeling, the excess undissolved probe was removed through several centrifugations. was recovered and redissolved in DMSO. The hypothesis is that the precipitated probe is the unreacted probe, therefore reusable for another labeling reaction. Then, before the purification most of the DMSO was removed by evaporation under nitrogen flow and dissolved for chromatographic purification.

Overall, this labeling protocol resulted in a 40% labeling efficiency, the limiting factor being the solubility of TTAI, in tandem with the imidazole being an inefficient leaving group for this reaction.

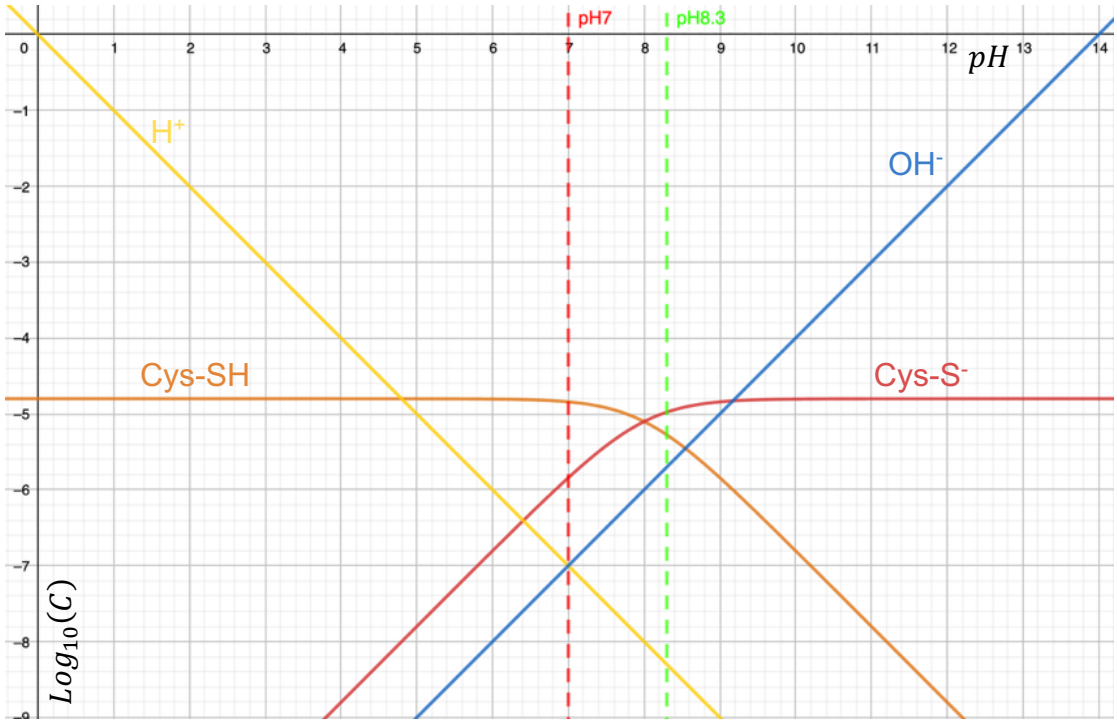

Figure 36: Cys protonate species logarithmic diagram calculated for a total peptide concentration of 62.5 μM. The vertical lines indicate pH 7.0 (red) and pH 8.3 (green), respectively.

12 Purification

Early purification attempts were made trying to extract the unreacted probe from the aqueous environment in organic solvents. These proved unsuccessful since we observed the concurrent extraction of the peptide in the organic phase and incomplete extraction of the free TTAI from the aqueous one. From the study of the samples prepared using the labeled peptide obtained with the first inefficient purification procedures, weak DEER and no ReLaser-IMD signals were observed. Only after the implementation of the RPC as a purification protocol, it was possible to increase DEER signal intensity and to measure ReLaser-IMD time traces. As the first samples were prepared using a mixing of labeled and unlabeled peptide, not all the protein-peptide complexes contained the spin probe couple. Therefore, SNR is insufficient for reliable distance distribution determination.

Therefore, we moved to a chromatographic purification protocol using reverse phase chromatography (RPC). To successfully perform the RPC chromatography of a peptide it is often necessary to introduce a coupling agent, such as trifluoracetic acid (TFA). A peptide is a hydrophilic species, so it tends to interact more with the mobile phase rather than with the stationary phase and thus exit in the flow-through. In our case, the labeled and unlabeled peptides are similarly hydrophilic and without the coupling agent they would be indistinguishable. The coupling agent is an acid strong enough to protonate all the basic AAs of the peptide as well as to form an ion-pair with each negative charge on it. The trifluoroacetate anion interacts with the positive charges of the peptide, neutralizing them. This way the peptide will be neutral (null charge) and therefore sufficiently apolar to be retained by the stationary phase. Just using a coupling agent it's possible to distinguish a labeled peptide from a non-labeled one.

12.1 Two step purification and label stability

A previously developed elution protocol was used to purify the peptide. Knowing that the presence of high amounts of DMSO in the sample causes a marked broadening of the chromatographic peaks and given the uncertainty regarding the stability of the labeled peptide in an acidic environment, several elution tests were performed.

As a first test, the possibility of purifying the raw reaction from the excess probe and traces of DMSO was verified; in this case the first run was done purposefully without TFA to fully remove the unreacted probe; the chromatogram is reported in **Figure 37**.

The elution protocol used was devised with an isocratic of 0% eluent B', followed by a rapid gradient of up to 90% of B'. In the absence of a coupling agent, the mixture of M13TT and M13C was eluted in the flow-through together with salts in the initial isocratic step. From the UV-Vis analysis it was evident that the fraction that came out at 2.5 mL was the peptide mixture, while the UV-Vis spectrum of the fraction at 11 mL suggested it to be the unreacted TT.

The fraction at 2.5 mL was collected, divided into two aliquots and freeze-dried. In the end, $6.8 \cdot 10^{-9} mol$ of peptide mixture were isolated in total.

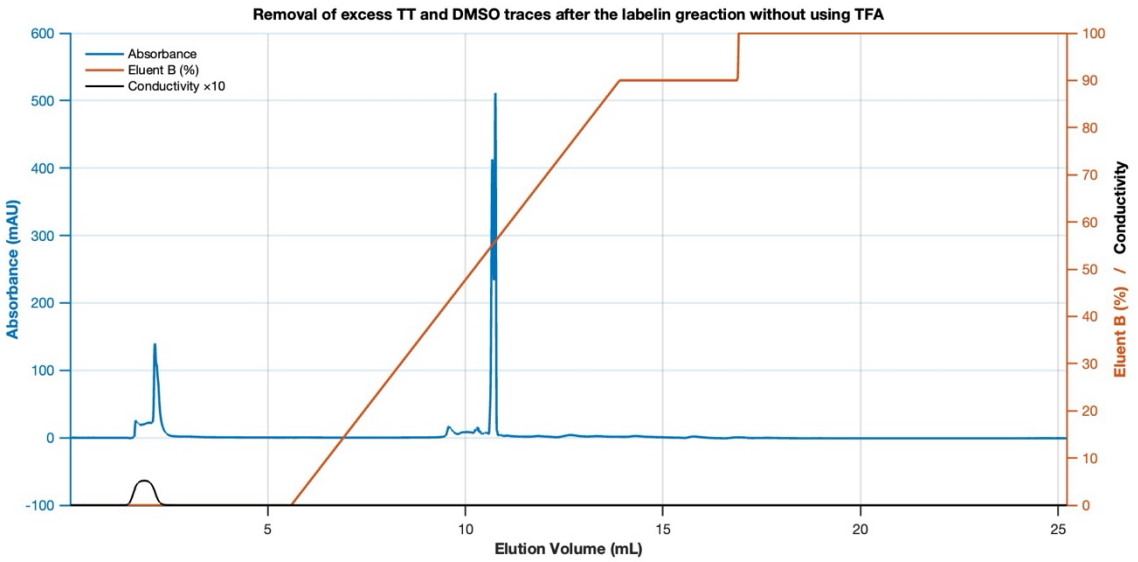

Figure 37: Chromatography of the peptide mixture M13C and M13TT (light blue), obtained by FPLC analysis (ÄKTA™ pure 150 system; UV monitor U9-L; fraction collector F9-C; S9H pumps for system and sample; Cytiva RESOURCE™ RPC column). The run was performed at 1mL/min using eluent A' (MilliQ water) and eluent B' (90% acetonitrile). It was possible to purify the peptide mixture from the excess probe.

The next step is the separation of the labeled peptide from the unlabeled one through RPC making use of TFA as a coupling agent.

For subsequent purifications, an elution protocol previously developed for the purification of labeled peptide in the presence of TFA was used. This is a protocol that was devised during the purification phase during the study of other probes for the M13C peptide. To determine the output fraction of the unlabeled peptide, a chromatographic run was performed with M13C 60 μM; reported in **Figure 38**. The peak absorption at 280 nm is observed at around 13 mL and is indicative of the peptide output. The small spike at 13.9 mL is potentially attributable to different protonation states.

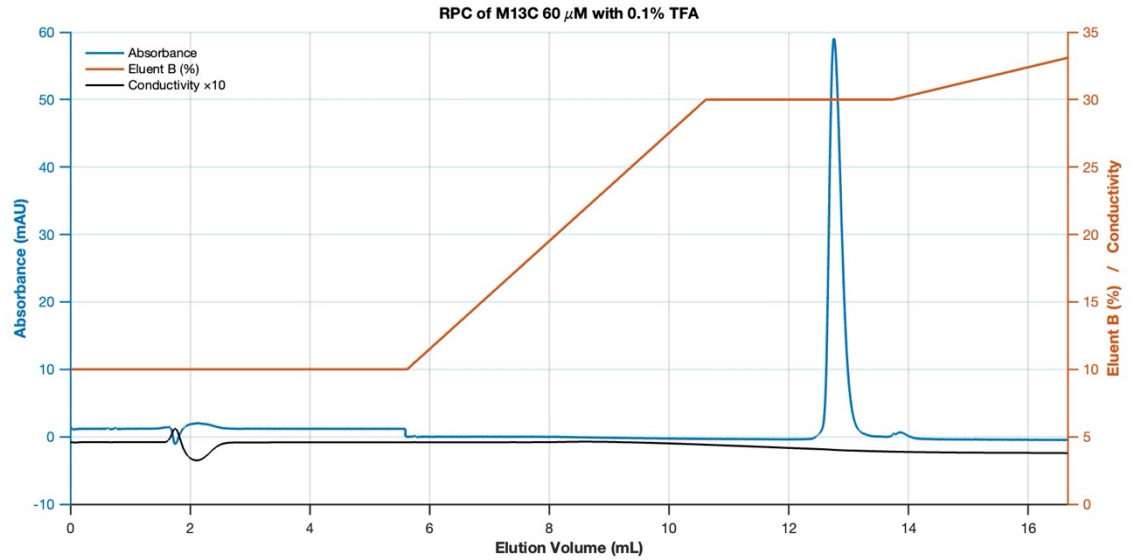

Figure 38: Chromatography of M13C peptide (light blue), obtained by FPLC analysis and RPC column. The run was performed at 1mL/min using eluent A (MilliQ water + 0.1% TFA) and eluent B (90% acetonitrile + 0.1% TFA).

Before attempting the separation in TFA, since thioesters are subject to nucleophilic attack on carbonyl carbon and the acid hydrolysis reaction is favored at pH<4, it was necessary to perform hydrolysis kinetics to verify the stability of the labeled peptide in the presence of

TFA. Half of the lyophilized peptide mixture (see above) was used to prepare the sample used to perform hydrolysis kinetics. A 0.1 vol% solution of TFA in a solution of 25 vol% of DMSO in MilliQ water. Resulting in pH≃2. Hydrolysis kinetics were followed by UV-Vis (described below in **13.7**) and showed that the labeled peptide remains stable in the presence of TFA over timescales significantly higher than the one required for chromatographic separation.

Since the addition of TFA did not result in marked removal of TT from the labeled peptide, at the end of the kinetics the sample was injected into the column. This way, it was also possible to verify the influence on the quality of chromatography due to the presence of DMSO at 25% in the sample. The chromatogram is reported in **Figure 39**.

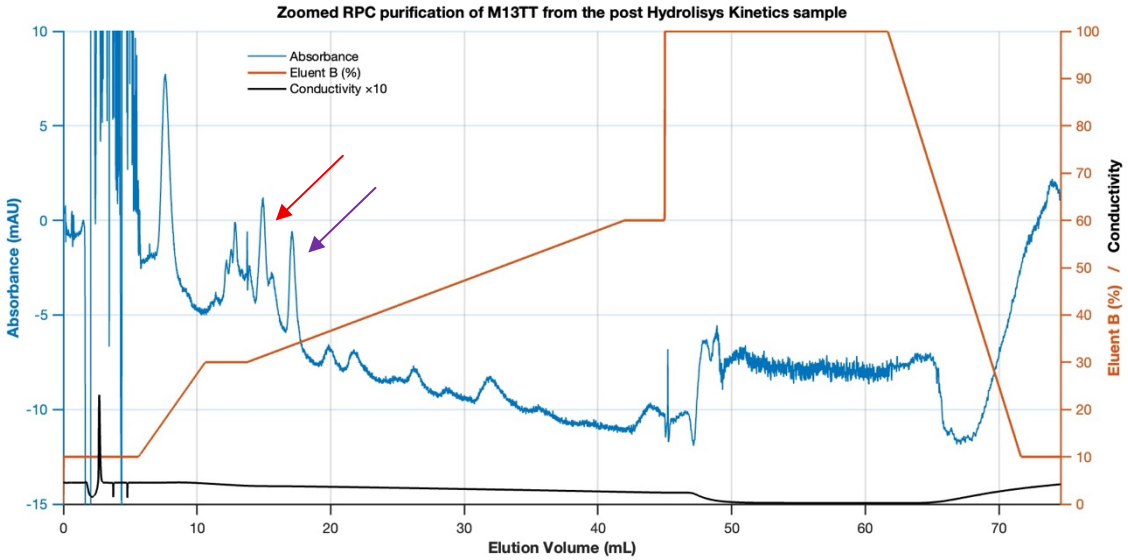

Figure 39: Chromatography of the M13C and M13TT sample (light blue) at 25% DMSO previously used for the hydrolysis kinetics in TFA, obtained by FPLC analysis and RPC column. The run was performed at 1mL/min using eluent A (MilliQ water + 0.1% TFA) and eluent B (90% acetonitrile + 0.1% TFA). It was possible to separate the labeled peptide from the unlabeled peptide while no serious effects due to DMSO occurred.

The other half of the freeze-dried peptide stock was dissolved in 600 μL of MilliQ water and injected into the column. The chromatogram is reported in **Figure 40**.

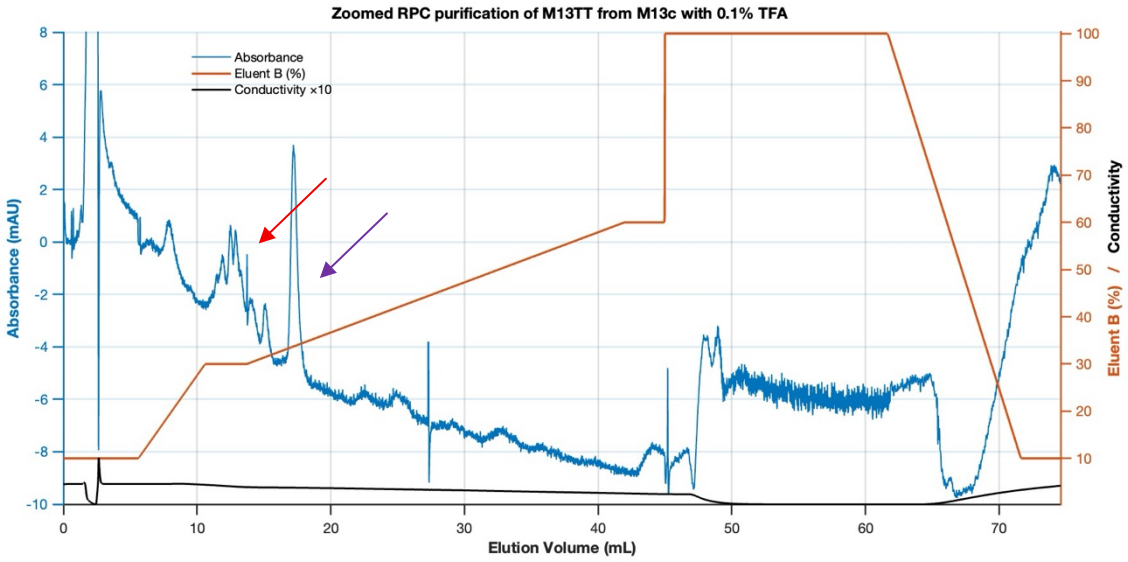

Figure 40: Chromatography of the M13C and M13TT sample (blue) in MilliQ water, obtained by FPLC analysis and RPC column. The run was performed at 1mL/min using eluent A (MilliQ water + 0.1% TFA) and eluent B (90% acetonitrile + 0.1% TFA). It was possible to separate the labeled peptide from the unlabeled one.

The low concentration of the peptide causes both chromatograms to be fairly noisy and exposed to marked baseline drift. They are shown without any corrections, since the evaluation of the reaction has been performed purely using UV-Vis spectroscopy.

For both runs, the elution of the unlabeled peptide is observed at 30% of eluent B in the form of a set of peaks. Despite the change in shape of the peak compared to that observed in the reference chromatography for M13C (**Figure 38**), the elution volume coincides (red arrow in **Figure 39** and **41**). The presence of a group of peaks is compatible with different protonation states of the peptide. On the other hand, the labeled peptide elutes during the linear gradient and around 33% of eluent B (purple arrows). Although the two samples were prepared at the same total concentration of peptide, in the one used for hydrolysis kinetics (**Figure 39**) a decrease in the intensity of the labeled peptide absorption peak is observed. Surely it is a consequence of the hydrolysis kinetics experiment previously performed that decreased the concentration of labeled peptide in the sample.

Since this procedure was successful in the separation of the labeled from the unlabeled peptide, it was repeated a few times with varying amounts of peptide and TTAI. However, the overall yield for the labeling and purification is only about 5%.

12.2 One-step purification

Subsequently, to limit peptide loss, an attempt was made to remove, in a single run, the excess TT, the traces of DMSO, and to separate the labeled peptide from the unlabeled one. A labeling reaction was performed with greater amounts of both peptide and probe exhausting in this attempt all TTAI stock aliquots. The chromatogram is reported in **Figure 41**.

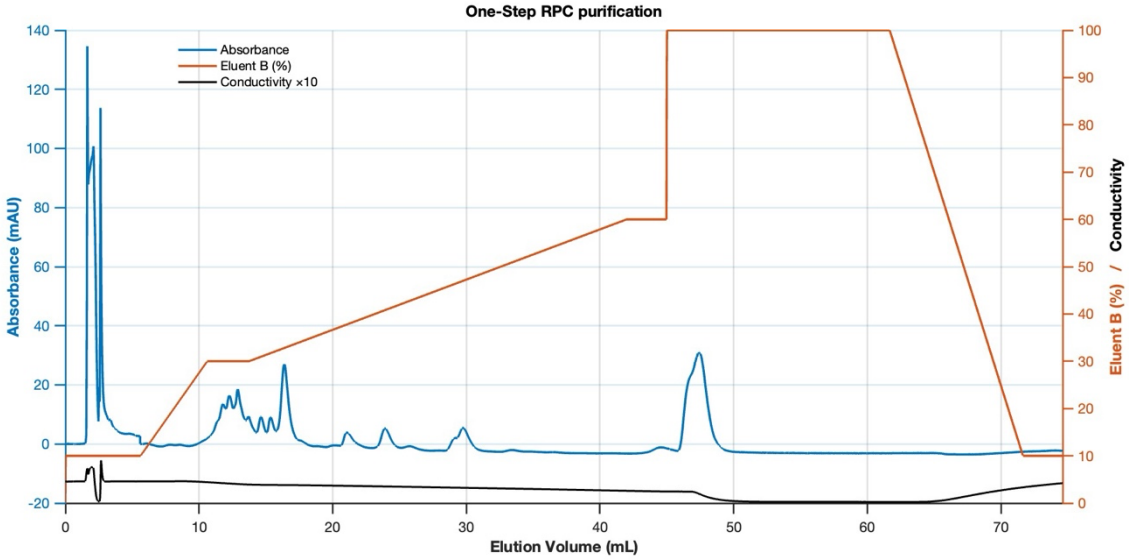

Figure 41: Chromatography of the post-evaporation and centrifugation labeling reaction solution (light blue), obtained by FPLC analysis and RPC column. The run was performed at 1mL/min using eluent A (MilliQ water + 0.1% TFA) and eluent B (90% acetonitrile + 0.1% TFA). It was possible to separate the labeled peptide from the unlabeled one, as well as to remove the excess label and DMSO traces.

Compared to the runs showed in the previous paragraph, the increase in absorbance is the result of the increase in the peptide injected into the column concentration. The improved quality of the run also allowed the free TT output to be seen at around 48 mL. All spikes between 20 and 30 mL are due to various terthiophene byproducts of the labeling reaction.

Comparing the region between 10 mL and 20 mL of the four performed chromatograms (see **Figure 42**), an actual broadening of the peaks caused by DMSO is observed. In addition, the sample preparation conditions also influence the position and intensity of the peaks. Since there are no major variations between chromatographic runs, and the labeled peptide is well-separated from the rest (purple arrows) performing a single chromatographic run for peptide purification and separation is cost-effective.

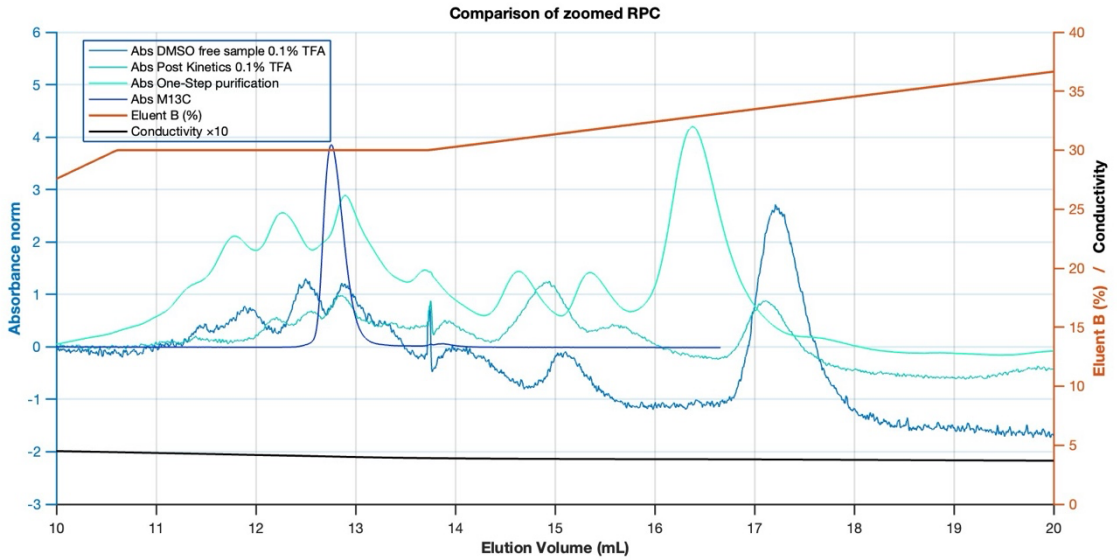

Figure 42: Comparison of chromatographic runs over the peptide output range. The results are reproducible and the output volume of the peptide in the reference run coincides with that obtained in the purification runs.

12.3 Single gradient protocol

Trying to improve the resolution of the column, it was decided to simplify the elution protocol, replacing it with an initial isocratic at 0% of eluent B, followed by a slow gradient of up to 60% of eluent B. The removal of the isocratic to 30% of eluent B allows to tighten the peak of the unlabeled peptide. The initial isocratic at 0% eluent B allows a better removal of salts and excess DMSO than a 10% eluent B. For the longevity of certain chromatographic columns, it is not recommended to practice 100% elutions of one of the two eluents. However, in the case of the pre-packed Cytiva RESOURCE™ 15RPC ST 4.6/100 column, these weaknesses are not present.

Before testing the efficiency of the protocol on the raw reaction, a reference run was performed on a 92 μM sample of M13C, see **Figure 43**.

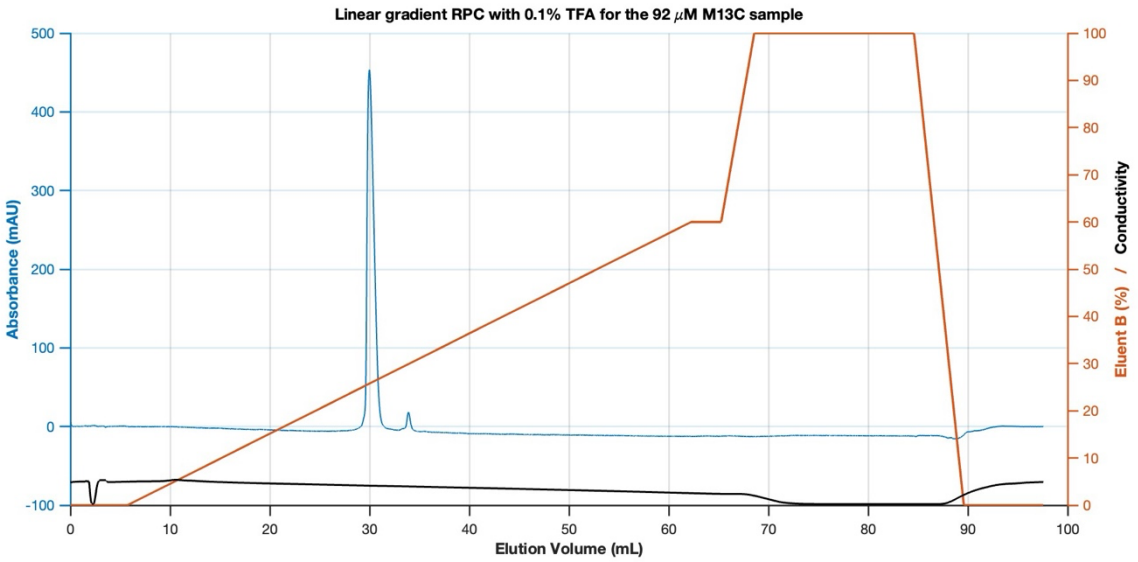

Figure 43: Chromatography of M13C peptide (blue) in MilliQ water, obtained by FPLC analysis and RPC column. The run was performed at 1mL/min using eluent A (MilliQ water + 0.1% TFA) and eluent B (90% acetonitrile + 0.1% TFA). For the single linear gradient elution protocol, the peptide comes out at 30mL.

Unlabeled peptide output is observed around 30 mL, in the presence of a small peak at 34 mL potentially attributable to a different protonation state of the peptide.

For the preparation of the sample used to test the efficiency of the new elution protocol, a labeling reaction at pH=8 was performed using the TTAI probe recovered from previous labeling. To reduce the hydrolysis of the labeled peptide as much as possible, the reaction mixture was neutralized both before it was evaporated and immediately after the fraction left the column. The chromatogram is reported in **Figure 44**.

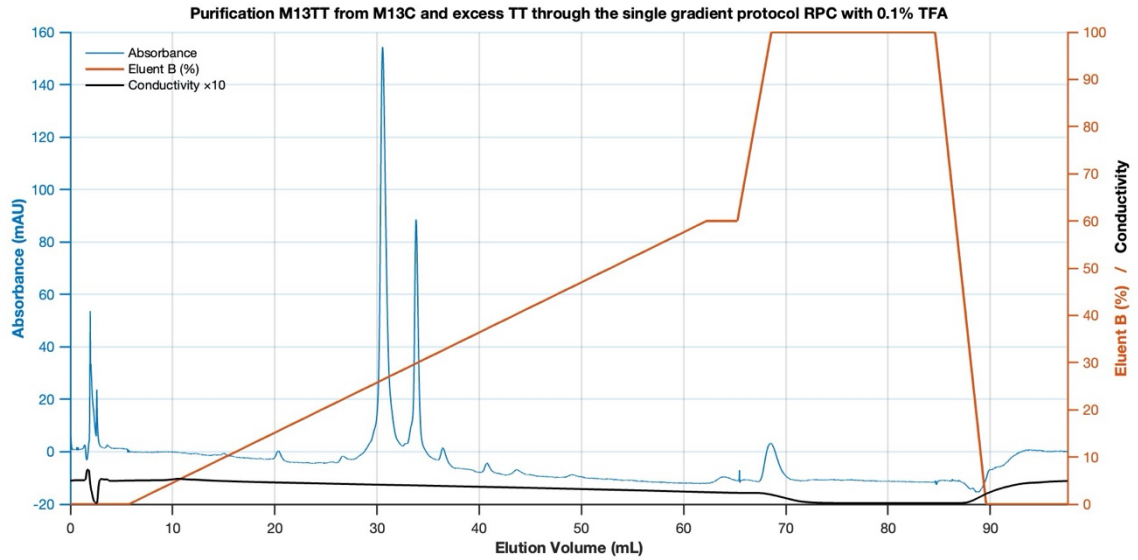

Figure 44: Chromatography of the post-centrifugation labeling reaction solution (light blue), obtained by FPLC analysis and RPC column. The run was performed at 1mL/min using eluent A (MilliQ water + 0.1% TFA) and eluent B (90% acetonitrile + 0.1% TFA). From the UV-Vis analysis it was not possible to demonstrate the presence of bonded label.

Although the chromatographic run suggests that the labeled peptide elutes at 34 mL, from the UV-Vis analysis of the fractions between 28 and 38 mL, negligible or zero TT is observed. The peaks at 31 and 34 mL are attributable to the unlabeled peptide, while the peak at 68 mL is attributable to the free probe.

The null labeling efficiency suggests that the TTAI recovered from the labeling reactions is not reusable. The impossibility of effectively recovering the probe, combined with its poor solubility, represents a significant limitation both in economic terms and in terms of experimental sustainability.

13 Characterization

After isolating the fraction containing the labeled peptide, its concentration was determined by applying the Lambert-Beer law:

$$A = \varepsilon \cdot d \cdot C \tag{34}$$

Where A is the absorbance, ε are the molar extinction coefficient, d the optical path and C the chromophore concentration.

The labeled peptide, M13TT, has an absorption band at 280 nm attributable to the tryptophan residue present in the peptide sequence. The TT chromophore shows a maximum absorption at 376 nm when free in solution, which shifts to about 344 nm following binding to the cysteine residue of the peptide. Since TT also contributes significantly to absorption at 280 nm, the labeled peptide concentration cannot be derived directly from the absorbance measured at this wavelength:

$$A^{280} = (\varepsilon_{Trp}^{280} + \varepsilon_{TT}^{280}) \cdot d \cdot C \tag{35}$$

Since it was not possible to experimentally determine the molar extinction coefficient of the TT bound to the peptide, it was assumed that it coincided with that measured for free TT in solution containing 75% H_2O and 25% DMSO. The TT concentration was then derived from absorbance at 376 nm and used to estimate its contribution to absorption at 280 nm. By exploiting the additivity of absorbances, it was possible to isolate the contribution of tryptophan and determine its concentration:

$$C_{TT} = \frac{A_{TT}^{376}}{\varepsilon_{TT}^{376}} \tag{36}$$

$$\varepsilon_{TT}^{280} = \frac{C_{TT}}{A_{TT}^{280}} \tag{37}$$

In the ideal case of a fully labeled and purified peptide, the independently determined concentrations for TT and tryptophan should be the same. Any differences are mainly attributable to the uncertainties associated with the molar extinction coefficients used in the calculations.

To determine the molar extinction coefficients necessary for subsequent processing, the following calibration lines have been constructed.

13.1 Determination of ε_{Trp}^{280} in a 75% H_2O and 25% DMSO solution

The solutions shown in **Table 4** were prepared and the UV-Vis spectra were measured in the range 250-600 nm and reported in **Figure 45**.

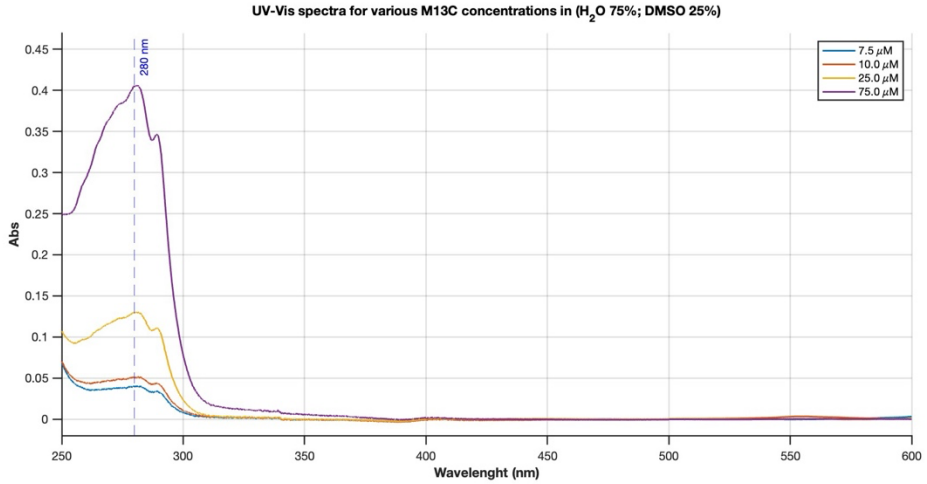

Figure 45: UV-Vis spectra for M13C 75% H_2O and 25% DMSO solutions at various concentrations, acquired to build the calibration line to determine ε_{Trp}^{280}.

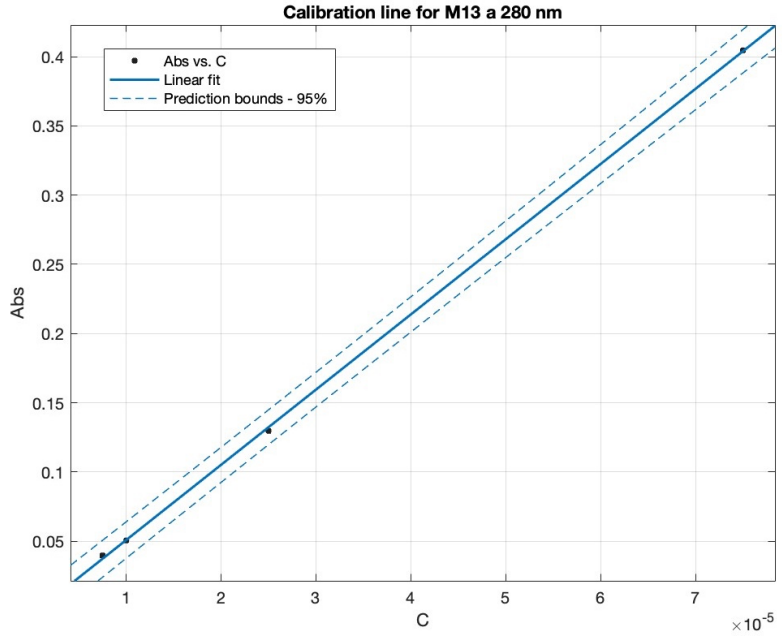

Figure 46: Calibration line to determine ε_{Trp}^{280} in 75% H_2O and 25% DMSO solution. Esteemed $r^2 = 0.9998$.

$C_{M13c} = C_{Trp}\ [\mu M]$	A_{Trp}^{280}
7.5	0.039
10.0	0.050
25.0	0.129
75.0	0.405

Table 4: Concentration for the M13C 75% H_2O and 25% DMSO solutions with the respective absorbance at 280 nm.

The absorbance values at 280 nm were subjected to linear regression as a function of peptide concentration (**Figure 46**). According to the Lambert-Beer law, the slope of the line corresponds to the molar extinction coefficient of tryptophan.

From the linear fit it was obtained that: $\varepsilon_{Trp}^{280} = 5400 \pm 210\ M^{-1}cm^{-1}$.

13.2 Determination of ε_{TT}^{280} and ε_{TT}^{376} in a H_2O:DMSO = 3:1 solution

The solutions shown in **Table 5** were prepared and the UV-Vis spectra were measured in the range 250-600 nm and reported in **Figure 47**.

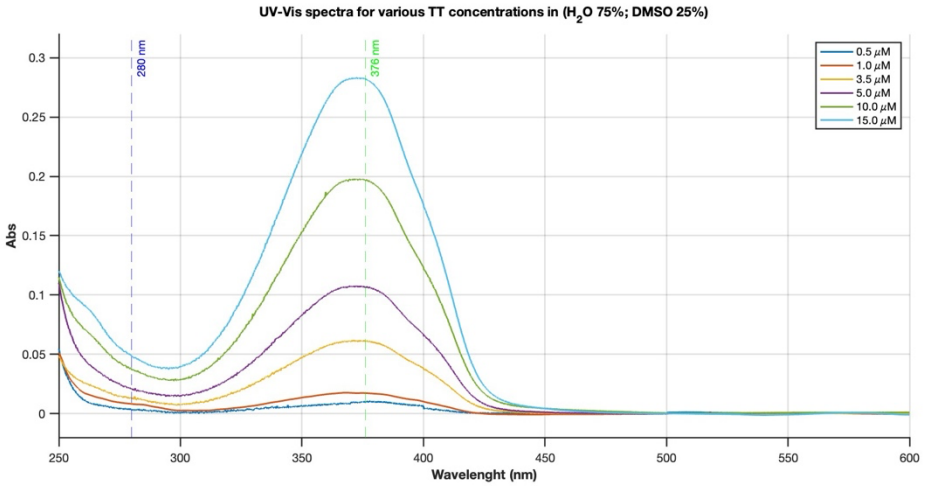

Figure 47: UV-Vis spectra for TTAI 75% H_2O and 25% DMSO solutions at various concentrations, acquired to build the calibration line to determine ε_{TT}^{280} and ε_{TT}^{376}.

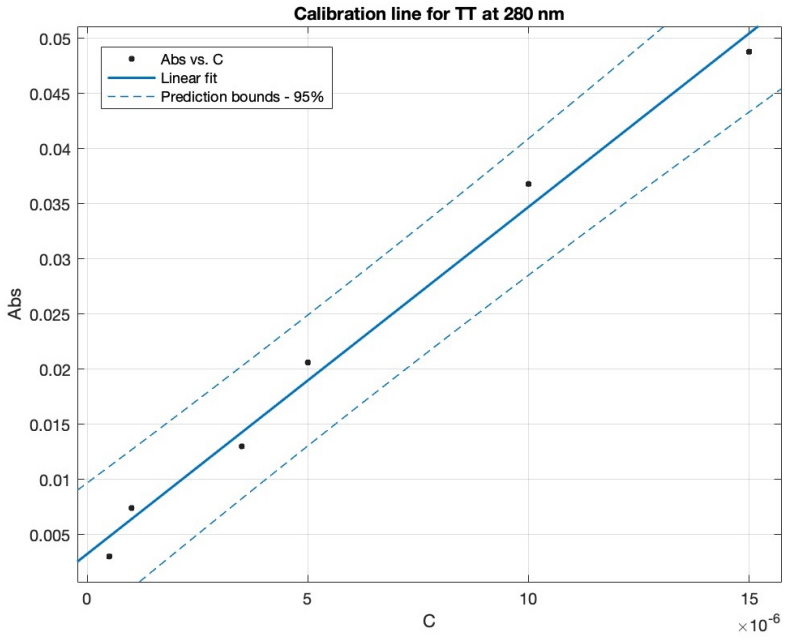

Figure 48: Calibration line to determine ε_{TT}^{280} in 75% H_2O and 25% DMSO solution. Esteemed $r^2 = 0.9888$

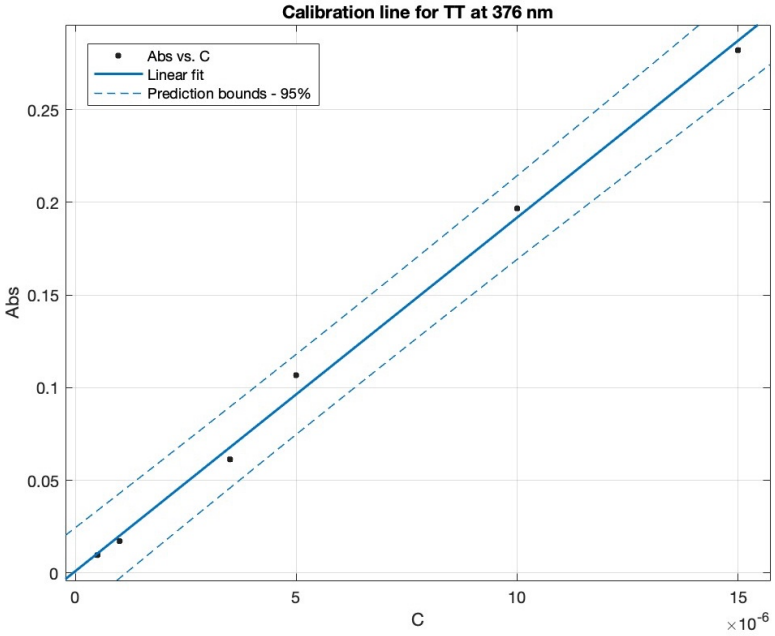

Figure 49: Calibration line to determine ε_{TT}^{376} in 75% H_2O and 25% DMSO solution. Esteemed $r^2 = 0.9964$

$C_{TT}\ [\mu M]$	A_{TT}^{280}	A_{TT}^{376}
0.5	0.003	0.010
1.0	0.007	0.017
3.5	0.013	0.061
5.0	0.021	0.107
10.0	0.037	0.197
15.0	0.049	0.282

Table 5: Concentration for the TTAI 75% H_2O and 25% DMSO solutions with the respective absorbance at 280 nm and 367 nm.

The absorbance values measured at 280 nm and 376 nm were subjected to linear regression as a function of TTAI concentration (**Figure 48** and **Figure** 49). The following molar extinction coefficients were obtained from the slopes of the calibration lines: $\varepsilon_{TT\ 25\%DMSO}^{280} = 3100 \pm 440\ M^{-1}cm^{-1}$ e $\varepsilon_{TT\ 25\%DMSO}^{376} = 19000 \pm 1600\ M^{-1}cm^{-1}$.

13.3 Determination of ε_{TT}^{280} and ε_{TT}^{376} in a H_2O:DMSO = 1:1 solution

The solutions shown in the **Table 6** have been prepared and the UV-Vis spectra have been measured in the range 260-480 nm and reported in **Figure 50**.

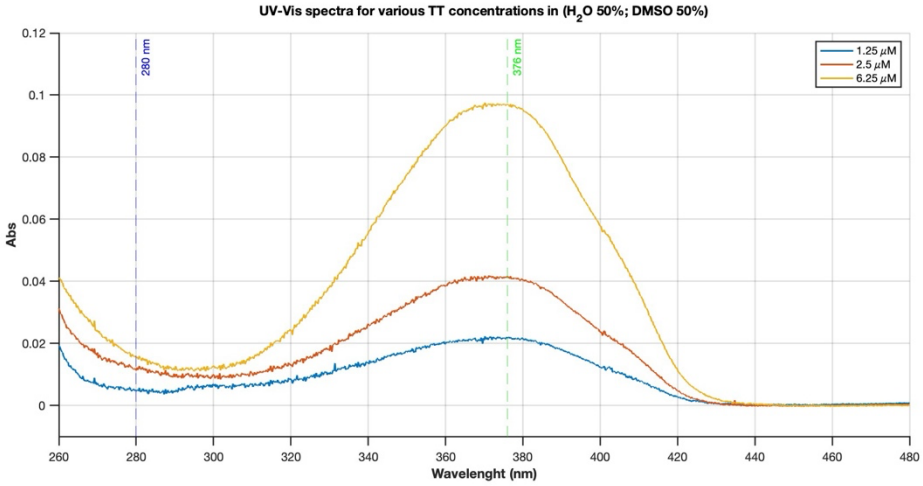

Figure 50: UV-Vis spectra for TTAI 50% H_2O and 50% DMSO solutions at various concentrations, acquired to build the calibration line to determine ε_{TT}^{280} and ε_{TT}^{376}.

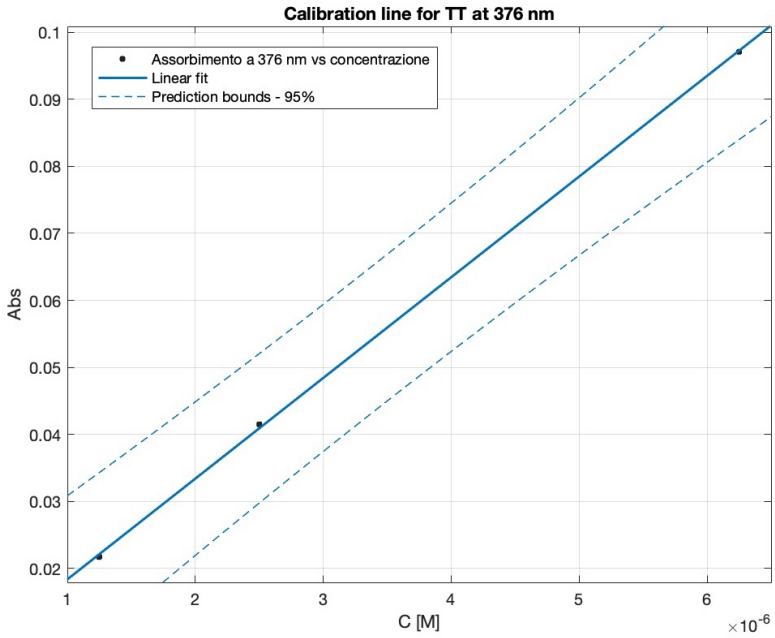

Figure 51: Calibration line to determine ε_{TT}^{376} in 50% H_2O and 50% DMSO solution. Esteemed $r^2 = 0.9998$

C_{TT} $[\mu M]$	A_{TT}^{280}	A_{TT}^{376}
1.25	0.005	0.022
2.50	0.011	0.042
6.25	-	0.097

Table 6: Concentration for the TTAI 50% H_2O and 50% DMSO solutions with the respective absorbance at 280 nm and 367 nm.

The absorbance values measured at 280 nm and 376 nm were subjected to linear regression as a function of TT concentration (**Figure 51**). The following molar extinction

coefficients were obtained from the slopes of the calibration lines: $\varepsilon^{280}_{TT\ 50\%DMSO} \approx 5200\ M^{-1}cm^{-1}$ e che $\varepsilon^{376}_{TT\ 50\%DMSO} = 15000 \pm 2600\ M^{-1}cm^{-1}$. Since only two experimental points provided reliable absorbance values at 280 nm, the coefficient $\varepsilon^{280}_{TT\ 50\%DMSO}$ must be considered as an approximate esteem. Under these conditions, it was not possible to significantly determine the uncertainty associated with the parameter.

13.4 Determination of ε^{280}_{TT} and ε^{376}_{TT} in 100% DMSO

The solutions shown in the **Table 7** were prepared and the UV-Vis spectra were measured in the range 250-600 nm and reported in **Figure 52**.

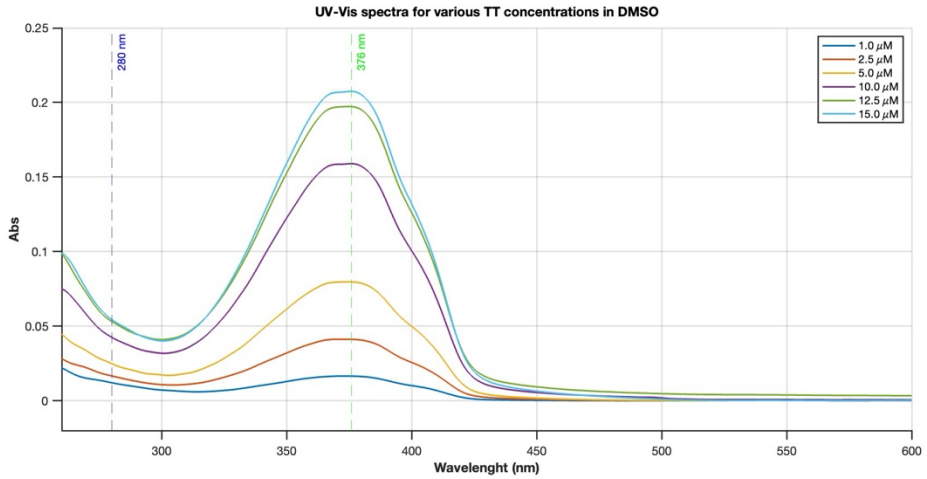

Figure 52: UV-Vis spectra for TTAI in DMSO solutions at various concentrations acquired to build the calibration line to determine ε^{280}_{TT} and ε^{376}_{TT}.

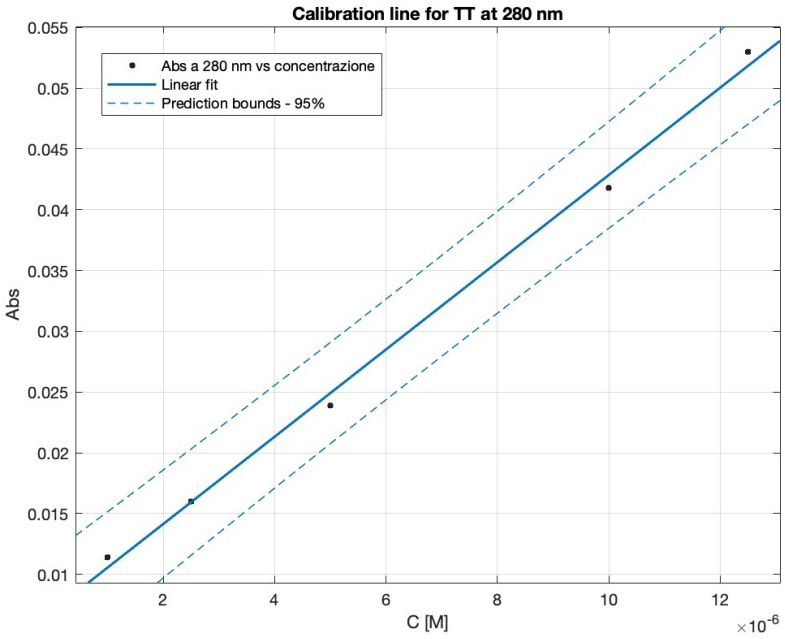

Figure 53: Calibration line to determine ε^{280}_{TT} in DMSO solution. Esteemed $r^2 = 0.9966$

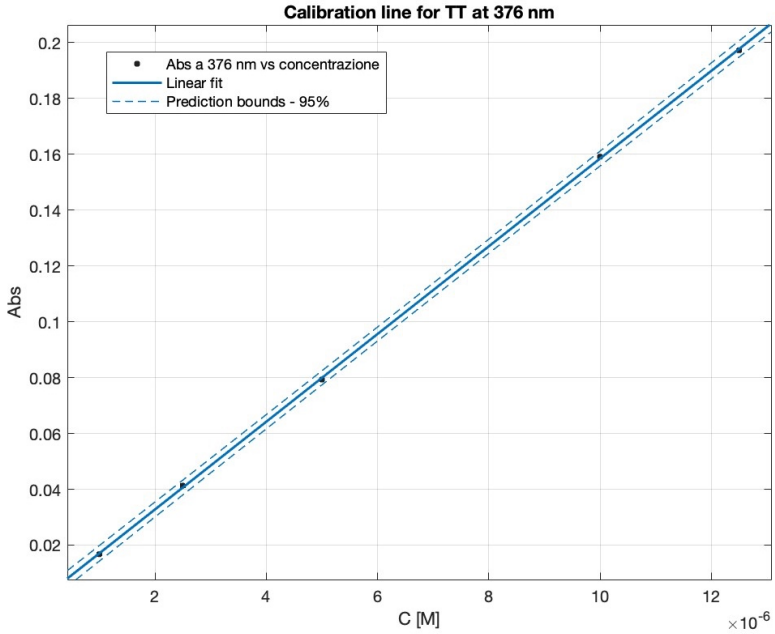

Figure 54: Calibration line to determine ε_{TT}^{376} in DMSO solution. Esteemed $r^2 = 0.9999$

C_{TT} $[\mu M]$	A_{TT}^{280}	A_{TT}^{376}
1.0	0.01	0.017
2.5	0.02	0.041
5.0	0.02	0.079
10.0	0.04	0.159
12.5	0.05	0.197

Table 7: Concentration for the TTAI DMSO solutions with the respective absorbance at 280 nm and 367 nm.

The absorbance values measured at 280 nm and 376 nm were subjected to linear regression as a function of TTAI concentration (**Figure 53** and **Figure 54**). The following molar extinction coefficients were obtained from the slopes of the calibration lines: $\varepsilon_{TT\ DMSO}^{280} = 3600 \pm 380\ M^{-1}cm^{-1}$ e $\varepsilon_{TT\ DMSO}^{376} = 15700 \pm 230\ M^{-1}cm^{-1}$.

13.5 Solvent polarity effect

As shown by the calibration lines, for the same concentration of TT and as the polarity of the solvent increases (%H_2O increasing), there is an increase in the value of the molar extinction coefficient. Therefore, as the polarity of the solvent increases, a hyperchromic effect occurs. In **Figure 8** are grouped the ε_{TT}^{376} for the three different water-DMSO-ratios solutions.

Solvent	ε_{TT}^{376} $[M^{-1}cm^{-1}]$
75% H_2O 25% DMSO	19000 ± 1600
50% H_2O 50% DMSO	15000 ± 2600
100% DMSO	15700 ± 230

Polarity ↑

Table 8: In the left column the solvent is reported in order of decreasing polarity. To the right are reported the corresponding molar extinction coefficient for TT at 376 nm.

Having the TT bound to the peptide will surround the label with an increased apolar environment in comparison to the one it can experience while free in water solution. Binding the TT to the peptide will likely decrease ε_{TT}^{376} slightly. Unfortunately, due to lack of TTAI stock solutions we were unable to determine the magnitude of this effect. M13TT characterization was made assuming TT molar extinction coefficient to be the same as the one determined for the 75% H_2O 25% DMSO solution.

13.6 Difference between free and peptide-bound TT

When TT is bound to the peptide, the label spectrum undergoes blue-shift with a maximum shift from 376 nm to 344 nm as well as showing greater band structuring, see **Figure 55**. The bathochromic effect is indicative of the presence of a dipole moment that is perturbed when the TT chromophore reaches the excited state. Electronic transitions are events occurring faster than thermal dipole rearrangement. Just after the electronic transition, the dipole moment of the excited state will interact with an arrangement of the dipole moments of the peptide and of any interacting solvent molecules that used to be favorable for the ground state. As the excited state gets destabilized, more energy will be needed to make the electronic transition happen. The effect of peak resolution, on the other hand, is typical when the chromophore is exposed to a less polar environment. As can be seen, TT exposed to water shows a wide and smooth peak, while TT bound to the peptide shows a more resolved peak where two shoulders are visible. The probe bound to the peptide will tend to have the peptide around it that limits its access to the polar environment.

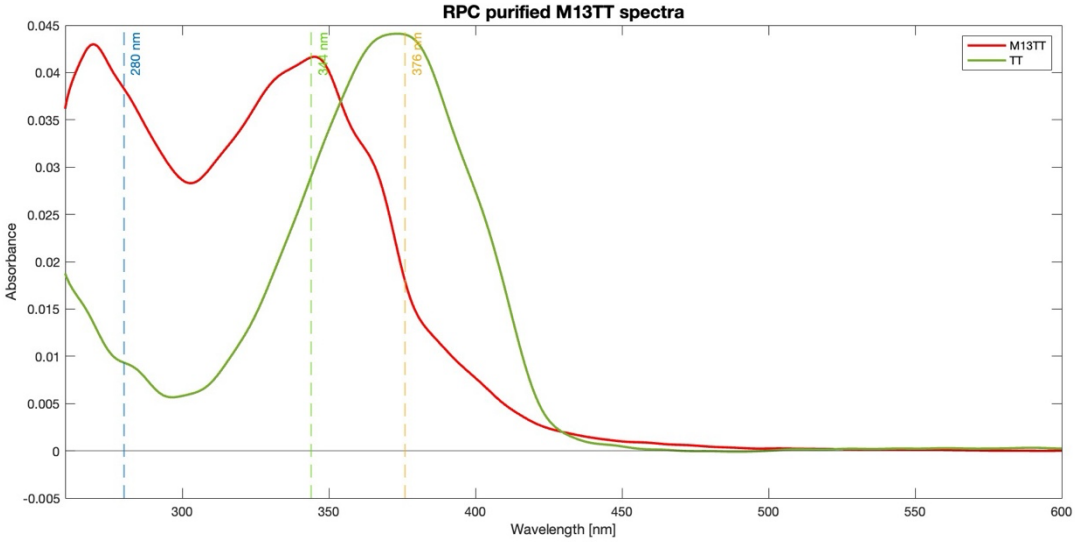

Figure 55: UV-Vis spectra of free TT in 75% H_2O 25% DMSO solution is reported in green while the one for purified M13TT in water is reported in red. It's possible to observe both the blue-shift and the increase of band resolution for the TT bound to the peptide.

13.7 Hydrolysis kinetic

Since, we suspected that the probe would have been highly unstable in an acidic environment due to the acidic hydrolysis of the label from cysteine. Therefore, before executing a RPC chromatography with TFA as a coupling agent, it was necessary to verify the stability of the probe in an acidic environment. **Figure 56** reports the UV-Vis spectra

acquired during the M13TT hydrolysis kinetic in TFA. All absorption values at 344 nm over time are reported in **Table 9**.

The hydrolysis kinetics sample was prepared dissolving $3.4 \cdot 10^{-9} mol$ in a 0.1% TFA solution of 1:4 = DMSO:MilliQ water, characterized by pH≃2. From the results of the kinetic it's possible to say that the labeled peptide is stable on a timescale that is longer than the one necessary to run a chromatography.

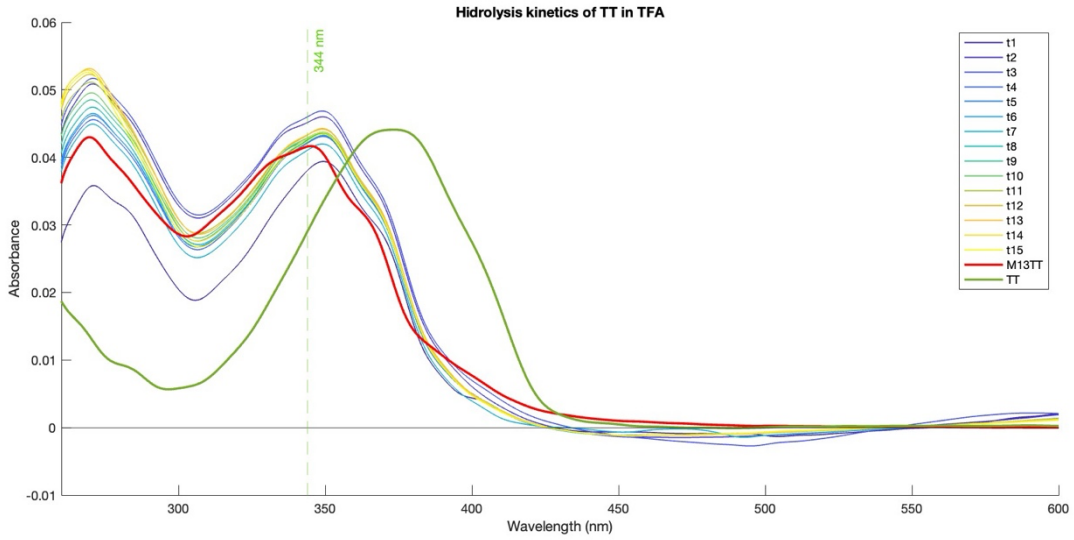

Figure 56: UV-Vis spectra acquired during the hydrolysis kinetics of M13TT. Except for the initial destabilization of the absorbance, after a short time it stabilizes. As no red shift was observed after 6 hours, we could deduce that the labeled peptide would have been stable enough to execute a RPC chromatography using TFA.

T [h:min:s]	Abs at 344 nm
00:00:00	0.038
00:02:05	0.045
00:04:27	0.046
00:06:51	0.042
00:09:13	0.043
00:11:38	0.042
00:14:05	0.041
00:18:57	0.043
00:28:57	0.043
00:44:00	0.043
01:16:30	0.043
02:17:30	0.043
03:21:30	0.043
04:45:30	0.043
06:29:30	0.042

Table 9: Evolution over time of the absorbance at 344 nm after baseline correction.

13.8 Secondary structure evaluation

In the CD spectra of a mostly α-helical protein, is it possible to observe two negative Cotton effects at ~ 205 nm and ~ 222 nm and a positive Cotton effect at about ~ 192 nm, features typical of right-handed a-helical conformations. The first two negative maxima correspond to the parallel component of the $\pi \rightarrow \pi^*$ transition and to the $n \rightarrow \pi^*$ transition of the peptide chromophore, while the positive maximum is associated to the perpendicular component of the $\pi \rightarrow \pi^*$ transition[33]. The exciton-coupling between peptides $\pi \rightarrow \pi^*$ transitions is responsible for the most intense features. The $n \rightarrow \pi^*$ transition, although electrically forbidden, is magnetically allowed and is primarily responsible for the negative band at ~222 nm.

As can be seen from **Figure 2**, the CaM sequence includes four modular EF-hand helix-loop helix subdomains, arranged in two pairs with a short flexible linker between the N- and C-terminal pairs. The overall secondary structure of CaM is characterized by a high α-helical content, as such the recorded CD spectra are coherent with the overall secondary structure content.[34]

The CD CaM100S-M13TT spectra (**Figure 57**), shows a slight change in the signal intensity of the 205 nm and 222 nm bands. The less negative signal intensity indicates loss of α-helical secondary structure of the protein. Eventually, peptide labeling through the particularly hydrophobic TT spin label can cause protein misfolding. For this sample, extending CD spectra analysis down to 190 nm was not possible. As TT absorbs under the 250 nm region, under 198 nm most of the photons originated from the Xeon arc lamp will be absorbed. To compensate this loss, the detector will increase the detector's voltage, thus increasing the noise until burying the true CD signal.

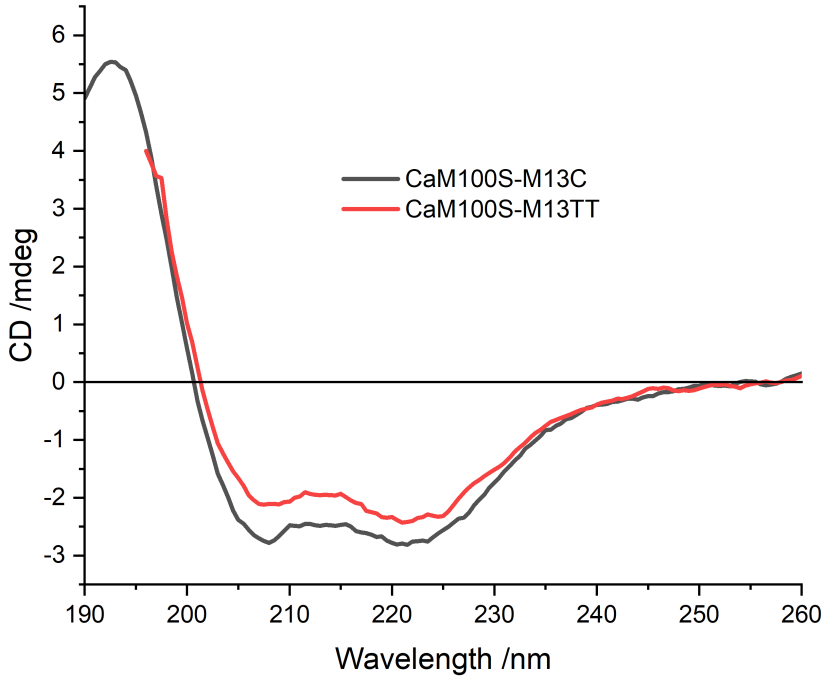

Figure 57: Circular dichroism spectra for CaM100S-M13C (black) and CaM100S-M13TT (red).

14 EPR

14.1 EDEPR

EPR spectra of photo-excited triplets are mainly governed by the dipolar electron-electron interaction, described by the zero-field splitting tensor via the D and E parameters. The parameter D mainly reflects the spatial distribution of the spin density in the triplet, while E describes the deviation from the axial symmetry of the system. As the parameter D increases, the localization of the spin density increases, while for E which tends to zero, the axiality of the system increases.

We measured the triplet state spectra of TTAI in solution; of the M13TT peptide free in solution; of the M13TT peptide bound to the three different CaM single mutants. The spectra were then simulated to obtain the g tensor, the ZFS parameters, the sublevel populations and the relative amounts of different triplets when more than one is present. The results are summarized in **Table 10**.

All spectra reported here, aside from that of free TTAI, are those resulting from the light on – light off subtraction to eliminate the contribution of stable radical species.

Specie	g_x	g_y	g_z	D	E	p_x	p_y	p_z	%
Free TT	2.0094	2.0060	2.0050	82.8	2.8	0.21	0.79	0.00	100
M13TT	2.0086	2.0062	2.0051	97.7	18.9	0.07	0.93	0.00	90.9
	2.0094	2.0085	2.0050	97.7	6.3	0.21	0.79	0.00	9.1
CaM6S M13TT	2.0086	2.0062	2.0051	97.7	18.9	0.07	0.93	0.00	75.9
	2.0094	2.0060	2.0050	82.8	2.8	0.21	0.79	0.00	15.3
	2.0094	2.0085	2.0050	97.7	6.3	0.21	0.79	0.00	8.8
CaM100S M13TT	2.0087	2.0072	2.0056	97.1	18.4	0.10	0.90	0.00	74.6
	2.0094	2.0060	2.0050	82.8	2.8	0.21	0.79	0.00	16.9
	2.0094	2.0085	2.0050	97.7	6.3	0.21	0.79	0.00	8.5
CaM114S M13TT	2.0085	2.0070	2.0052	97.2	18.4	0.10	0.90	0.00	75.8
	2.0094	2.0060	2.0050	82.8	2.8	0.21	0.79	0.00	15.8
	2.0094	2.0085	2.0050	97.7	6.3	0.21	0.79	0.00	8.4

Table 10: List of the parameters used for the EasySpin[24] simulation of triplet spectra. Orange refers to free TT parameters. Green refers to the lowest populated triplet specie in the M13TT triplet. White refers to the highest populated triplet specie of each sample. Gaussian broadening was set to 3 for every simulation. Constants are reported for all the studied samples. In the % column is reported the weight of the various triplet species in each sample.

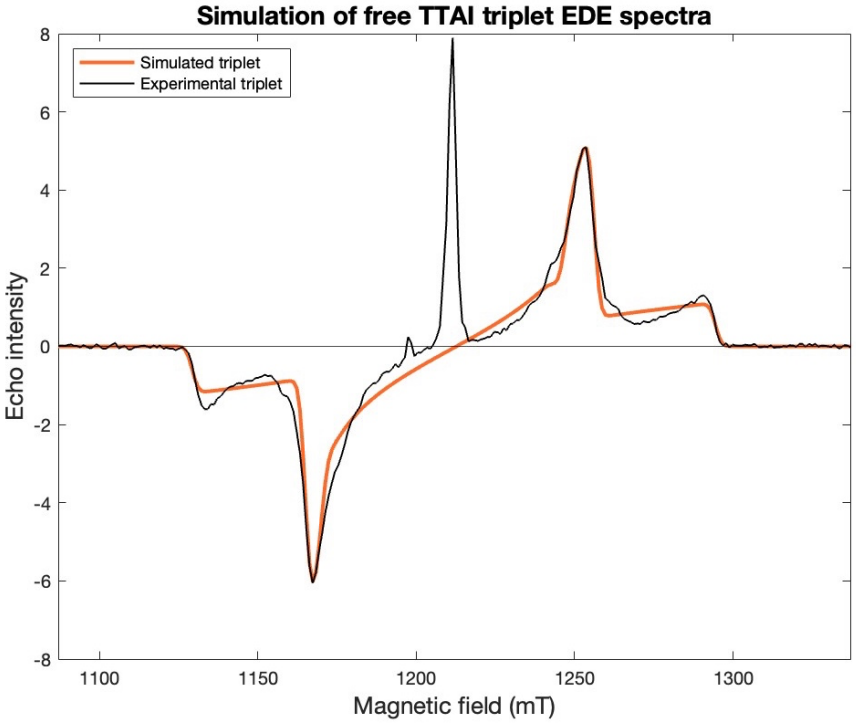

Figure 58: Simulation of the echo detected triplet spectra for a 100 μM TTAI label in DMSO:H_2O:$Glycerol_D$=1:1:1solution. The experimental triplet was acquired from 1088 mT to 1328 mT recording 250 points over 1 average. Pulsed microwave was set at 7.96 mJ and 3.40223e+10 GHz. For the simulation parameters refer to ***Table 10****.*

The free TTAI (**Figure 58**) shows a typically axial triplet EPR spectrum populated by ISC. The spike in the center of the spectrum is the signal of the TT radical that will be discussed later. The spectrum of M13TT (**Figure 59**), shows the presence of two rhombic triplet species, populated by ISC indicating the presence of at least two distinct conformations of the probe.

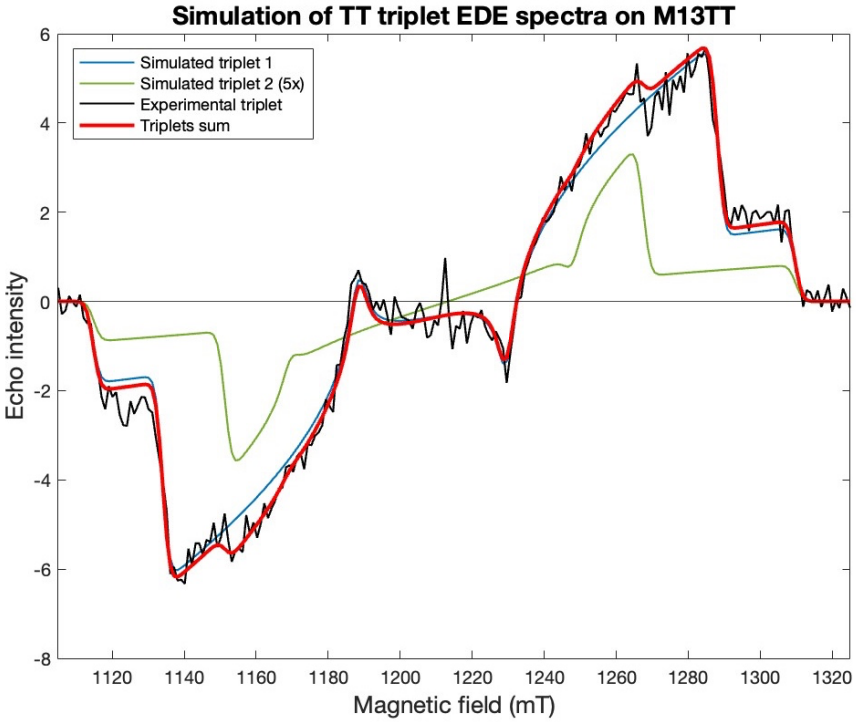

Figure 59: Simulation of the echo detected triplet spectra for a 80 μM M13TT in D_2O: $Glycerol_D$ =1:1 solution. The experimental triplet was acquired from 1105 mT to 1325 mT recording 220 points over 1 average. Pulsed microwave was set at 10.02 mJ and 3.40369e+10 GHz. For the simulation parameters refer to ***Table 10****.*

The comparison of the two spectra shows that TTAI has a lower D value than that of M13TT. A decrease in D is consistent with a greater delocalization of the triplet's electron density, suggesting that in the free sample the terthiophene structure may take on more planar conformations on average. In oligothiophene systems, planarization of the π-conjugate backbone increases the extent of electron conjugation as can be seen from (**Figure 60**). This results in a greater average separation of the spin density in the excited triplet and therefore a reduction in the electron dipole interaction, experimentally observed as a decrease in the D parameter. Furthermore, the lower value of E observed for the triplet of the free probe is indicative of a greater axial symmetry, as well as agreeing with the possibility of assuming more planar conformations on average. The two components of M13TT differ mainly in the ZFS parameters, suggesting different geometries of the π-conjugate system. Specifically, they show identical D but different E. This means that the delocalization of the electron density of the triplet is identical but that the two shapes have different axial symmetry. As a result, the increased D and lower E when TT is bound to the peptide, suggests that the probe twists as in **Figure 61** and one of the rings is removed from the conjugation thereby assuming ZFS parameters and polarization like those of dithiophene[15,35]. The simulated ZFS parameters (D/E = 83/2.8 mT) for the free TT are compatible with the ones for a *trans/trans* TT as reported form[11] (D/E = 83/2.1 mT). The peptide-bound TT has a D parameter (98 mT) that is closer to the one of dithiophene (104 mT) than the one of terthiophene, suggesting that the probe will tend to present a dithiophene-like triplet state spin density. In the case of M13-bound TT our simulated E values suggest a *cis/cis* configuration as reported from.[11] The initial populations value for free TT are very close to the ones defined from article.[11]

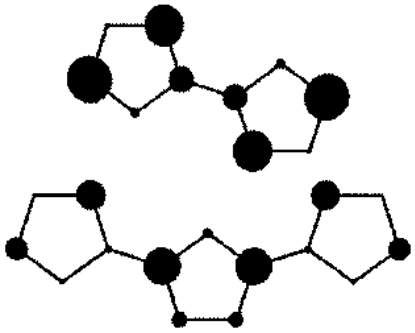

Figure 60: Schematic representation of calculated π-spin densities in the lowest excited triplet state of dithiophene and terthiophene. Calculations are based on a simple π-electron (one-electron-per-site) model including electron-electron interaction at the extended Hubbard level.[11]

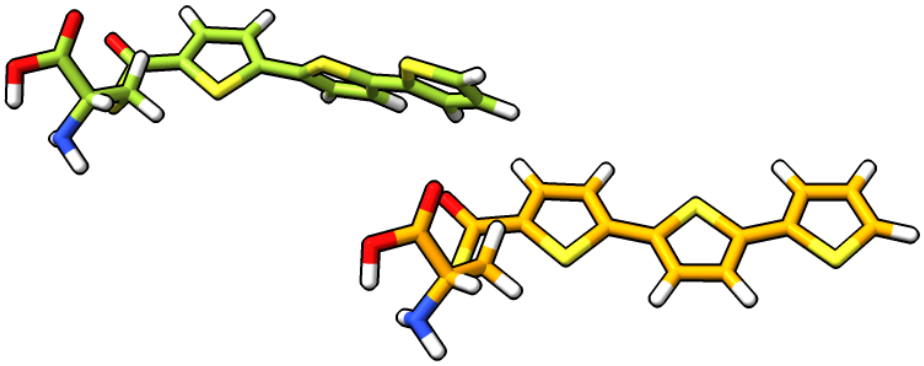

Figure 61: TTAI planar (orange) and twisted (green) configuration. The first one can be observed for free TTAI, while the second for M13-bound TT.

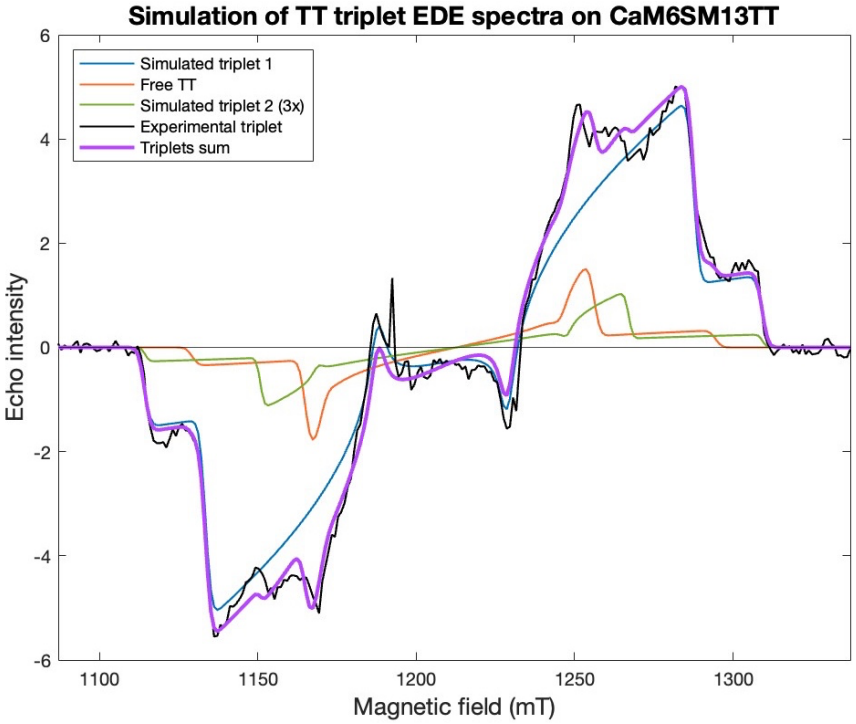

Figure 62: Simulation of the echo detected triplet spectra for a 80 μM CaM6SM13TT in D_2O: $Glycerol_D$ =1:1 solution. The proportion CaM6S:M13TT:Ca^{2+}=1:1.2:20 was used for sample preparation. The experimental triplet was acquired from 1087 mT to 1327 mT recording 250 points over 1 average. Pulsed microwave was set at 7.96 mJ and 3.40158e+10 GHz. For the simulation parameters refer to ***Table 10****.*

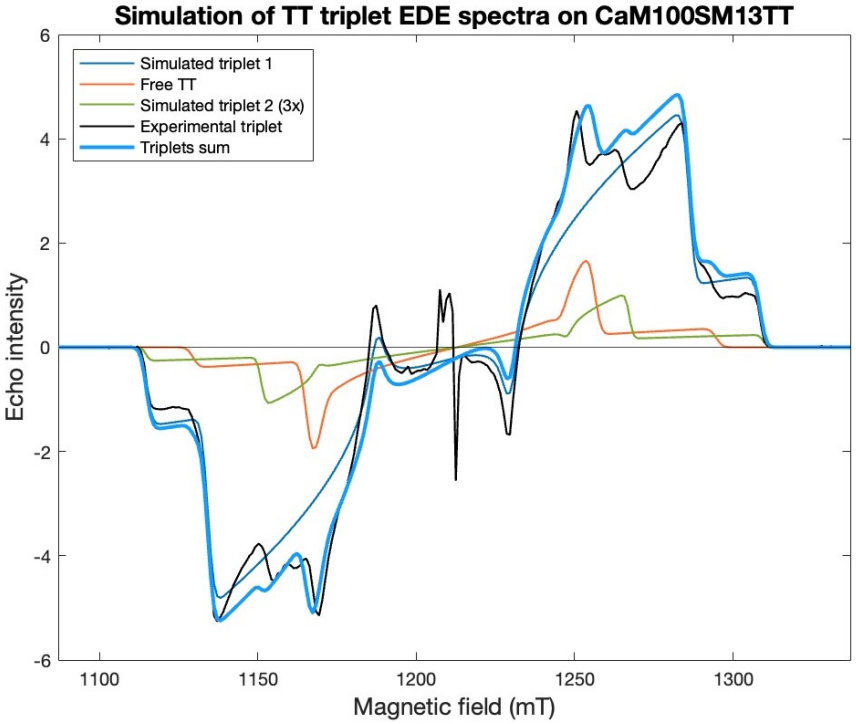

Figure 63: Simulation of the echo detected triplet spectra for a 80 μM CaM100SM13TT in D_2O: $Glycerol_D$ =1:1 solution. The proportion CaM100S:M13TT:Ca^{2+}=1:1.2:20 was used for sample preparation. The experimental triplet was acquired from 1087 mT to 1327 mT recording 250 points over 1 average. Pulsed microwave was set at 10.02 mJ and 3.40294e+10 GHz. For the simulation parameters refer to ***Table 10****.*

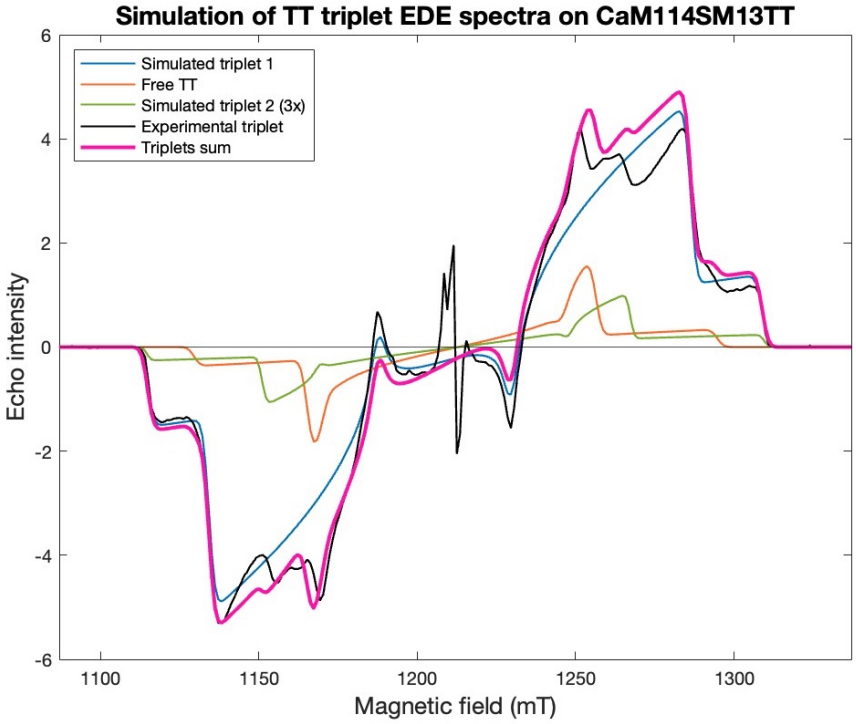

Figure 64: Simulation of the echo detected triplet spectra for a 80 μM CaM114SM13TT in D_2O: $Glycerol_D$ =1:1 solution. The proportion CaM114S:M13TT:Ca^{2+}=1:1.2:20 was used for sample preparation. The experimental triplet was acquired from 1105 mT to 1325 mT recording 220 points over 1 average. Pulsed microwave was set at 10.02 mJ and 3.40369e+10 GHz. For the simulation parameters refer to ***Table 10****.*

The triplet spectra of CaM6S, CaM100S and CaM114S complexes require the superposition of three triplet components to be reproduced correctly. The corresponding simulations are reported in **Figure 62**, **Figure 63** and **Figure 64**. Comparing the parameters used to simulate the M13TT triplet with the ones used to simulate CaM-peptide complexes, the two predominant triplet species are almost identical. The third species is consistent with a small amount of free label, likely detached after the lyophilization process to prepare the samples. The triplet spectra of CaM6S, CaM100S and CaM114S complexes are substantially indistinguishable within experimental resolution. This suggests that the surroundings of the terthiophene probe and its conformational distribution remain similar in the three complexes. Since ZFS parameters are extremely sensitive to local electron geometry, the absence of significant variations indicates that the formation of the complex with CaM does not substantially alter the average conformation of the probe. Covalently binding the probe to the M13 peptide is what introduces main conformational constraints that favor less planar constraints than the free probe.

A further peculiarity of the ED-EPR spectra is represented by the progressive decrease in the intensity of the triplet signal towards increasing values of the magnetic field. This behavior can be attributed to the photoinduced formation of the terthiophene cation radical during spectrum acquisition. The progressive conversion of part of the triplet population into radical species therefore determines a reduction in the intensity observed at high field values since the high-field regions are acquired later than the low-field ones.

14.2 Laser-stimulated radical growth

After 355 nm laser illumination, in addition to the triplet state of the terthiophene spin probe, the rapid formation of a radical species is also observed, hypothetically attributed to a terthiophene radical. The ED-EPR spectra at 80 K of the g~2 region of CaM6S + M13TT as a function of laser illumination time (7.3 mJ/shot) are reported in **Figure 65**; for convenience, the spectra are reported using the g factor scale. The signal shows initially just the spectrum of the nitroxide radical on CaM (black spectrum); in 80 s of total laser illumination, the photogenerated radical contribution grows almost larger than that of the nitroxide. The small signal at $g = 2.03$ is a background signal originating from the cavity, while the photogenerated radical contribution appears as a signal centered at about $g = 2.004$, corresponding to the central region of the triplet spectrum.

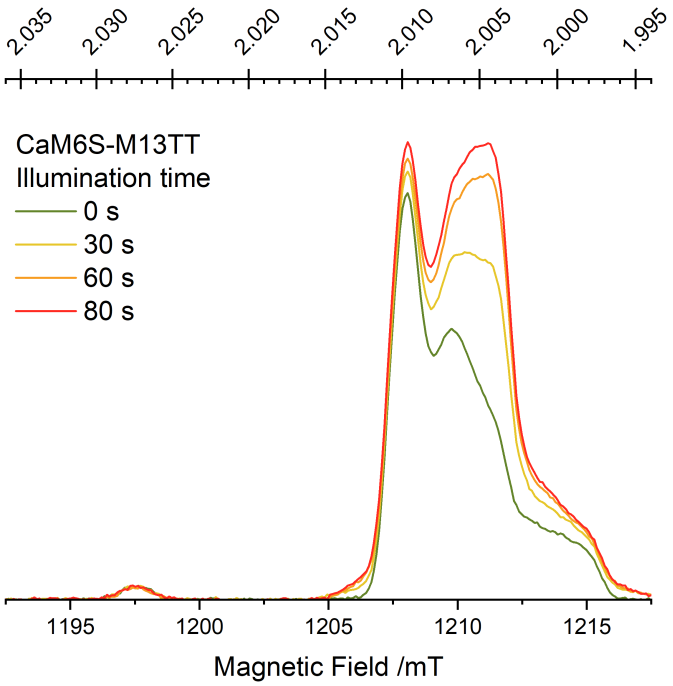

Figure 65: TT photoinduced radical growth in the CaM6SM13TT complex. Quick radical formation is observed.

The simultaneous observation of the triplet state and the radical highlights the terthiophene photochemical bivalent nature, see **Figure 58**. If the sample containing TT is lit for long times, those typical of a ReLaser-IMD experiment, around 10 to 15 hours, the radical signal progressively increases but the triplet is still visible (**Figure 66**). In addition, a broad signal (400 mT wide) is visible from the ED-EPR spectra at the base of the radical. The lineshape is characterized by an axial g tensor. Unfortunately, it was not possible to assign it, due to its low intensity and superposition with the other signals.

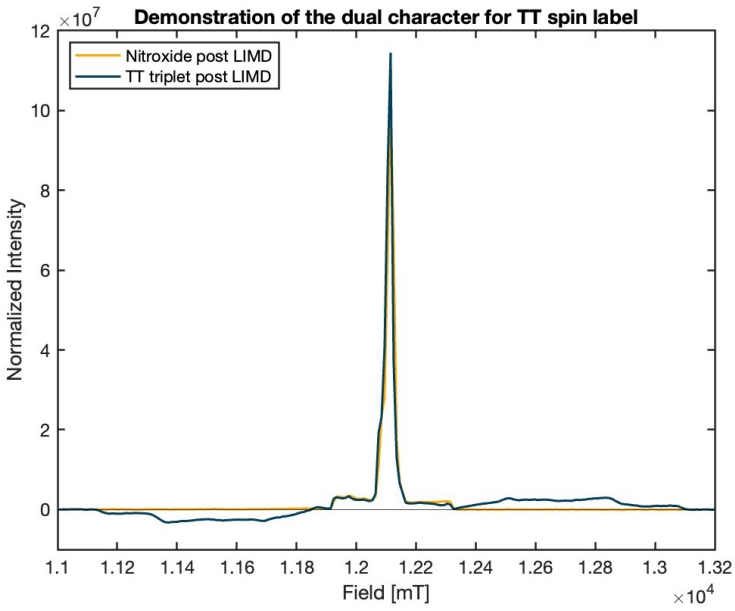

Figure 66: ED-EPR executed for the CaM6SM13TT complex after an overnight ReLaser-IMD experiment. In yellow is reported the non-lit measurement, while in blue the lit one.

To verify whether the radical formation is tied to the presence of TT we performed the ED-EPR spectra of the g~2 region of CaM100S + M13C as a function of laser illumination time (7.3 mJ/shot); for convenience, the spectra are reported in **Figure 67** using the g factor scale. When TT is absent in the sample, light induced radical formation is still observed, but with a much slower growth rate. This weaker contribution at g=2.005 comes from the light-induced radicals originating in the protein.

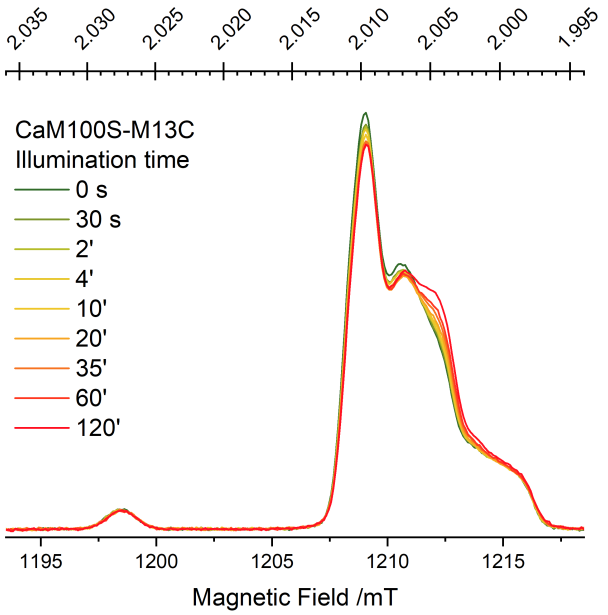

Figure 67: TT photoinduced radical growth in the CaM100SM13C complex. Slow radical formation is observed.

14.3 DEER

DEER measurements were done to determine the intracomplex NO•—TT• distances and to prove whether the TT radical is suitable as a spin label for distance measurements. For this purpose, the three CaM mutants (positions 6-100-114) were analyzed in presence of M13TT. As reported in the experimental part, we detect on the nitroxide and pump on the photogenerated radicals.

Evolution time from the acquired dipolar traces do not exceed 3 μs to preserve a reasonable signal-to-noise ratio (SNR). This time window limits the maximum interspin distance that can be reliably determined, making distributions at distances greater than about 4 nm progressively less accurate. Contributions beyond ~5 nm cannot be considered even qualitatively reliable under the experimental conditions used.

For all the samples analyzed, a modulation depth below 5% is obtained. This value indicates weak dipolar coupling and low fraction of coupled spins suggesting that the radical coupled with the NO• will be present just in few peptide-protein complexes.

The SNR of the traces was calculated as the ratio between the modulation depth (as a measure of the signal) and baseline root mean square error after background subtraction. No SNR greater than 50 was obtained, indicating significant noise present and inability to extract artifact-free distance distributions.

Based on the growth of the radical described in the previous paragraph, in **Figure 68** the results for DEER measurement after short and long illumination period are provided for single mutant CaM100S complexing M13TT, both measured in the presence of a 20-fold excess of Ca^{2+}. To identify the distances related to TT, the DEER of CaM100S-M13C illuminated for two hours is also reported. Panel (A) displays the background-corrected and fitted time traces, while panel (B) shows the corresponding distance distributions. The values obtained from data analysis are summarized in **Table 11**.

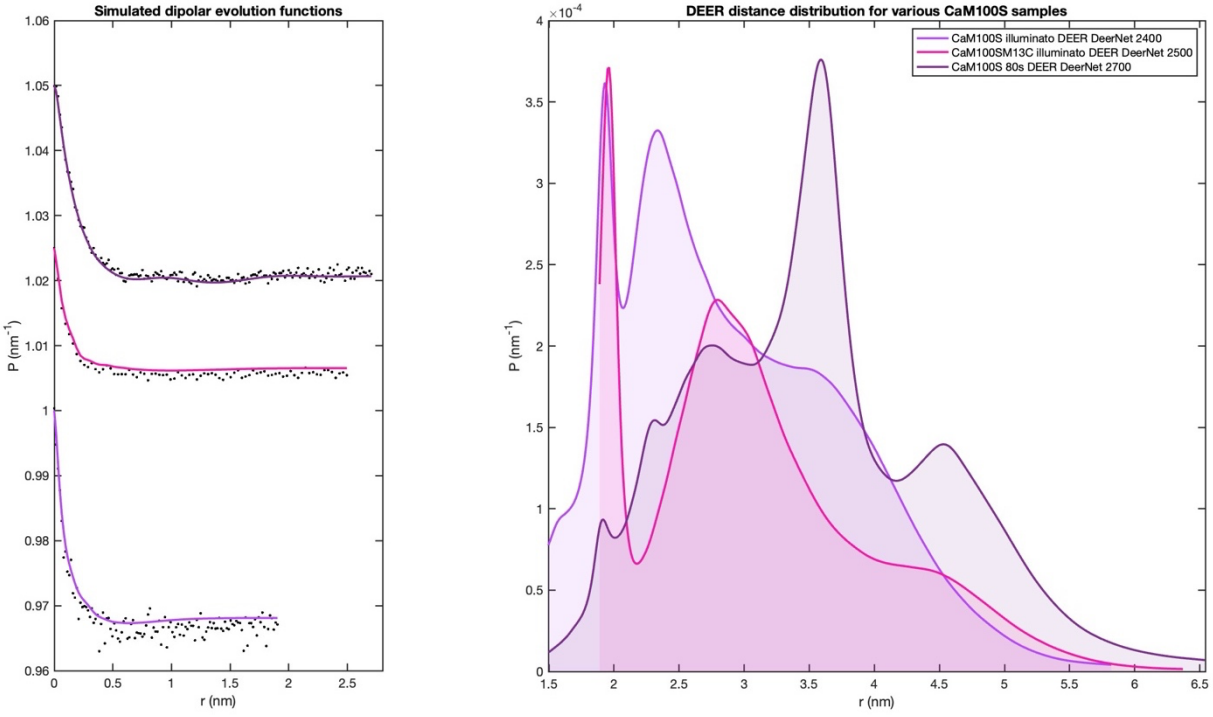

*Figure 68: Q-band (80K) 4-pulse DEER results of CaM100S with M13TT or M13C at different illumination times. (**A**) Background corrected time traces. Black dotted lines represent the experimental raw data while the colored line show the homogeneous 3D background fit obtained with DeerAnalysis2022. (**B**) Distance distribution computed with DeerNet from DeerAnalysis2022.*

The analysis of the DEER time traces showed a surprising result, we expected a single, well-defined distance, but we observe a high number of peaks. The main peak for a short illumination time (dark purple in **Figure 68**) is at 3.6 nm with additional maxima at 1.8 and 2.4 nm. The same peaks appear also after prolonged irradiation but with a redistribution of intensities. Some of the peaks are also observed in the distance distribution in the absence of TT. The peak at 1.8 nm is clearly present in both CaM100SM13C and CaM100SM13TT samples subjected to prolonged illumination, while it is only hinted for CaM100SM13TT illuminated 80 s. The presence of the signal even in the system without TT suggests that the formation of the radical pair responsible for this distance doesn't involve terthiophene, even considering the different possible conformers. The presence of additional radical species is then needed to explain the distance distributions. In particular, for longer illumination times the DEER traces could include not only NO-radical contributions, but also radical-radical contributions since the signals are partially overlapping. The presence of more than two radical centers complicates the analysis since combination peaks might be present.

To get a deeper insight into the nature of the distances we observe, a model of the protein-M13TT complex has been created in Chimera starting from the available structures constructed using AlphaFold v.3[30], shown in **Figure 70**, **Figure 71** and **Figure 72**. The amino acids that can form radicals are primarily the aromatic ones, especially Trp (present only on M13) and Tyr (two of them are present on CaM).[36]

From the analysis of the protein model, the 1.8 nm distance could be associated with a NO•—Trp• distance. The same considerations can be made for the region around 3.0 nm: it maintains almost constant shape and intensity for the three distributions. This contribution might instead result from a superposition of multiple aromatic radical interactions or from an intrinsic conformational distribution of the system. In the presence of TT, the peaks at 2.4 and 3.6 nm are affected by a variation in intensity depending on the illumination time. Since the concentration of the TT radical should increase for increasing illumination times, it is inferred that the peak at 2.4 nm is representative for a distance directly involving the TT. Referring to the protein model it can be associated both to NO•—TT• and TT•—Tyr• distances. From the molecular model no distances between radical pairs can be associated to the 3.6 nm distance. We deduce that the corresponding peak might originate from a superposition of multiple aromatic radical interactions involving TT and that is relevant just for short illumination times. The longer distances are not reliable in view of the trace evolution time and the SNR of the experiment, and in addition they are hard to justify since properly folded CaM largest diameter is around 4 nm. Therefore, it is possible that these distances are either artefacts or suggest that part of the protein is partially misfolded or aggregated, likely because of the hydrophobicity of TT and the freeze-dry of the sample. Indeed, the recorded CD spectra (Errore. L'origine riferimento non è stata trovata.) of the CaM100S-M13TT protein complex showed a somewhat reduced CD signal possibly indicating that the TT perturbs the protein structure.

DEER	Modulation depth	Baseline ε_{rms}	SNR	Fit ε_{rms}	$\bar{d}$ [nm]	$\sigma_{\bar{d}}$ [nm]
CaM100S M13TT short	2.9%	0.70e-3	41.4	0.69e-3	3.53	±1.0
CaM100S M13TT long	3.3%	1.25e-3	26.3	1.75e-3	2.9	±0.9
CaM100S M13C	1.9%	0.38e-3	49.7	1.27e-3	3.2	±0.9

Table 11: DEER data analysis for long illuminated CaM100SM13C, short and long illuminated CaM100SM13TT in presence of an excess of Ca^{2+}.

In **Figure 69** the results for DEER measurement after a short lighting period are provided for single mutant CaM6S, CaM100S and CaM114S complexing M13TT, all measured in the presence of a 20-fold excess of Ca^{2+}. Panel (A) displays the background-corrected and fitted time traces, while panel (B) shows the corresponding distance distributions. The values obtained from data analysis are summarized in **Table 12**.

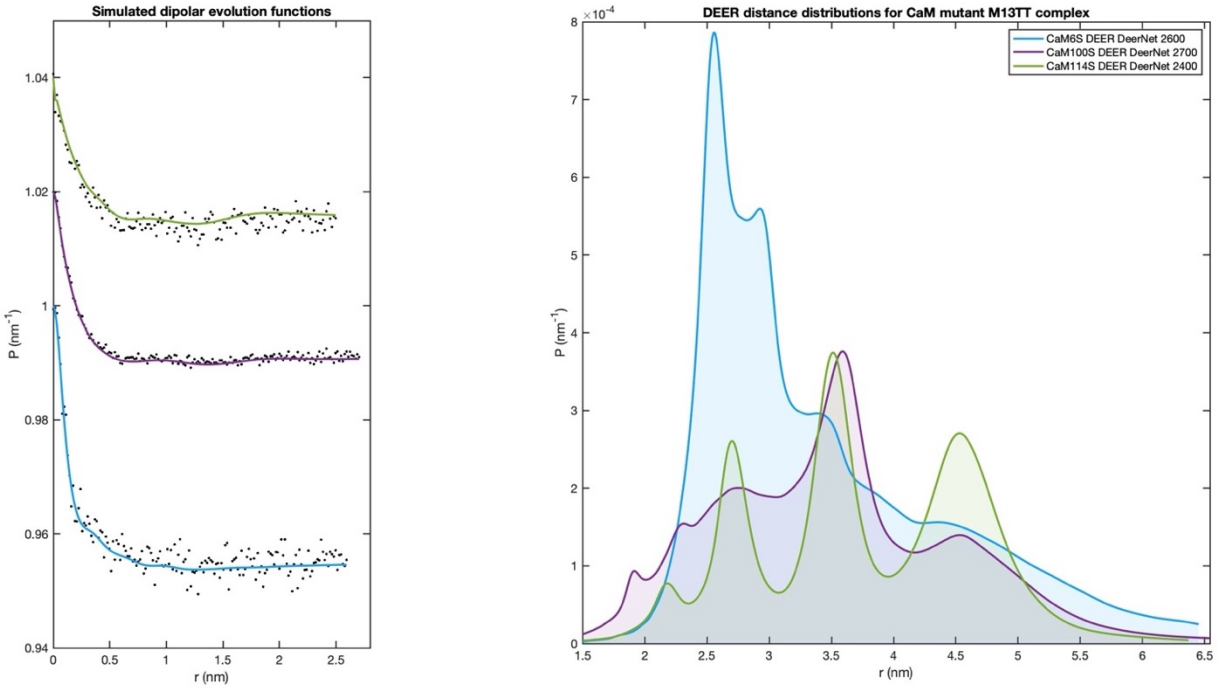

*Figure 69: Q-band (80K) 4-pulse DEER results of CaM6S, CaM100S and CaM114S complexing M13TT at short illumination times. (**A**) Background corrected time traces. Black dotted lines represent the experimental raw data while the colored line show the homogeneous 3D background fit obtained with DeerAnalysis2022. (**B**) Distance distribution computed with DeerNet from DeerAnalysis2022.*

DEER	Modulation depth	Baseline ε_{rms}	SNR	Fit ε_{rms}	$\bar{d}$ [nm]	$\sigma_{\bar{d}}$ [nm]
CaM6S	4.4%	2.03e-3	21.6	2.27e-3	3.4	±1.0
CaM100S	2.9%	0.70e-3	41.4	0.69e-3	3.5	±1.0
CaM114S	3.0%	1.46e-3	20.5	1.86e-3	3.5	±1.1

Table 12: DEER data analysis on CaM6S, CaM100S and CaM114S + M13TT peptide in presence of an excess of Ca^{2+}.

The resulting DEER distances were compared with the ones measured in the protein model, reported in **Table 13**, **Table 14** and **Table 15**:

- CaM6SM13TT is characterized by the longest distances in comparison with the other samples. The peak a 2.5 nm can be associated to the NO•—TT• and NO•—Trp• distance, while the one at 3.5 nm can be associated to NO•—Tyr• distance. The respective molecular model is reported in **Figure 70**.
- CaM100SM13TT has both a protein model close to the CaM114SM13TT one and a similar distance distribution. It's the mutant with the smallest NO•—Trp• distance. Therefore, it's the only one showing a peak at 1.8 nm. As said before, the peak at 2.4 nm can be associated either to the NO•—TT• distance, while the peak at 3.6 nm

remains of difficult association. The respective molecular model is reported in **Figure 71**.

- CaM114SM13TT shows four well distinguished bands. The one at 2.1 nm can be associated to NO•—Trp• distance, the one at 2.6 nm to NO•—TT• distance and the one at 3.5 nm NO•—Tyr• distance. As such long distances can't exist in CaM, the band at 4.5 nm could either come from experimental noise or misfolded protein. The respective molecular model is reported in **Figure 72**.

All experimental traces have a limited SNR despite acquisition times on the order of 14 h. As a result, the distance distributions obtained are characterized by a relatively wide range of uncertainty. Therefore, the interpretation of the results was mainly focused on the most robust characteristics of the distributions.

The local mobility of the probe naturally widens the distribution of distances. The amplitude of the distributions obtained reflects the conformational heterogeneity of the probe, which turned out to be more mobile than had been assumed at the beginning of the project.

Besides the precise interpretation of the distance distributions, what emerges from the DEER analysis is that TT acts as a photosensitizer for radical formation, thus boosting the radical formation kinetic on neighboring amino acids.[37] Overall, it is clear that photogeneration of the TT radical is not suitable for DEER experiments.

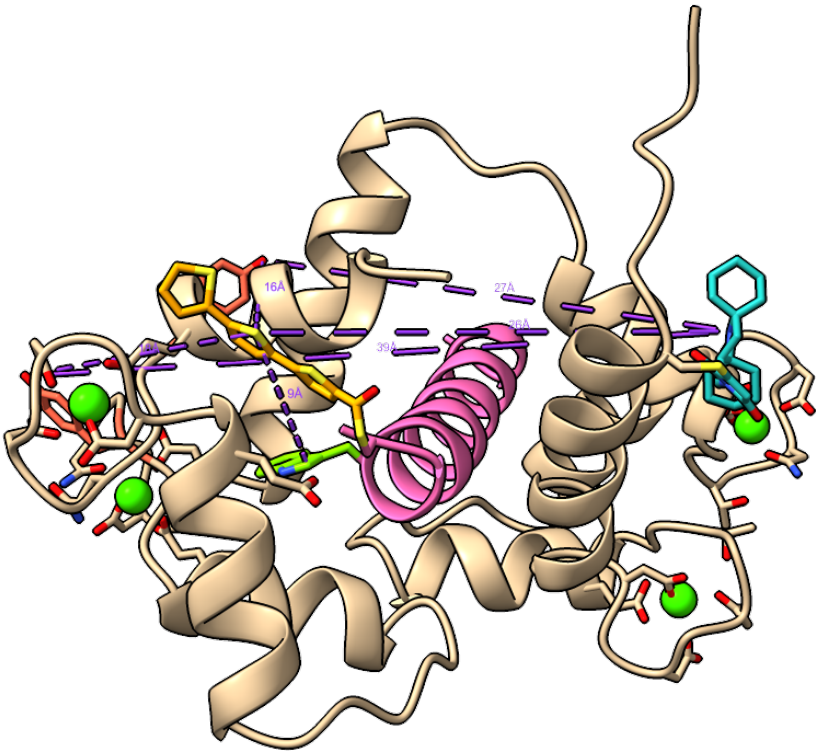

Figure 70: CaM6S-M13TT ChimeraX representation. SPIRO is colored in blue, TT in yellow, Trp in green and Tyr in orange. Relevant distances are reported in purple.

Couple	d [nm]
NO•—TT•	2.6
NO•—Tyr•	2.7 and 3.9
NO•—Trp•	2.5
TT•—Tyr•	1.6 and 1.8
TT•—Trp•	0.9
Trp•—Tyr•	1.5 and 1.7

Table 13: CaM6S-M13TT distances from molecular model.

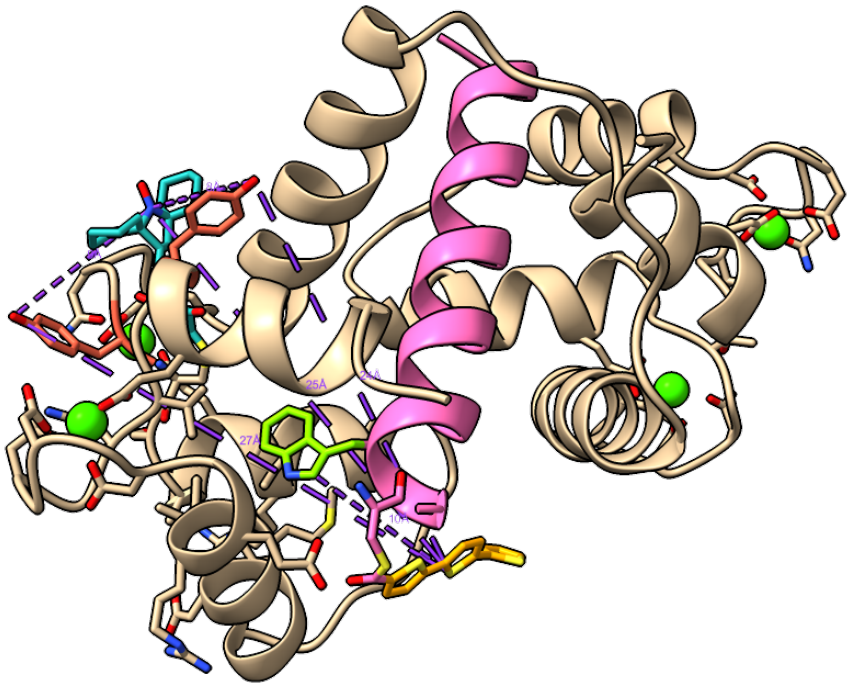

Couple	d [nm]
NO•—TT•	2.5
NO•—Tyr•	0.8 and 0.9
NO•—Trp•	1.7
TT•—Tyr•	2.4 and 2.7
TT•—Trp•	1.0
Trp•—Tyr•	1.5 and 1.8

Table 14: CaM100S-M13TT distances from molecular model.

Figure 71: CaM100S-M13TT ChimeraX representation. SPIRO is colored in blue, TT in yellow, Trp in green and Tyr in orange. Relevant distances are reported in purple.

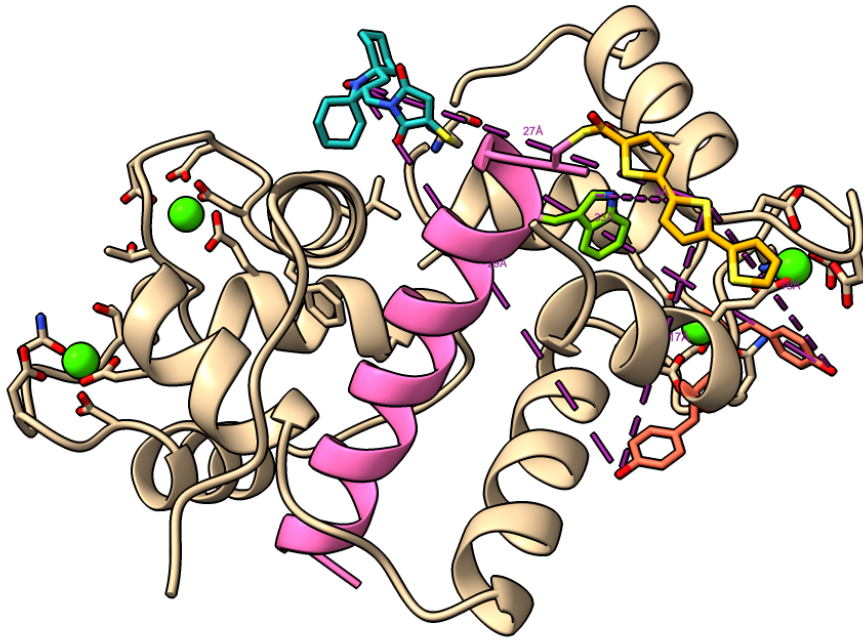

Couple	d [nm]
NO•—TT•	2.5
NO•—Tyr•	2.9 and 3.3
NO•—Trp•	1.9
TT•—Tyr•	1.7 and 1.8
TT•—Trp•	0.9
Trp•—Tyr•	1.6 and 1.8

Table 15: CaM114S-M13TT distances from molecular model.

Figure 72: CaM114S-M13TT ChimeraX representation. SPIRO is colored in blue, TT in yellow, Trp in green and Tyr in orange. Relevant distances are reported in purple.

14.4 ReLaser-IMD

As for the DEER measurements, the Laser-IMD technique was used to determine the distance distribution between TT bound to M13 peptide and the SPIRO probe bound to CaM. In this case, however, the TT species that is involved is the triplet state of the chromophore.

Compared to DEER experiments, Laser-IMD measurements were more complex due to the competitive photogeneration of the TT radical. Using a probe that undergoes photoreduction during the experiment, the progressive TT conversion to a radical leads to a reduction in the triplet population available for ReLaser-IMD measurements and contributes to the worsening of the SNR. Consequently, ReLaser-IMD measurements show a lower SNR compared to DEER. Nevertheless, even for prolonged illumination, not all TT is converted to its radical form, as **Figure 66** shows, the triplet signal is still visible after a ReLaser-IMD experiment. Additionally, the ReLaser-IMD trace in the beginning appears distorted and its intensity increases rather than showing a decay as expected. After about one hour of laser illumination the trace becomes stable and has the proper decay shape. To ensure that no further distortions are present during the long experiment, each acquisition was saved separately and inspected before obtaining the final average.

The background contribution was removed from the dipolar signal fitting data from 1000 ns to about 2400 ns. The background contribution was simulated through an exponential function using DeerAnalysis MatLab® tool. Tikhonov regularization was applied to define the optimum compromise between goodness of the fitting and smoothness of the distance distribution.

For all the samples analyzed, a modulation depth below 1% is obtained. This value indicates weak dipolar coupling and a low fraction of coupled spins.

The SNR was estimated in the same way as for DEER measurements. No SNR greater than 15 was obtained, indicating significant noise presence and inability to extract highly reliable and artifact-free distance distributions. With such a low SNR, distances over 4.0 nm will be severely affected by artifacts and therefore unreliable.

In **Figure 73** the results for ReLaser-IMD measurement are provided for single mutant CaM6S, CaM100S and CaM114S complexing M13TT, all measured in presence of a 20-fold excess of Ca^{2+}. Panel (A) displays the background-corrected and fitted time traces, while panel (B) shows the corresponding distance distributions. The values obtained from data analysis are summarized in **Table 16**.

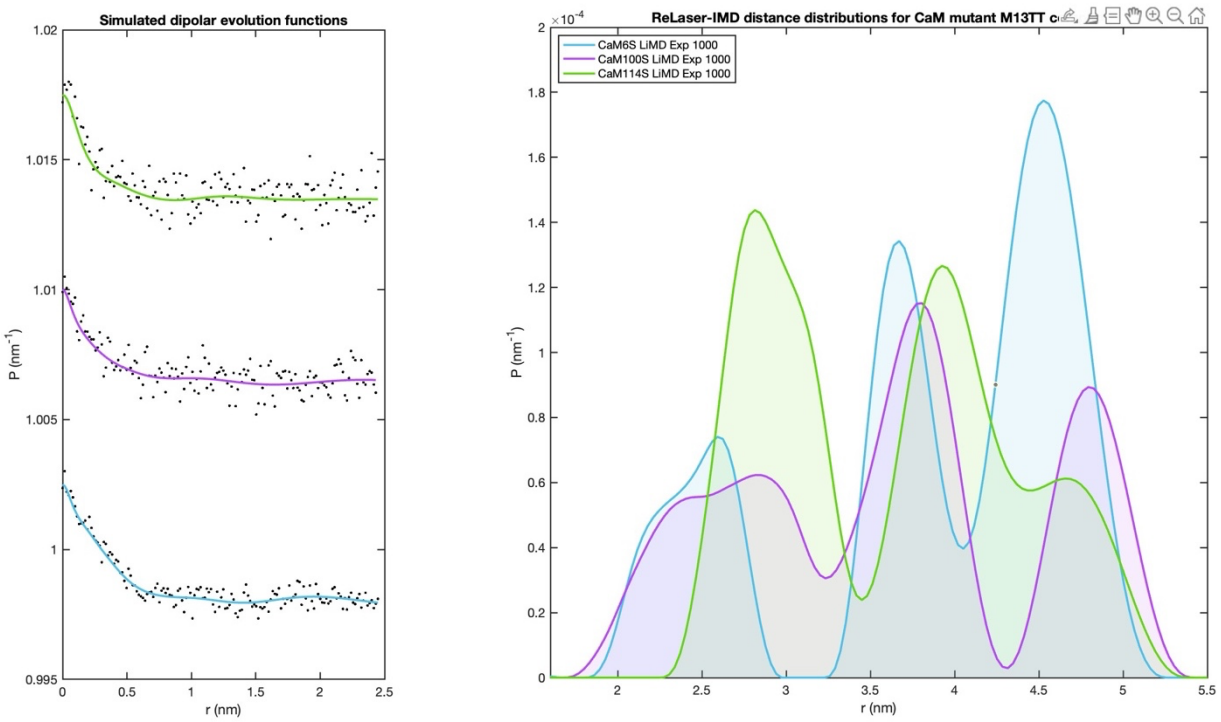

*Figure 73: Q-band (80K) ReLaser-IMD results of CaM6S, CaM100S and CaM114S complexing M13TT. (**A**) Background corrected time traces. Black dotted lines represent the experimental raw data while the colored line show the homogeneous 3D background fit obtained with DeerAnalysis2022. (**B**) Distance distribution computed with DeerNet from DeerAnalysis2022.*

ReLaser-IMD	Modulation depth	Baseline ε_{rms}	SNR	Fit ε_{rms}	$\bar{d}$ [nm]	$\sigma_{\bar{d}}$ [nm]
CaM6S	0.5%	0.32e-3	15.4	0.29e-3	4.3	±1.2
CaM100S	0.3%	0.52e-3	5.8	0.50e-3	4.0	±1.2
CaM114S	0.4%	0.62e-3	6.5	0.62e-3	3.9	±1.1

Table 16: ReLaser-IMD data analysis on CaM6S, CaM100S and CaM114S + M13TT peptide in presence of an excess of Ca^{2+}.

Since ReLaser-IMD specifically measures distances between a stable radical and a photoinduced triplet species, it allows to isolate the distance distributions involving TT. The distance values under 3.2 nm can be well described by the simulated peptide-protein complex structure considering the distance between the central TT ring and the nitrogen atom of the SPIRO label. As discussed for the DEER traces longer distances are hard to justify in a properly folded protein. Overall, ReLaser-IMD distance distribution region under 3.2 nm resembles the DEER one, therefore confirming association to NO•—TT• and TT•—Tyr• distances.

Conclusions

This thesis investigated the applicability of terthiophene acetyl-imidazole (TTAI) as a novel photoexcitable spin label for pulsed EPR distance measurements using the well-characterized CaM–M13 system as a model platform. The study combined site-directed spin labeling, chromatographic purification, spectroscopic characterization, and pulsed dipolar EPR techniques to evaluate both the chemical suitability of TTAI and its performance in DEER and ReLaser-IMD experiments. While terthiophene (TT) finds its main applications in molecular electronic devices, the possibility to photoinduce its triplet state inspired this work. No previous attempts at using TT as a photoexcitable spin probe have been reported in the literature, potentially making TTAI an extremely novel spin label.

The initial part of this work focused on developing and optimizing the SDSL protocol for the TTAI probe. Acetyl-imidazole was chosen as a linker instead of the more common methanethiosulfonate, allowing for label binding through a one-atom bridge. Labeling was achieved through nucleophilic substitution of cysteinate anion on the TTAI carbonyl carbon, involving imidazole as the cysteinate-selective leaving group. TTAI proved to be highly insoluble, pH sensitive and with a weak leaving group because no reaction yields over 40% could be obtained. TTAI water solubility could be improved binding a bio-compatible charged hydrophilic functional group to one of the thiophene rings, which should definitely improve the labeling efficiency.

M13TT purification was achieved through reverse phase chromatography (RPC) using trifluoroacetic acid (TFA) as a coupling agent. Labeled TT stability in a 0.1% TFA solution was determined through hydrolysis kinetics. The M13-bound TT (M13TT) proved to be pH sensitive as well as it undergoes hydrolysis over timescale of days in solutions of pH ranging from 7 to 8.3, at room temperature. From the EPR spectra of the various peptide-protein samples it was evident that the ester bond undergoes hydrolysis over freeze-unfreeze cycles too. To shorten the whole labeling procedure and prevent M13TT degradation over pH, the use of RPC right after the overnight reaction should be tested since in the final protocol no evident peak broadening was observed for DMSO concentrations up to 25%.

UV-Vis spectroscopy was used to characterize the labeled peptide. The molar extinction coefficients were determined for M13C at 280 nm and for TTAI at 280 and 376 nm for solutions in various MilliQ water and DMSO ratios. M13TT could be distinguished from free TTAI because binding the label to M13C causes a blue-shift on the TT maxima of absorption at 376 nm, moving it to 344 nm.

Potential alterations in the secondary structure upon labeling were assed using circular dichroism (CD) spectroscopy. CaM interaction with M13TT showed a small decrease of the α-helix content with respect to the one interacting with M13C. CD measurements proved that a high hydrophobic label such as TT can cause slight protein misfolding.

ED-EPR experiments on protein bound M13TT proved the presence of both *trans/trans* and *cis/cis* TT, in contrast to the *trans/trans* conformation observed for free TT. Therefore, defying expectations, the one-atom linker strategy alone is not sufficient to guarantee narrow distance distributions since the different conformations widen the umbrella of adopted configurations.

Pulsed dipolar spectroscopy using DEER and ReLaser-IMD experiments were planned to determine respectively NO•—TT• and NO•—T_1TT distance distributions. As TT proved to act as mediator for photoinduced radical generation, even after few seconds of laser illumination, the distances with protein radicals could be observed as well. In contrast, at 355 nm and in the absence of TT, hours of laser illumination are needed to photoinduce protein radicals. The presence of more than two radicals in the peptide-protein complex noticeably complicated DEER (and ReLaser-IMD as well) distance distributions. Poor signal emerged from ReLaser-IMD experiments, proving TT not viable as a photoexcitable spin label. Despite the poor SNR and low modulation depth, the experiment still allowed selective observation of TT-related distances and helped disentangle contributions from the multiple radical species. To interpret the various distances a molecular model was used. Using the model, the experimental distance distributions could be interpreted as arising from specific radical-radical pairs or radical-triplet pairs. Moreover, the presence of distances longer than the molecular size proved slight protein misfolding as detected from CD spectroscopy.

Overall, the suitability of TT as a spin label appears limited, since it is neither a pure triplet label nor a fully photo-reducible one. After 15 hours of laser illumination not all TT had been converted to its radical form. As TT EPR literature is extremely poor, such a result would have been unforeseeable. The only way to make TT effective for ReLaser-IMD experiments would be finding a way of inhibiting the radical photoinduction.

Despite all these shortcomings, future work should not only focus on mitigating the limitations of TTAI, but also on exploring the unexpected opportunities revealed by its photochemistry. While photoinduced radical formation complicated the interpretation of the present measurements, it may represent the basis for an entirely new class of pulsed EPR experiments. The observation that TT photoexcitation can generate protein-based radicals, likely involving Tyr and Trp residues, suggests the possibility of performing distance measurements using only a single externally introduced probe. In such a strategy, a single TT label would be attached to the macromolecule, while site-directed mutagenesis would be used to position suitable radical-forming amino acids at defined locations within the protein. Upon photoexcitation, the transient amino-acid radical could act as a second spin center, enabling light-triggered distance measurements without the need for a second covalently attached spin label. If demonstrated experimentally, this approach could significantly simplify sample preparation and expand the range of systems accessible to pulsed EPR spectroscopy. Alongside efforts aimed at improving the solubility, stability, and triplet-state properties of thiophene-based labels, the development of such single-probe methodologies represents a particularly promising and potentially transformative direction for future research.

Acknowledgments

Five years have passed as a chemistry student and finally it's time for my path to come to an end. I'm grateful to my parent's that let my experience the academic life in Padua and that always provided encouragement, love and support. Thanks for always being there.

The two master's years proved to be the most challenging of all. Some of my friends took longer time to finish their bachelor studies, other didn't continue with the master's study. Then came the different choice of courses, the Erasmus program and the lab work for the thesis contributing to dismember even more us students. Solitude was always ready to manifest but never took over. Thanks to Piero and Haoni for taking me out of my room, to Michele for the various healing outdoor adventures, to Marco, Vincenzo, Riccardo, Daniele and Franceso for the lunches at Piovego canteen and to Costanza for all the unmissable breakfasts at Manzato's bakery.

'Defying my expectations', I loved working in the laboratory, doing reactions, purifications, characterizations, simulations and always trying to find a way to do better. Thanks to Prof. Marco Bortolus for teaching me how to work in a laboratory, for always being present and careful. Also, thanks to Prof. Cristina Peggion, my co-supervisor, and Sabrina, the lab technician.

Special thanks to all my roommates Simone, Gabriel, Sara, Federica, Alice, Bianca Gabriele; to Shamir, Ismaele, Maria, Marta and Valentina from the FitOne family; to Anna, Samuel, Francesco, Andrea and Jacopo from the PhD's office; and to all the members of the GCRC.

Almost since a year and a half a special person came in my life. Thank to Anouk, for all the love, support, patience, holydays, fun and for teaching me a lot. I love spending time with you, and I hope we will manage to realize all our dreams (maybe including owning an Appaloosa). Thanks to your family for having accepted me, for including me on vacations and restaurant visits. I never feel alone, love you.

Bibliography

1. Muscle contraction. *Wikipedia* (2026).
2. Beghi, S. *et al.* Calcium Signalling in Heart and Vessels: Role of Calmodulin and Downstream Calmodulin-Dependent Protein Kinases. *Int. J. Mol. Sci.* **23**, 16139 (2022).
3. Bayley, P. M., Findlay, W. A. & Martin, S. R. Target recognition by calmodulin: dissecting the kinetics and affinity of interaction using short peptide sequences. *Protein Sci. Publ. Protein Soc.* **5**, 1215–1228 (1996).
4. Andrews, C., Xu, Y., Kirberger, M. & Yang, J. J. Structural Aspects and Prediction of Calmodulin-Binding Proteins. *Int. J. Mol. Sci.* **22**, 308 (2021).
5. Babu, Y. S. *et al.* Three-dimensional structure of calmodulin. *Nature* **315**, 37–40 (1985).
6. Ikura, M. *et al.* Solution structure of a calmodulin-target peptide complex by multidimensional NMR. *Science* **256**, 632–638 (1992).
7. Jablonski Diagram | Perrin-Jablonski Diagram. https://www.edinst.com/resource/what-is-a-jablonski-diagram-perrin-jablonski-diagram/ (2021).
8. Tait, C. E., Krzyaniak, M. D. & Stoll, S. Computational tools for the simulation and analysis of spin-polarized EPR spectra. *J. Magn. Reson.* **349**, 107410 (2023).
9. Jeschke, G. DEER Distance Measurements on Proteins. *Annu. Rev. Phys. Chem.* **63**, 419–446 (2012).
10. Bertran, A., Barbon, A., Bowen, A. M. & Di Valentin, M. Chapter Seven - Light-induced pulsed dipolar EPR spectroscopy for distance and orientation analysis. in *Advances in Biomolecular EPR* (ed. Britt, R. D.) vol. 666 171–231 (Academic Press, 2022).
11. Bieber, A., Bücker, D. & Drescher, M. Light-induced dipolar spectroscopy – A quantitative comparison between LiDEER and LaserIMD. *J. Magn. Reson.* **296**, 29–35 (2018).
12. Hintze, C., Bücker, D., Domingo Köhler, S., Jeschke, G. & Drescher, M. Laser-Induced Magnetic Dipole Spectroscopy. *J. Phys. Chem. Lett.* **7**, 2204–2209 (2016).
13. Cafiso, D. S. Wayne Hubbell and the Path to Site-Directed Spin Labeling. *Appl. Magn. Reson.* **55**, 5–10 (2024).
14. Roopnarine, O. & Thomas, D. D. Structural Dynamics of Protein Interactions Using Site-Directed Spin Labeling of Cysteines to Measure Distances and Rotational Dynamics with EPR Spectroscopy. *Appl. Magn. Reson.* **55**, 79–100 (2024).
15. Bennati, M., Németh, K., Surján, P. R. & Mehring, M. Zero-field-splitting and π-electron spin densities in the lowest excited triplet state of oligothiophenes. *J. Chem. Phys.* **105**, 4441–4447 (1996).
16. Wintgens, V., Valat, P. & Garnier, F. Photochemical generation of radical cations from thiophene oligomers. *J. Phys. Chem.* **98**, 228–232 (1994).

17. Barratt, M. D., Dodd, G. H. & Chapman, D. A spin label for tyrosine residues. *Biochim. Biophys. Acta BBA - Protein Struct.* **194**, 600–602 (1969).

18. MTURA, R., SUGIYAMA, T. & YAMANO, T. Spin Label Studies on the Interactions of Bovine Adrenodoxin with NADPH-Adrenodoxin Reductase and with Cytochrome P-450sec. *J. Biochem. (Tokyo)* **85**, 1107–1113 (1979).

19. Chen, Y.-T. *et al.* Rigid and stable nitroxide spin label for high-resolution distance measurements on proteins by DEER experiments. *Magn. Reson. Lett.* **5**, 200194 (2025).

20. Wang, Y. *et al.* Synthesis of Unnatural Amino Acids Functionalized with Sterically Shielded Pyrroline Nitroxides. *Org. Lett.* **16**, 5298–5300 (2014).

21. Rajca, A. *et al.* A Spirocyclohexyl Nitroxide Amino Acid Spin Label for Pulsed EPR Spectroscopy Distance Measurements. *Chem. – Eur. J.* **16**, 5778–5782 (2010).

22. Bode, B. E. & Norman, D. G. Pulsed Electron-Electron Double Resonance (PELDOR) and Electron Spin Echo Envelope Modulation (ESEEM) Spectroscopy in Bioanalysis. in *Radiation in Bioanalysis: Spectroscopic Techniques and Theoretical Methods* (eds Pereira, A. S., Tavares, P. & Limão-Vieira, P.) 195–212 (Springer International Publishing, Cham, 2019). doi:10.1007/978-3-030-28247-9_7.

23. Handbooks - Cytiva. https://www.cytivalifesciences.com/en/us/support/handbooks.

24. Stoll, S. & Schweiger, A. EasySpin, a comprehensive software package for spectral simulation and analysis in EPR. *J. Magn. Reson.* **178**, 42–55 (2006).

25. Jeschke, G., Bender, A., Paulsen, H., Zimmermann, H. & Godt, A. Sensitivity enhancement in pulse EPR distance measurements. *J. Magn. Reson.* **169**, 1–12 (2004).

26. Goldfarb, D. & Stoll, S. *EPR Spectroscopy: Fundamentals and Methods*. (John Wiley & Sons, 2018).

27. Jeschke, G. *et al.* DeerAnalysis2006—a comprehensive software package for analyzing pulsed ELDOR data. *Appl. Magn. Reson.* **30**, 473–498 (2006).

28. Pettersen, E. F. *et al.* UCSF ChimeraX: Structure visualization for researchers, educators, and developers. *Protein Sci. Publ. Protein Soc.* **30**, 70–82 (2021).

29. Goddard, T. D. *et al.* UCSF ChimeraX: Meeting modern challenges in visualization and analysis. *Protein Sci. Publ. Protein Soc.* **27**, 14–25 (2018).

30. Meng, E. C. *et al.* UCSF ChimeraX: Tools for structure building and analysis. *Protein Sci.* **32**, e4792 (2023).

31. Hanwell, M. D. *et al.* Avogadro: an advanced semantic chemical editor, visualization, and analysis platform. *J. Cheminformatics* **4**, 17 (2012).

32. Albrecht, F. & Strube, O. I. A Python tool for predicting optimal solvent blends based on Hansen solubility parameters. *J. Coat. Technol. Res.* **22**, 1263–1268 (2025).

33. Manning, M. C. & Woody, R. W. Theoretical CD studies of polypeptide helices: Examination of important electronic and geometric factors. *Biopolymers* **31**, 569–586 (1991).

34. Kelly, K. L. *et al.* Conformational Ensembles of Calmodulin Revealed by Nonperturbing Site-Specific Vibrational Probe Groups. *J. Phys. Chem. A* **122**, 2947–2955 (2018).

35. Bennati, M., Grupp, A., Mehring, M. & Bäuerle, P. Pulsed EPR Spectroscopy of the Photoexcited Triplet States of Thiophene Oligomers in Frozen Solution. *J. Phys. Chem.* **100**, 2849–2853 (1996).

36. Ignasiak, M. *et al.* Iodide influences the sensitized one-electron photo-oxidation of Tyr and Trp residues by competition reaction. *Redox Biochem. Chem.* **12**, 100050 (2025).

37. Ji, H.-F. & Shen, L. Triplet excited state characters and photosensitization mechanisms of α-terthienyl: A theoretical study. *J. Photochem. Photobiol. B* **94**, 51–53 (2009).